2016

Burst-mode laser particle image velocimetry with multi-time step processing for improved dynamic velocity range

Mark Jeffrey Johnson
Iowa State University

Burst-mode laser particle image velocimetry with multi-time step processing for improved dynamic velocity range

by

Mark Jeffrey Johnson

A thesis submitted to the graduate faculty

in partial fulfillment of the requirements for the degree of

MASTER OF SCIENCE

Major: Mechanical Engineering

Program of Study Committee:

James Michael, Co-Major Professor

Terrence Meyer, Co-Major Professor

Hui Hu

Alberto Passalacqua

Iowa State University

Ames, Iowa

2016

TABLE OF CONTENTS

LIST OF FIGURES

LIST OF TABLES

ACKNOWLEDGEMENTS

I would like to start by thanking my committee chairs, Dr. James Michael and Dr. Terrence Meyer, and my committee members, Dr. Hui Hu and Dr. Alberto Passalacqua, for their support and guidance throughout the duration of my graduate research and studies. I need to give a special thanks to Dr. Hu for giving me the opportunity to research for him, both in Ames and in Shanghai, China.

I owe a lot of the success I have had during my graduate studies to Dr. Meyer. He gave me an opportunity as an undergraduate to help in his lab, and that time I spent in his lab propelled me into my Masters studies. He has afforded me a number of opportunities, and for that I will forever be grateful.

When Dr. Meyer left for Purdue, Dr. Michael was willing to take me on as one of his first graduate students. His help and support during that past few years have been truly remarkable. I learned so much from Dr. Michael, and I am forever thankful he wanted to take on my project and support me.

I would also like to thank Chloe, Jordan, Abhijeet, and Keke as well as all of my fellow graduate students for all of their help and support. I will always be remember and appreciate the friendships I developed during the past several years.

Finally, I need to give a big thanks to my family. My parents' love and encouragement has been ever-present during my entire life. Without their support, I would not be where I am today, and I will forever be thankful for the blessings of a wonderful family.

ABSTRACT

Particle image velocimetry (PIV) is robust means of making accurate velocity measurements in dynamic fluid environments. However, limitations in temporal resolution and dynamic velocity range have always resulted from insufficient data acquisition systems. As laser technology continues to advance, so do the potential capabilities of PIV. Today, burst-mode laser systems are capable of MHz repetition rates. These advancements in temporal resolution allow new insight into the dynamics of highly turbulent flows. Optimization of the pulse-burst laser for PIV will allow for unparalleled measurement capabilities.

In this work, a method for high temporal resolution, high dynamic velocity range PIV is proposed by means of multi-frame processing of particle images. This was accomplished using a triple-pulsed, burst-mode laser system and high-speed, CMOS sensor. Pulse triplets, with time spacings tailored to the flow velocity, were repeated at 10 kHz which resulted in three particle images per instance. Correlation between each combination of these three images produced three separate vector fields. Vectors were then selected based on comparisons of correlation plane data. This method of vector selection was tested using synthetically generated particle image sequences. Resulting composite vector fields increased the dynamic velocity range while simultaneously decreasing processing based uncertainty when compared to standard, two-frame PIV processing.

An experimental study of a fully developed turbulent jet over a range of Reynolds numbers was performed. PIV data was collected both free jet and cylindrical bluff-body test cases. Results of multi-frame processing supported the synthetic results, showing decreased uncertainty over the entire velocity range of the flow when compared to standard processing.

CHAPTER 1 INTRODUCTION AND MOTIVATION

Particle image velocimetry has long been a robust technique for making accurate velocity measurements in dynamic fluid environments. PIV research has become commonplace in application areas such as aerodynamics and combustion research. In many applications, PIV is used to study turbulent flows consisting of a wide range of time scales. The velocity ranges in these flows often exceed the limits of standard PIV. Because of this, measurement techniques with greater dynamic velocity range as well as increased spatial and temporal resolution are required.

Burst mode lasers are capable of high energy and megahertz repetition rates, making them an ideal solution to increasing temporal resolution. Another unique capability of these lasers is their flexibility to create pulse trains with varying temporal spacing. Exploiting this capability has the potential to allow for measurements with increased dynamic velocity range.

In this work, a method for increased dynamic velocity range PIV measurements is detailed. A burst mode laser system was used to generate pulse triplets at time spacings optimized to flow conditions. High repetition rates of the pulse triplets was used to simultaneously achieve ideal temporal resolution. Imaging of these triplets subsequently created multiple time spacings, each of which represented the same instance in time. Correlation of each time spacing produced three separate vector fields. These fields were then combined using a selection algorithm that optimized for uncertainty minimization. By using multiple time spacings for each instantaneous realization, dynamic velocity range of the technique was increased.

Additional information on PIV and burst mode lasers is provided in the following section. A detailed overview of the experimental setup and processing algorithm is then provided. Following this, the results of the study are presented in a manner that demonstrates the improvements of multi-frame pulse burst PIV over standard two-frame. Finally, conclusions are drawn and future work is discussed.

CHAPTER 2 BACKGROUND INFORMATION

2.1 Particle-Based Velocimetry Diagnostics

The desire to make qualitative as well as quantitative measurements in dynamic fluid environments facilitated the development of many flow visualization and measurement techniques. Velocity measurements in fluids are of particular importance in many applications. Because of this, a family of three experimental techniques was developed to make non-intrusive velocity measurements by means of particle imaging. These three techniques are Particle Tracking Velocimetry (PTV), Laser Speckle Velocimetry (LSV) and Particle Image Velocimetry (PIV). For all three of these techniques, a flow is seeded with tracer particles, and a camera is used to image the seeded flow and velocity information is extracted from the motion of the tracer particles. The difference in these techniques lies in the seeding densities, which in turn restricts the manner in which the generated particle images can be analyzed.

2.1.1 Particle Tracking Velocimetry

Particle tracking velocimetry was developed from flow visualization techniques such as particle-streak velocimetry and stroboscopic photography [1]. Low seed densities made it possible to track individual particle displacements in a double-exposed image. Originally, double-exposed images recorded on film used auto-correlation algorithms to determine displacements. With auto-correlation, magnitude and angle of the correlation peaks are known but the phase is not. This results in directional ambiguity in the single images. With the advent of digital imaging, auto-correlation on double-exposed images was replaced by the cross-correlation of two singly-exposed images. With cross-correlation, phase is recovered as well as magnitude and angle [2].

2.1.2 Laser Speckle Velocimetry

Laser speckle velocimetry lies on the opposite end of the spectrum from PTV. While LSV image acquisition is identical to PTV, LSV uses extremely high seed densities. This makes correlation-based particle tracking impossible. Instead, LSV image analysis techniques are rooted in solid mechanics. Double-exposed images are analyzed using a coherent light source. Scattered coherent light will naturally form a speckle pattern due to constructive and destructive interference [1]. Light from the coherent source is used to illuminate areas of the double-exposed image. The resulting speckle diffraction pattern will contain fringes with a given angular spacing which can be used to solve for displacement [3]. This analysis can be performed in small regions over the entire image leading to an increase in spatial resolution over PTV. Due to the tedious analysis process and the advent of more efficient digital techniques, LSV is rarely used.

2.1.3 Particle Image Velocimetry

Particle image velocimetry is a correlation-based diagnostic technique much like PTV. However, as opposed to PTV where single particles are tracked, PIV tracks groups of particles through image correlation techniques. Because of this, PIV achieves the same type of spatial resolution as LSV. PIV will be discussed at length in Chapter 2.2.

Table 1gives a comparison of the three seeded, laser-based velocimetry techniques. It also compares these techniques to Laser Doppler Velocimetry (LDV) which is also a particle velocity measurement tool. LDV is commonly used when high accuracy is required. However, LDV is restricted to essentially point measurements. As a result, the three other techniques are used when increased spatial resolution is desired. Of the three planar techniques, LSV provides

the greatest accuracy, but also the greatest challenge in processing. PIV and PTV are both robust means for accurate velocity measurements in all sorts of fluid dynamic environments, which makes them both quite common. The values contained in Table 1 are based on commercially available systems for PTV, PIV and LDV [4] [5] [6]. LSV analysis is more challenging and time consuming than the other methods, so commercial systems are not readily available. Information regarding LSV comes directly from the literature [1] [3] [7].

Table 1. Comparison of particle based velocimetry techniques. PIV, PTV and LSV are all planar techniques where LDV is a point measurement. Differences in measurement and processing techniques result in accuracy, resolution and range.

	Description	*Velocity Components*	*Accuracy*	*Spatial Resolution*	*Temporal Resolution*	*Dynamic Velocity Range*
Particle Image Velocimetry (PIV)	Sub-regions of illuminated particles are correlated spatially between singly-exposed images. Results in equally spaced vector field with one vector per interrogation region.	U,V,W	±0.1 pix	8 x 8 pixel sub-regions with 50% overlap.	Yes, commercially available systems can be resolved to 100 µs	100-200 Zero displacement not resolvable
Particle Tracking Velocimetry (PTV)	Individual particles are tracked between images either double exposed single images, or singly exposed double images Resulting vector field is a function of quantity tracer location.	U,V,W	±0.1 pix	Theoretically, PTV should allow for a vector from each particle. Limited by seeding density and particle overlap.	Yes, commercially available systems can be resolved to 100 µs	100-200 Zero displacement not resolvable
Laser Speckle Velocimetry (LSV)	Particle group tracking like PIV. Ultra-high seed densities mean particle overlap is unavoidable. Analysis of double-exposed single images is performed using a coherent beam to produce fringe pattern.	U,V	1-2% of measured velocity	Similar to PIV	Theoretically the same as PIV and PTV, however due to slow processing times not usually attempted	100-200 Zero displacement not resolvable
Laser Doppler Velocimetry (LDV)	CW laser source is split and two beams are focused and intersected at their waist. Intersecting beams create an interference pattern. As tracer particles move through the fringes, they scatter light into the sensor. Scattered light intensity fluctuation frequency is proportional to the velocity component of the particle in the plane of the two beams.	U,V,W	0.1% of max velocity	Point measurement. By traversing through the flow, high spatial resolution is achievable. Time-averaged only	CW laser means temporal resolution is only a function of only the acquisition system.	Zero displacement to supersonic particles speeds are resolvable

2.2 Particle Image Velocimetry (PIV)

2.2.1 Overview of PIV

PIV is a non-intrusive diagnostic technique used to determine instantaneous, local velocity vector fields in fluid flows. There are numerous variations on this technique; however, PIV is most commonly used to determine two-dimensional velocity vectors in a planar region of a flow. Many detailed reviews of the technique are available in the literature [1,2,8–13].

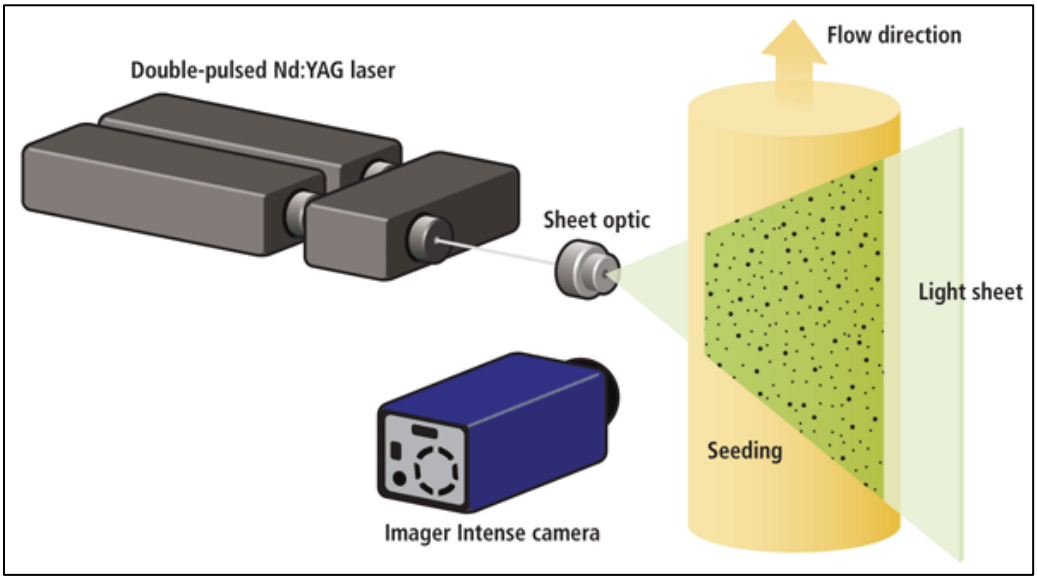

Figure 1. Diagram of a typical planar PIV setup. A camera is position normal to the plane of the laser sheet. The laser then illuminates tracer particles which are imaged by the camera [14].

Modern PIV systems utilize pulsed lasers focused to a sheet as the source of illumination. This sheet illuminates the plane of interest in the flow. The flow is seeded with micron sized, neutrally buoyant particles. Depending on the type of fluid being studied, the tracer particles can range from solids to atomized liquids. These particles follow the flow with minimal error, while acting as a scattering medium for the laser light. A high-speed camera focused onto the laser

sheet images the light scattered by the seed particles. Short duration laser pulses, on the order of nanoseconds, effectively freeze the flow in time. One pulse is imaged per frame, and then consecutive frames can be broken into interrogation regions and correlated to determine particle displacement between pulses. With dual-head lasers, the time separation between pulses from each head can be controlled with great precision. Now that particle displacement for each interrogation region and pulse separation are known, velocity vectors for each interrogation region can easily be calculated.

2.2.2 Seeding

PIV seeding is of utmost importance to the generation of quality images. Particle diameters need to be sufficiently small to allow adequate response to the fluid, yet the tracer particle scattering cross-section must be large enough to facilitate a sufficiently high signal-to-noise ratio. The scattering cross section is defined as the ratio of the total scattered power to the incident laser intensity [15]. For a particle suspended in a fluid, the Stokes number is defined as the characteristic non-dimensional frequency of the particle's response to fluid motion.

$$St = \frac{\tau_p}{\tau_f} \tag{1}$$

In Equation 1, τ_p represents the response time of the particle and τ_f represents the characteristic time of the flow. In a turbulent flow, τ_f is equal to the turnover time of a relevant turbulent structure. Often times, the Kolmogrov time scale is used, which is equal to the turnover time of the smallest eddy in the flow. The Stokes number determines the degree of coupling between particles and the fluid. As values of the Stokes number approach zero, the particle will behave like an ideal tracer while for large Stokes numbers, particles become unresponsive to the flow.

Choice of tracer particle type, diameter and seeding density varies based on the fluid density, viscosity, velocity and whether or not the flow is reacting. Table 2 gives a list of types several and sizes of seed particles used in gas phase PIV. In gas phase PIV, both solid and liquid tracer particles are used. Most commonly, seed particles will be on the order of 1-10 μm in diameter. When larger than this, the inertial forces of the particles becomes non-negligible and the Stokes number tends to rise. In the literature, detailed reviews of the effect of tracer particle size and material are given in Raffel *et al* and Melling [10] [15].

Table 2. Standard tracer particle materials and sizes for gaseous flows, adapted from work by Melling [15]. *This table shows several examples from the literature.* [16] [17] [18]

MATERIAL	PARTICLE DIAMETER (MM)	LASER	PULSE ENERY, PULSE TIME	PULSE WIDTH (MM)	PULSE THICKNESS (MM)
TIO_2	0.7-1.0	Nd:YAG	110 mJ, 12 ns	15	0.3
AL_2O_3	0.3	Nd:YAG	400 mJ	Not Given	0.2
OLIVE OIL	1.06	Nd:YAG	70 mJ, 16 ns	200	0.5

While size and material are vital components to effectiveness of tracer particles, equally important is the seeding density. Adrian defines two dimensionless parameters that describe the effects of particle seeding density [1]. The source density (N_s), represents the likelihood that particles overlap one another, and the image density (N_i) is the mean number of particles per interrogation region. Optimal values for these parameters depend on the processing scheme (PTV, LSV, or PIV) being used. For PIV, a high image density with a low source density is desirable. Proper seeding density will ultimately have a profound effect on the quality of the resulting vector field.

2.3 PIV Processing

2.3.1 Cross-Correlation Processing Technique

Before the advent of digital imaging, double-exposed photographic images were analyzed in a similar fashion to PTV or LSV, as mentioned earlier. Photographically recorded transparency images were interrogated by means of optical autocorrelation or Young's fringe method [2]. Manual analysis of the transparencies was a tedious and time consuming process. With the advent of digital imaging, discrete Fourier transform auto-correlation based techniques became the preferred method [8]. Modern analysis of particle images is done by spatial cross-correlation of singly-exposed digital images. Sequential digital images are divided into sub-windows called interrogation regions, each of which will ultimately yield one displacement vector. Interrogation regions can range in size depending on the particle density and magnification of the image. Typical interrogation region sizes range from 16x16 to 64x64 pix^2. Interrogation regions often overlap up to 50 percent in order to increase spatial resolution of the resulting velocity vector field. The cross-correlation of an interrogation can either be performed directly or by using a discrete Fourier transform. Given a pair of images $(g_1(i,j),\ g_2(i,j))$ with interrogation regions of pixel size $\big((2M+1),(2N+1)\big)$ centered at some value (i,j), the discretized form of the cross-correlation equation is a follows:

$$r(m,n) = \sum_{i=-M}^{M} \sum_{j=-N}^{N} [g_1(i,j)] \cdot [g_2(i+m, j+n)] \tag{2}$$

In Equation 2 , *r(m,n)* is said to be the standard correlation coefficient and *m* and *n* are pixel coordinates of the correlation peak. Computing cross-correlations between two images directly is quite computationally expensive, so often images are transformed using a fast Fourier transform (FFT) in order to avoid the summations [19]. The discretized forms of a Fourier

transformed cross-correlation is given in Equations 3-5. It can be seen that after the transformation, the cross-correlation simply becomes the product of the complex conjugate of the first image and the second image (with * denoting the complex conjugate).

$$G_1(\xi,\eta) = \mathcal{F}\{g_1(i,j)\},\ \ G_2(\xi,\eta) = \mathcal{F}\{g_2(i,j)\},\ \ R(\mu,\nu) = \mathcal{F}\{r(m,n)\} \tag{3}$$

$$R(\mu,\nu) = G_1^{*}(\xi,\eta)\, G_2(\xi,\eta) \tag{4}$$

$$r(m,n) = \mathcal{F}^{-1}\{R(\mu,\nu)\} \tag{5}$$

Upon completion of the correlation, the inverse FFT is performed to convert back from the frequency domain into the correlation (spatial) domain [20]. The location of the peak value in the resulting correlation plane corresponds to the particle displacement for the interrogation region.

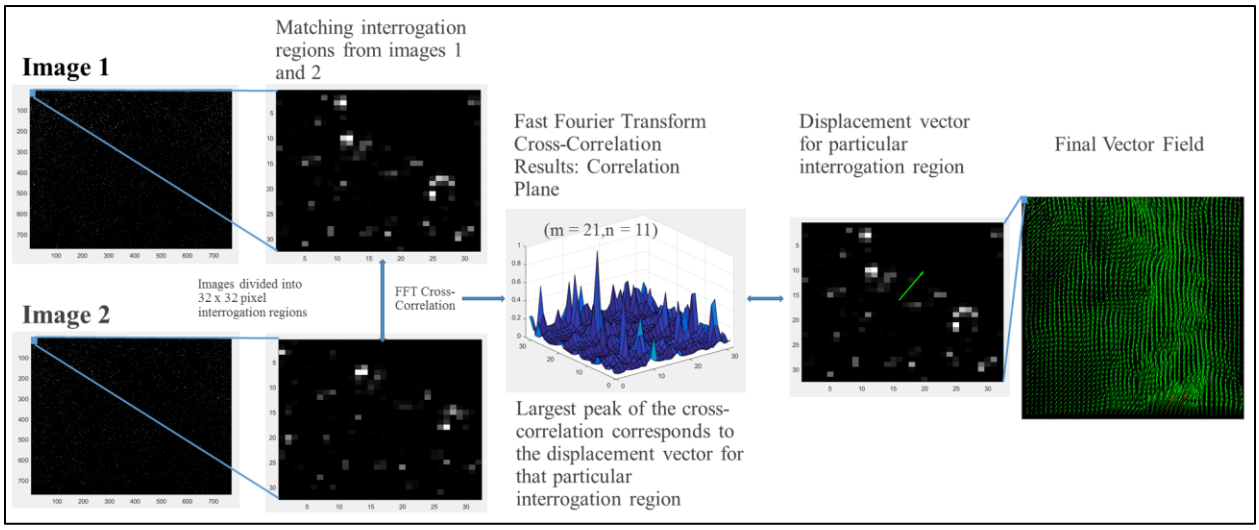

Figure 2. Cross-correlation PIV processing. Images are divided into sub-regions and correlated. Each sub-region yields one displacement vector.

Cross-correlation by itself is only capable of predicting pixel displacement of the particle field to an integer value. This can lead to large uncertainties (±0.5 pixels) in displacement values [12]. These uncertainties result in large errors, especially when small interrogation regions are used. Because of this, subpixel accuracy is essential to minimizing error. A number

of subpixel estimation methods and their algorithms are detailed in several works from Scarano, Brady and Dabiri [21] [22] [23]. The most common of these methods uses a 3-point Gaussian fit to predict subpixel displacement values. Particle image intensities are well approximated by a Gaussian distribution, which is why a Gaussian 3-point curve estimator is most commonly used. Sub-pixel estimators are capable of producing displacement vector accuracies on the order of 0.01 for synthetically generated data [22]. However, for experimental data, the standard estimate for the minimum resolvable velocity is on the order of 0.1 pixels. Error sources such as out-of-plane losses, velocity gradients, and particle intensity variations keep experimental accuracies from approaching the synthetic image accuracy levels [24].

2.3.2 Advanced Processing Techniques for Improving Resolution and Velocity Range

The dynamic velocity range (DVR) is defined as the ratio of the maximum resolvable velocity to the minimum resolvable velocity [25]. For single-pass processing schemes, DVR is limited by the size of the interrogation region. This leads to a direct trade-off between DVR and resolution. If a finer resolution is desired, smaller interrogation regions were necessary. The advent of multiple-pass processing techniques has eliminated this trade-off. Other techniques, such as multi-frame PIV, have been developed for the primary purpose of improving the velocity range of PIV.

Single-pass FFT cross-correlation analysis is the standard processing in modern PIV, but a number of variations exist that are capable of improved resolution, dynamic range, and accuracy. One such variation is multi-pass image-shifting processing. In its simplest form, multi-pass image-shifting involves analyzing an image pair with a coarse grid on the first pass. Once completed, the grid is refined (interrogation areas are usually 25% of the first pass) and a second pass is performed. Displacement values from the first pass are used to predict correlation

peak locations in the second pass. During the second pass, interrogation regions in the first particle image are arranged uniformly, but the corresponding interrogation regions in the second image are shifted by the predicted value from the first pass. Before the use of multi-pass processing, there was a trade-off between spatial resolution and velocity range. In order to ensure accurate velocity vectors, displacements are commonly limited to one-quarter of the interrogation region [26]. As the interrogation area is decreased, spatial resolution is increased but velocity range decreased. Multi-pass processing allows for an increase in spatial resolution without in-plane loss of particle image pairs. Many variations of this technique now exist, including higher order window deformation methods to further improve accuracy and eliminate error. These techniques are detailed in the following works [21] [27] [28] [29].

2.3.3 PIV Error Source and Analysis

Error associated with PIV measurements can be divided into two forms. The first is systematic or mean-bias error, and the second is random error [30]. Bias errors arise from the correlation and sub-pixel computations. One common form of bias error in PIV is a tendency of measured displacements to tend toward the closest integer value of displacement. This is called peak-locking, and it can result in error up to 0.1 pixels [31]. Peak-locking arises from measurement uncertainty inherent to PIV due to discrete pixel values. This error is intensified by using tracer particles with diameters smaller than two pixels [10]. Gaussian sub-pixel interpolation greatly reduces peak-locking, but it does not completely eliminate its effects [20] [32]. Multi-pass, image-shifting and image-deformation techniques were developed specifically to reduce this source of error [21] [28] [29] [33]. Another form of bias error is the systematic underestimation of particle displacements as displacement values increase.

Displacement values larger than 0.5 pixels display a linear increase in bias. Because of the linear trend, weighted correction is possible [8] [12].

The contribution of bias error to the overall inaccuracy of a measurement is generally small compared to errors from random fluctuations. This random error is often called RMS error. Common factors that contribute to RMS error include displacement gradients, in-plane and out-of-plane motion, seeding density, particle image diameter, and background noise [31]. Each of these contributing factors can be optimized for error minimization but these sources can never be completely corrected for or eliminated.

2.3.4 Vector Validation

Upon completion of correlation analysis, vectors in the resulting field can be classified into one of two categories: correct measurements with uncertainty or false/spurious measurements [34]. Uncertainty in correct vectors will be discussed in a later section. Spurious vectors arise due to random errors in either the image acquisition or correlation computations. Identification of spurious measurements is done primarily by statistical analysis in post-processing. Common identification operations involve minimum and maximum displacement limits along with local and global filtering [35] [36]. If particle image quality is high and the processing has been optimized, it is unlikely to find a high proportion of spurious vectors in a small sub-division of the vector field. Because of this, mean and median filtering are sufficient for validation in most PIV applications [36]. An adaptation to the local median filtering method is explored in Westerweel & Scarano [37].

2.3.5 Uncertainty Analysis

In the roughly 40 years since the advent of PIV, it has become a well-established and trusted diagnostic technique. Despite all of the developments and refinements to this technique

throughout recent years, quantification of uncertainty remains a challenge. PIV measurements vary in both time and space, which leads to a non-uniform error across the resulting vector field. This non-uniformity renders a universal uncertainty estimate inadequate [38]. PIV error sources are well-understood. However, because of the lack of whole flow field information, quantifying these errors is quite difficult. *A priori* error estimation methods have been developed based on theoretical analysis validated by Monte Carlo simulations of synthetically-generated flow fields. With synthetic data, whole field information is known precisely at each location. This allowed for processing techniques to be validated and optimized. Statistically converged simulation results allowed researchers to make predictions of error in actual experiments [39] [40]. Theoretical expressions to calculate error were also developed and compared to simulation results [20] [41]. *A priori* uncertainty predictions cannot account for all of the parameters that affect PIV measurement and analysis, leading to consistent underestimation of error, which limits their effectiveness [31].

Due to the lack of detailed global flow field information in prior PIV experiments, *a posteriori* methods of uncertainty quantification are desired. One such method involved identifying the primary sources of error in PIV measurements (particle size, particle density, velocity gradients and in/out-of-plane motion) and characterizing the overall contribution of each parameter to measurement inaccuracy. Characterization was done by simulations using synthetic datasets. Experimental uncertainty was then estimated by running simulations using the experimental values for each of the error sources [38]. Another method utilizes using correlation data to predict error. The signal-to-noise ratio of the cross-correlation data (ratio of the highest peak to the second highest) contains information directly related to the measurement quality, and can be used to quantify uncertainty [42] [43]. A third method involves using the measured

particle displacement from each interrogation region to shift the regions in the second image so particle locations should match between both the first and second images. Any error sources present in the flow will cause the superimposed second interrogation region to differ from the first. A cross-correlation is then performed between the first image and the shifted interrogation regions of the second image, and a disparity vector results. This disparity vector returns an estimate of velocity error for that interrogation region [31]. A review of current PIV uncertainty estimate methods and their effectiveness is available in Sciacchitano et al. [44].

2.3.6 Limitations of PIV

PIV has proven to be a robust means for making velocity measurements in fluids. However, there are still a number of limitations to this technique that must be addressed. First, limitations arise from the equipment used in data acquisition. Standard solid-state, Q-switched PIV laser sources (discussed in the next section) are limited to approximately 10-50 kHz repetition rates [12]. At these rates, temporal resolution is still not possible for highly turbulent flows or trans-sonic and super-sonic flows. Repetition rates up to 1 MHz are achievable with pulse-burst laser systems. However, at these extreme repetition rates, spatial resolution starts to become an issue due to high speed CMOS sensor limitations. For example, the top-of-the-line Photron Fastcam SA-Z CMOS camera is still only capable of 20,000 frames per second at 1024 x 1024 pixel resolution [45]. Multi-frame CCD sensors are capable of full frame operation at multi-MHz rates with a limited number of frames. Running the SA-Z at MHz rates to fully utilize these high laser repetition rates would greatly reduce the spatial resolution. Also, for such short camera exposures, the total amount of laser energy required becomes quite high. All of these factors limit PIV from achieving optimal spatial and temporal resolution in certain cases.

Image analysis provides another set of limitations. PIV processing is done by dividing particle images into sub-regions and then correlating those regions between frames to produce a displacement vector. In order to increase spatial resolution of the resulting vector field, smaller interrogation regions are desired. However, decreasing interrogation region size will also decrease the measureable maximum displacement. In certain situations, this leads to a direct trade-off between velocity range and spatial resolution. A common practice is to limit particles within an interrogation region to displacements less than one-quarter of the region [26]. This limit is set to avoid incurring large numbers of dropped vectors. However, it also does further limit maximum particle displacements that are measureable. Techniques have been developed to increase DVR while maintaining spatial resolution (see section 2.3.7). However, for flows with high vorticity or large gradients, using some of these techniques that allow for larger particle displacements to be correlated (multi-pass, image-shifting, etc.) will lead to increased error. Standard multi-pass processing techniques employ 16x16 square pixel interrogation regions with 50% overlap. Using smaller passes is possible, but the flow must be almost ideal. Out-of-plane losses and gradients have a drastic effect on interrogation regions this small [46].

Minimum particle shifts are also limited. Sub-pixel estimators are all but required in modern PIV, and they are able to achieve accuracies on the order of 0.01 pixels for synthetic data [22]. It is widely accepted that accuracies in experimentally acquired PIV data will be limited to approximately 0.1 pixels [24]. Because of these minimum and maximum particle displacement limits, DVR for standard PIV is usually limited to around 100-200 [47].

Other limitations in vector detection arise from particle image density and in-plane and out-of-plane losses. Keane and Adrian defined a metric for determining the likelihood of valid vector detection as a function of the particle density within the interrogation region (N_i), as well

as the in-plane (F_i) and out-of-plane (F_o) losses [39] [48]. For zero losses due to in-plane or out-of-plane particle motion, F_i and F_o will equal unity. The values of F_i and F_o will decrease as losses due to particle motion are incurred. For sufficiently high values of $N_i F_i F_o$, detection probability approaches 100%. However, in-plane and out-of-plane losses are unavoidable in PIV, and as a result valid vector detection will never achieve 100% experimentally.

2.3.7 PIV Variations

Stereoscopic PIV (Stereo PIV)

Stereoscopic PIV utilizes two cameras with overlapping imaging planes and different view axes in order to extract the out-of-plane velocity component. Stereo PIV is still a planar technique, but the resulting vector field contains three-dimensional velocity information [49]. In processing of stereo PIV, corresponding points on a calibration image are matched between the two cameras, enabling mapping functions to reconstruct all three velocity components [50].

Tomographic PIV (Tomo PIV)

Tomographic PIV shares similarities to stereo PIV; however, the result is a volume of three-component velocity vectors instead of just a plane. In tomo PIV, a volume is illuminated in the flow using pulsed laser. This volume is imaged using additional camera views (typically four or more). A calibration image is used to perform a tomographic reconstruction using the multiple images. Once reconstructed, the images are processed using spatial cross-correlation and a three-component vector volume results [51].

Time-Resolved PIV (TR-PIV) and Multi-Frame PIV

Advancements in PIV image collection and data processing have led to increased spatial and temporal range and accuracy in the velocity measurements. Higher repetition rate lasers and the improvement in CCD and CMOS technology have made it possible to perform standard

Planar PIV as well as Stereoscopic and Tomographic PIV with greatly increased temporal resolution. The term Time-Resolved PIV (TR-PIV) is used to describe these improved methods. TR-PIV has led to advances in turbulence research, which will be discussed in more detail later.

Improvements in TR-PIV data collection methods have led to innovations in image analysis. Multi-Frame PIV improves the dynamic velocity range (DVR) and accuracy of conventional TR-PIV by measuring local velocities with multiple time intervals [52]. Short time spacing between laser pulses makes it possible to get correlation data from not just consecutive pulses, but also longer time spacings. TR-PIV systems are typically designed to operate at a sufficiently fast rate to capture the smallest time scales of the flow, satisfying the Nyquist criterion [53]. However, in turbulence research, flows often contain a wide range of velocities. Short time spacings are far from optimal for the low velocity regions of the flow. One necessary improvement can be realized with Gaussian three-point sub-pixel estimators which can measure minimum displacements on the order of 0.1 pixels [28]. With this sub-pixel accuracy, the DVR over the whole field is still limited to around 200:1 [47]. Multi-frame PIV yields composite local velocity fields optimized at each vector location. As mentioned before, this increases accuracy, as well as the DVR.

2.4 Laser Sources and Sensors

2.4.1 Nd:YAG and Nd:YLF Lasers

The most common laser used in planar PIV is the Nd:YAG frequency doubled to emit at 532 nm. Nd:YAG lasers are capable of emitting 5-10 ns pulses at energies ranging from 12 to 1000 mJ per pulse with frequencies of 1-1000 Hz [12]. Typical Nd:YAG PIV lasers are dual-head systems, consisting of two separate laser cavities. Both laser cavities are pumped at the same frequency, but pulses from each laser can be precisely separated in time at intervals much

shorter than each individual laser's repetition rate. Short pulse spacings make studying faster flows possible. However, because the typical 10 Hz repetition rate is quite slow compared to common time scales in unsteady flows, temporal resolution of the flow field is not possible. With use of the imaging technique called frame straddling, the limiting factor for Δt becomes the interframe time of the imaging sensor. Frame straddling also allows for the camera to be operated at a frame rate as low as twice the laser frequency with no dead frames.

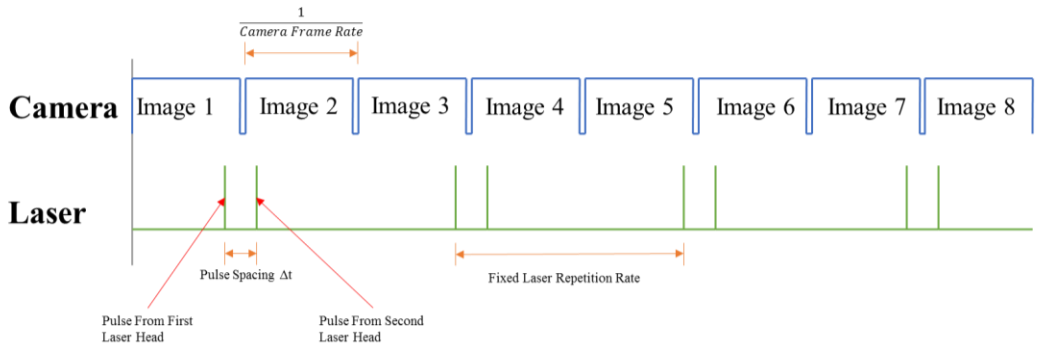

Figure 3. Timing diagram illustrating frame straddling. Top line represents camera exposures, and the bottom represents the laser pulses.

2.4.2 Burst-Mode lasers

As stated earlier, the innovations in laser technology have led to an increase in PIV temporal resolution. However, current commercially available diode-pumped solid-state lasers (Nd:YAG and Nd:YLF) are only capable of repetition rates of 10-50 kHz [54]. While this is a vast improvement, many high-speed flows have turbulent fluctuations occurring on much shorter time scales. Pulse-burst lasers provide improved repetition rates as well as increased energy outputs, both of which are vital to improving results the of TR-PIV. The pulse burst laser described by Thurow *et al* [55] uses a dual-Pockels-cell to slice a beam from a pre-amplified continuous-wave Nd:YAG laser into a tailor-made pulse train. Other pulse burst systems, like

the one used for this work, use an acousto-optic modulator (AOM) to achieve the same effect [56]. These pulse trains are capable of containing anywhere from 10 s to 1000 s of pulses with interpulse spacings shorter than 100 ns (10 MHz). Following the Pockels-cell or AOM, further amplification of the pulse train occurs. Multiple systems use a phase conjugate mirror (PCM) is used to simultaneously eliminate the low-intensity signal superimposed on the high-intensity pulses, as well as reduce amplified spontaneous emission (ASE) [57]. The result is an amplified pulse train capable of individual pulse energies greater than 100 mJ/pulse at 1064 nm. The capabilities of pulse burst lasers are well suited for high-speed PIV applications [54,57–59,56].

2.4.3 Imaging Systems

Modern PIV experiments primarily use either charge coupled device (CCD) or complementary metal oxide semiconductor (CMOS) imaging sensors. Both sensor types operate by converting light incident on each pixel during an exposure to electrical charge. In a CCD, the conversion from electric charge to a voltage occurs in a common output structure, where in CMOS sensors, the voltage conversion happens at each individual pixel [60]. Because of this, CMOS cameras will offer much higher frame rates, but CCD cameras are capable of greater resolution and lower noise levels. The type of PIV study often dictates the type of imaging sensor used. For time-resolved PIV, CMOS sensors typically are required by the high desired framerates. However, in situations where speed is not necessary but resolution is paramount, CCDs will provide the best results.

2.5 Turbulent Jet and Bluff-body Flow Physics

2.5.1 PIV and Turbulence Research

PIV has long been used as a means of better understanding and quantifying turbulent flow dynamics. For many years, standard PIV has provided the ability to make spatially resolved, time-averaged local velocity measurements of a turbulent flow. This information can then be used to derive turbulent flow statistics (i.e. turbulent kinetic energy, Reynolds stresses, etc.). Statistically converged, time-averaged flow field data from PIV is often used as a means of experimental validation of CFD models [61] [62]. Recent advances in laser and camera technology have made increased temporal resolution in PIV possible. Prior to PIV, the only way to achieve time-resolved flow field data was by means of point measurements using hotwires. TR-PIV is now allowing for both spatial and temporal resolution of large turbulent structures in flows. Frequencies of spatial and temporal structures from vortex shedding and other periodic large scale flow structures can be extracted from TR-PIV data using techniques like proper orthogonal decomposition (POD) and dynamic mode decomposition (DMD) [63] [64] [65].

2.5.2 Turbulent Jets

The free shear flow case of an axisymmetric, turbulent jet into an ambient environment of the same fluid is one classic example of a thoroughly studied turbulent flow. Turbulence texts contain detailed theoretical derivations and correlations for parameters such as centerline velocities and jet decay rates that have been supported by time-averaged experimental data [66] [67]. In an idealized case, a free turbulent jet can be completely defined by the jet exit diameter (d_{jet}), the velocity at the exit of the jet (u_{jet}), and the kinematic viscosity of the fluid (ν). Free turbulent jets will exhibit a development region from an axial displacement of $x/d_{jet} = 0$ to approximately $x/d_{jet} = 25$. Beyond this point, the flow is said to be fully developed and it

becomes self-similar. In this region, the centerline velocity and half-width of the jet are functions of only the axial-distance from the jet exit. Due to this, the Reynolds number of the jet has no effect on the mean velocity profile nor on the velocity-decay and spreading rates [66].

Understanding the flow phenomena present in turbulent jet flows requires more than just time-averaged data. A Reynolds decomposition of turbulent flows requires knowledge of not just mean velocity, but also velocity fluctuations. Early flow visualization techniques made it possible to observe repeating large scale structures in developing turbulent jets resulting from the unstable shear layer [68] [69]. Advances in PIV have made it possible to collect qualitative as well as quantitative data of vortices and other shear layer instabilities all throughout the development and self-similar regions of the jet [64] [70]. The increasing temporal and spatial resolution of PIV are making it possible to study smaller flow structures and shorter time scales which leads to a greater understanding of turbulent jets as a whole [71].

Another important aspect of turbulent jets is entrainment of the ambient fluid. Entrainment and turbulent mixing were long treated as a diffusion process that occurred on small scales. However, thanks to techniques such as Laser Induced Fluorescence (LIF), it was discovered that large-scale vortical motion was responsible for the bulk of mass transport [72] [73]. Turbulent mixing is of particular importance in PIV experiments of free shear jets. If the jet is seeded with tracer particles, entrained fluid from an unseeded ambient environment can disrupt seeding density and distribution, leading to poor correlations. Conversely, if the ambient fluid is seeded with tracers and the jet is unseeded, PIV measurements must be made sufficiently far downstream from the jet orifice to allow the effects of turbulent mixing to entrain an adequate amount of tracer particles into the jet core.

2.5.3 Cylindrical Bluff-Body Flows

A cylindrical body in a crossflow is a second classic fluid dynamics problem, and it is well understood. Bluff-body flows are known for having complex recirculation zones in the wake region which leads to cyclical vortex shedding. The Strouhal number is used to relate vortex shedding frequency to the flow velocity and characteristic length of the bluff-body. Many relations exist between Strouhal and Reynolds numbers which makes it possible to predict shedding frequency if the flow is well classified. Cylindrical bluff-body flows are common in turbulent combustion. Non-premixed, bluff-body diffusion flames provide high levels of turbulent mixing which aids in combustion control and flame stabilization [74].

2.5.4 Modal Decomposition Methods

Proper orthogonal decomposition (POD) and dynamic mode decomposition (DMD) are tools for identifying large coherent structures in turbulent flows. In both techniques, the vector velocity field is decomposed into a sum of weighted, linear basis functions (φ_m). These basis functions are often referred to as modes [75]. For POD analysis of empirical PIV data, x and y-velocity components from each realization are represented as a row in the **U** and **V** matrix respectively. The size of these matrices is then given as the number of realizations (K) by the total number of velocity vectors from the resulting field (M). Equation 6 shows instantaneous velocity fields are then decomposed into a linear combination of modes and corresponding coefficients. The spatial correlation matrix (**C**) is then given in Equation 7, where T denotes the transpose. Solving the eigenvalue problem shown in Equation 8 results in eigenvector (β_m) and diagonal eigenvalue (λ_m) matrices.

$$V^{(k)} = \sum_{m=1}^{M} c_m^{(k)} \varphi_m \tag{6}$$

$$\boldsymbol{C} = \frac{1}{K}(\boldsymbol{U}\boldsymbol{U}^{\boldsymbol{T}} + \ \boldsymbol{V}\boldsymbol{V}^{\boldsymbol{T}}) \tag{7}$$

$$\boldsymbol{C}\beta_{\boldsymbol{m}} = \ \boldsymbol{\lambda}_{\boldsymbol{m}}\beta_{\boldsymbol{m}} \tag{8}$$

After determining the eigenvalues and eigenvectors, the basis functions are calculated by projecting the velocity matrices (**U** and **V**) onto the eigenvector matrix β_m (Equation 9). Furthermore, coefficients of each mode are calculated by projecting the velocity matrices onto these basis functions (Equation 10).

$$\varphi_{m,x} = \ \beta_m \boldsymbol{U}^T \qquad \varphi_{m,y} = \ \beta_m \boldsymbol{V}^T \tag{9}$$

$$c_m^{(k)} = \ \beta_m U + \ \beta_m V \tag{10}$$

POD results will produce each mode ranked in order of decreasing energy. For flow field velocity data, the zeroth order mode will always represent the mean velocity field. Subsequently, this mode contains the majority of the energy. The most dominant flow structure will appear as mode 1, and so on. POD is often used to determine spatial modes from temporally uncorrelated data. Modal frequency analysis of temporally correlated data is possible with POD via Fourier analysis of time coefficient data. However, this procedure cannot identify spatial structure corresponding to a specific frequency [76]. In order to determine both spatial and temporal modes of time resolved data, DMD can be used. DMD is a modal decomposition method of temporally correlated orthogonal modes. These dynamic modes correspond to frequencies in the flow data [76] [77].

CHAPTER 3 EXPERIMENTAL SETUP

3.1 Setup Overview

In this chapter, the PIV equipment and setup is described. A pulse burst laser system in tandem with a high-speed Photron Fastcam SA-X2 CMOS camera were used to make triple-pulse PIV measurements in both a turbulent free jet as well as the same jet flow around a cylindrical bluff-body. Data was collected for three jet Reynolds numbers (Re = 10,000, 30,000 and 50,000) and two different camera magnifications (0.206 and 0.326). For all runs, the imaging plane of the camera was centered 10 jet diameters (D_{jet} = 8 mm) downstream. During PIV measurements of the bluff-body flow, the cylinder of diameter D_{bb} = 9.5mm was positioned 10 jet diameters downstream perpendicular to the imaging plane of the camera. Pulse triplets from the laser were repeated at a 10 kHz rate for the duration of a 5 ms burst. Within each triplet, pulse time spacings were varied based on the flow velocity. The camera triggered off the laser and ran at a fixed 50 kHz. A variation of frame-straddling was used to ensure that within each triplet, each individual pulse was singly exposed in three consecutive camera frames. In order to optimize spatial resolution with pulse spacing, two dead frames followed each three frames containing particle images. Particle images were saved and processed, which will be discussed in Chapter 4.

3.2 Laser and Imaging Setup

The pulse burst laser used in this study was quite similar to the pulse burst described in Michael et al [56]. A continuous-wave Nd:YAG laser diode emitting at the fundamental 1064 nm and at a power of approximately 300 mW is fiber coupled into a Gooch & Housego acousto-optic modulator (AOM). The AOM uses a radio-frequency (RF) driven piezoelectric transducer to produce oscillating sound waves in a crystal. These sound waves cause it to act like a

diffraction grating. Light diffracted by the crystal is directly proportional the power of the RF signal. Due to the oscillations in the RF signal, the crystal essentially acts like a shutter for any incident beam. The AOM is capable of producing a shuttering effect as fast as 100 MHz with rise time as short as 4 ns. Additionally, the RF signal is be manipulated to create a specific, tailored pulse pattern output. The AOM was driven continuously, but flash lamps for the amplifiers were run for a 5 ms duration. The output signal was a triple-pulse pattern repeated every 100 μs. After the 5 ms burst was created, the system was allowed to relax for 5 s before repeating.

Following the AOM, the resulting pulse slices were coupled into a fiber-amplifier. Pulse energy levels leaving the AOM were on the order of 10 nJ per pulse. This amplifier provided linear, small signal gain on the order of 10^3. Optical isolators were then used to reduce amplified spontaneous emission (ASE) before entering the first amplifier chain. The burst then made a double-pass through the first chain of amplifiers. This chain consisted of Amp 1A and Amp 1B. Both of these amplifiers were water cooled, flash-lamp pumped Nd:YAG rods where gains of 10^3 and 10^2 were achieved respectively. The smaller gain seen in the second amplifier indicates gain saturation and departure from the small-signal gain regime. Throughout the chain, spatial filters (pinholes) were used to reduce ASE.

More pinholes and optical isolators were used prior to the second amplifier chain, again in order to reduce ASE. The chain of amplifiers was very similar to the first. It provided double-pass amplification through two amplifiers (Amp 2A and Amp 2B), achieving double-pass amplification 200. However, before passing back through the amplifier chain the beam was reflected off a stimulated-Brillouin scattering (SBS) cell. Also called a Phase-Conjugate Mirror (PCM), this cell operates on the principles of stimulated Brillouin scattering, which is a non-

linear scattering phenomenon where an incident beam will be backscattered once a sufficient pulse energy is achieved. The purpose of the PCM was to remove the pedestal of ASE from the high energy pulses. Upon reaching a sufficient energy, the pulses were reflected back through the amplifier chain while any underlying, low energy signal was passed through and dumped.

The final amplifier, Amp 3, produced a saturated gain of 5, but it was not needed for these experiments. Following this amplifier, the pulse train was frequency doubled to 532 and then sheet forming optics were used to create and focus the laser sheet in the jet. A diagram of the laser is shown in Figure 4 and a sample oscilloscope trace showing relative pulse energies is shown in Figure 5.

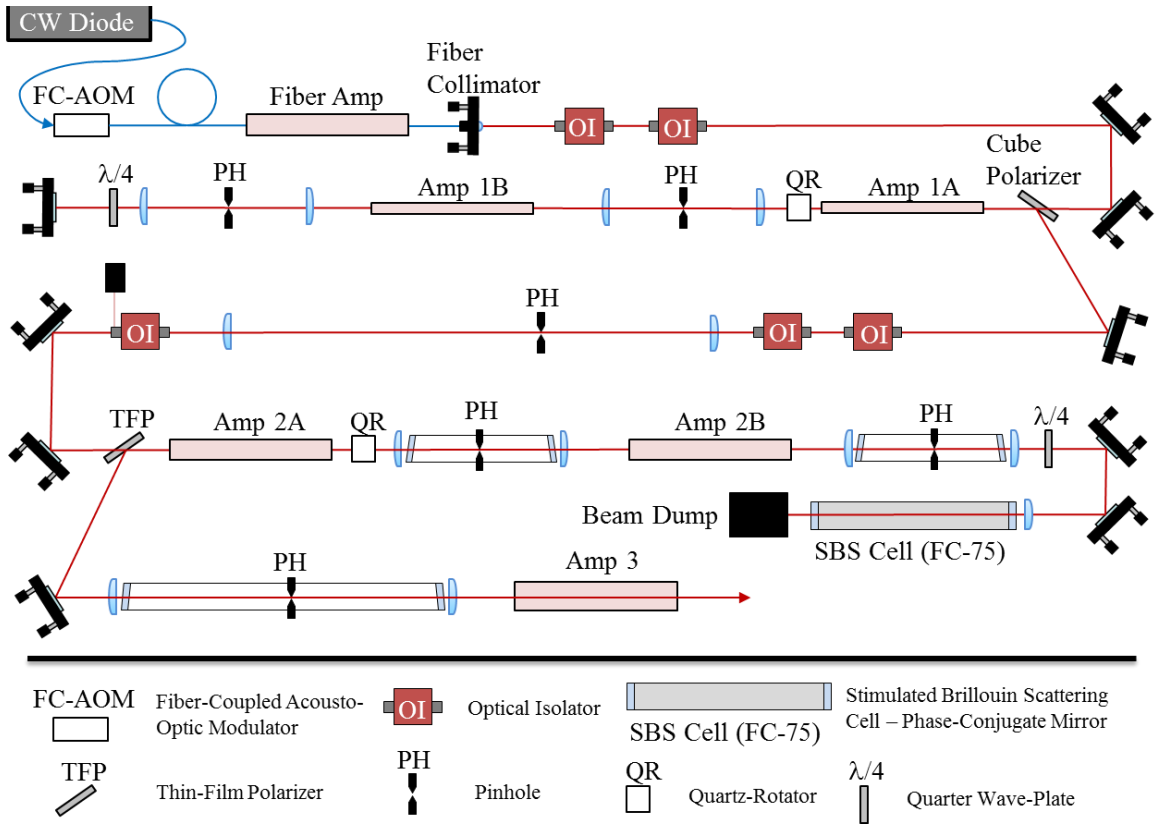

Figure 4. Pulse-burst laser diagram. Individual components are labeled, and abbreviations are listed below the diagram.

The camera used to capture the high-speed particle images was a Photron Fastcam SA-X2. The SA-X2 has a 12-bit CMOS sensor with 20 μm square pixels capable of full 1024 x 1024 pix resolution at 12,500 fps and 512 x 512 pix resolution at 45,000 fps. Shutter speeds of 293 ns and interframe times as short as 700 ns were achievable [45]. Magnifications settings of 0.206 and 0.326 were used.

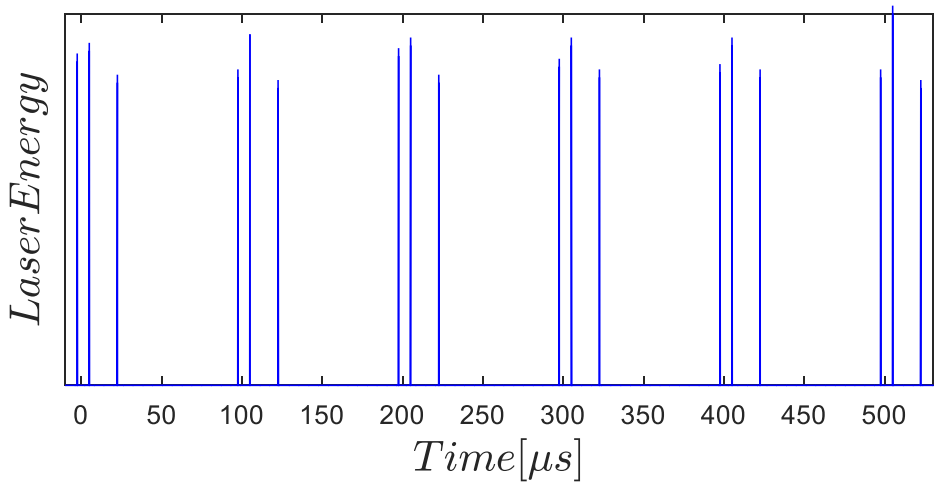

Figure 5. Sample oscilloscope trace from a photo-diode detecting relative laser pulse energy. This trace is for τ_{21} = 7.5 μs. This figure shows uniform energy distributions between and within each set of triplets.

3.3 Turbulent Jet and Bluff-body

A free, circular turbulent jet with a laminar co-flow was chosen to demonstrate the capabilities of the pulse burst laser as well as the triple pulse processing technique. Free turbulent jets contain many small scale structures at short time scales along with a definitive shear layer resulting in strong velocity gradients. The Reynolds number was defined at the jet exit by:

$$Re_{jet} = \frac{U_{exit} D_{jet}}{\nu_{air}} \tag{11}$$

Where U_{exit} is defined as the jet exit velocity, D_{jet} is the jet exit diameter and ν_{air} is the kinematic viscosity of air. At the Reynolds numbers studied (10,000 to 50,000), these flow features would be very difficult to resolve both spatially and temporally using standard planar PIV. The free jet alone along with the jet flow around a cylindrical bluff-body were both studied. The jet orifice diameter was 8 mm, and three different Reynolds numbers were used (10,000, 30,000 and 50,000) throughout the study. This equated to exit velocities of 19.4, 58.2 and 97.0 m/s. The cylindrical bluff-body had an outside diameter of 9.5 mm and it was positioned 10 jet diameters (80 mm) downstream from the exit of the jet. Subsequently, the flow was studied 10 jet diameters downstream for both the free jet and bluff-body cases.

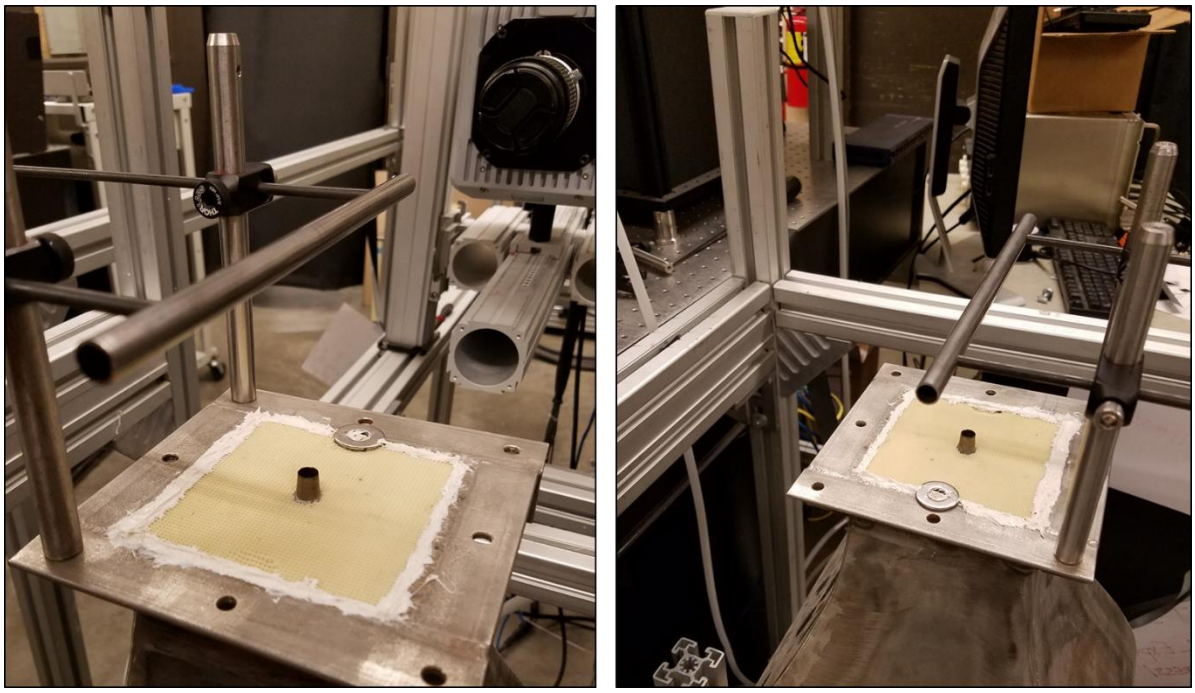

Figure 6. Images of the circular jet and cylindrical bluff-body setup. Cylindrical bluff-body was located 10 jet diameters downstream from the jet orifice. The 10 x 10 cm^2 honeycomb section for flow straightening of the co-flow can be seen surround the jet.

Atomized oil droplets were used for tracer particles. The oil atomizer used a Norgren oil filter and was run in reverse. High velocity air passed over a capillary in the filter, and the high shear rate resulted in micron sized oil droplets. The oil used was bis (2-ethylhexyl) sebacate, 97%. This was selected because of the small diameter particles produced, as well as the low vapor pressure of the oil. Low vapor pressure ensured that residual oil on surfaces would evaporate between runs.

3.4 PIV Setup

The beam was routed through the jet, orthogonal to the imaging plane of the camera. A -30 mm cylindrical concave lens was used to expand the height of the beam and a 500 mm circular convex lens was used to focus and collimate the beam as it passed through the imaging plane. The resulting beam was a 5 cm tall sheet with a thickness of 500 μm. The SA-X2 was mounted orthogonal to the plane of the laser sheet. A 105 mm objective set to an f-stop of 8 was used to achieve a sufficient depth of field such that the entire depth of the laser sheet was in focus. Two different camera positions, resulting in two different magnification levels, were used during data collection (0.326 and 0.206). The first and second camera positions were recorded at a resolutions of 456 x 512 pixels and 328 x 768 pixels respectively. The camera ran at 50 kHz with 20 μs exposure for all data collection configurations, and it was triggered off the 0.2 Hz master timer and synchronized to the delay generator clock at 100 kHz. Bursts from the laser were also triggered off of this same master signal, resulting in one burst every five seconds. The laser was triple pulsed, meaning within each laser burst, pulse triplets were produced at a repetition rate of 10 kHz. Time spacing between the first pulse of each triplet was fixed at 100 μs (10 kHz repetition rate); however, the spacing between the three pulses within each burst could be manipulated to optimize particle images based on the flow Reynold's number.

A variation on the principle of frame-straddling was used in order to place each of the three pulses from the triplet in a separate frame (see Figure 7). Running the camera at 50 kHz and the laser triplets at 10 kHz meant that only three out of every five frames contained information. While this is not desirable, it was necessary to be able to achieve a sufficiently short time spacing between the first and third pulses (τ_{31}) of each triplet. The time between the first and second pulse of each triplet (τ_{21}) was always the shortest time spacing, ranging from 1.5 μs to 7.5 μs depending on flow conditions. Spacing between pulse one and pulse three was held constant at 25 μs. This was the shortest spacing possible given the fixed 50 kHz camera repetition rate. Each of the pulse triplets was captured on three consecutive frames. Two dead frames were then recorded before the camera captured the first pulse of the next triplet. The total burst length was 5 ms, which resulted in a total of 150 pulses per burst. The camera was partitioned in a manner that allowed for the entirety of each burst to be captured in each partition.

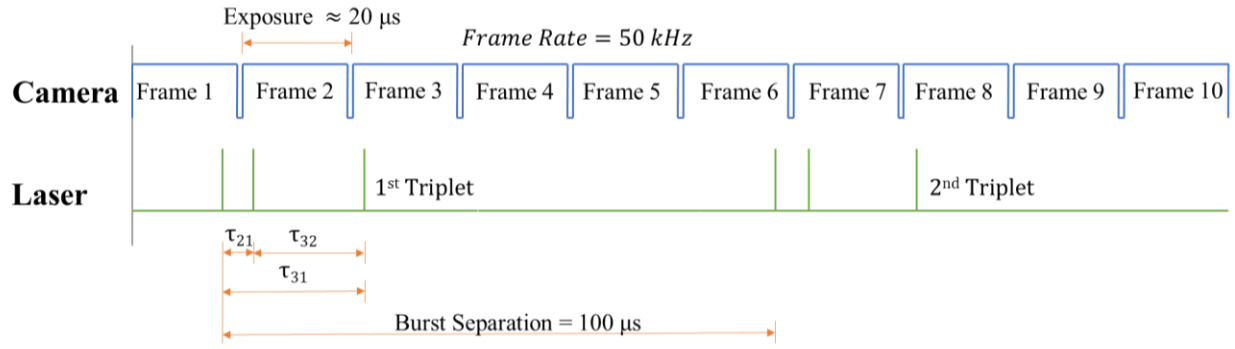

Figure 7. Timing diagram for the pulse burst laser and camera. A variation of frame straddling was used to ensure three consecutive camera frames contained a laser pulse. Two dead frames between each burst resulted due to frame rate limitations given the desired resolution.

CHAPTER 4 PIV PROCESSING

4.1 Overview of Multi-Frame Processing

The multi-frame PIV processing and post-processing algorithm described in this chapter was designed to make best use of the high energy and highly flexible timing capabilities of the pulse burst laser. Processing multiple time spacings for each instantaneous realization allowed for a vast improvement in DVR while also decreasing measurement uncertainty. Correlation plane data was analyzed for every interrogation region, and the ratio between primary and secondary peak was used as metric for correlation strength. This metric became the basis for vector selection.

4.2 Cross-Correlation Processing

Image sequences from the SA-X2 were saved as 16-bit multi-page tiff files. These files were read into Matlab as a 16-bit unsigned integer array. Dead frames preceding the first laser pulse and every subsequent fourth and fifth frame were eliminated, and the data was processed one pulse triplet at a time. As previously mentioned, each burst from the laser produced 150 pulses, which corresponded to 150 camera frames containing particle images and a total of 50 pulse triplets per burst. Each triplet ultimately yielded one instantaneous realization of the velocity vector field, which is why the processing was done one triplet at a time. Each laser triplet contained three potential time spacings. Correlation of the first and second image was referred to as τ_{21}, correlation of the second and third was referred to as τ_{32}, and correlation of the first and third image was referred to as τ_{31}.

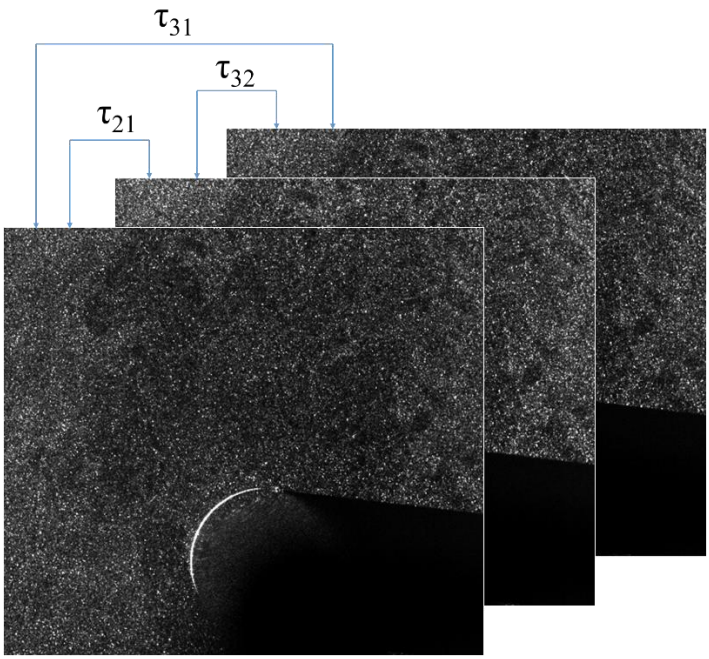

Figure 8. Three example particle images from one laser triplet. Pre-processing included CLAHE and high-pass filtering to improve contrast and decrease noise.

The open source, Matlab based PIV processing code, PIVlab, was used to perform the spatial cross-correlations between frames for each time spacing [35]. PIVlab utilizes the increased processing speed of a fast Fourier transform cross-correlation (FFT-CC) for each image combination. Prior to cross-correlation, images were pre-processed using both contrast-limited adaptive histogram equalization (CLAHE) and high-pass filters. CLAHE filtering improves the contrast of the particles images, and the high-pass filter reduces background noise. Images were then correlated using PIVlab's multi-pass FFT-CC function. This function employs a window-shifting technique that allows for up to 4 passes along with 3-point Gaussian sub-pixel interpolation. Each image pair was processed using two passes with a 50% interrogation region overlap. Interrogation region sizes for each pass were 32x32 px and 16x16 px respectively. Resulting displacement information and cross-correlation plane data for each interrogation region was saved for post-processing.

4.3 Multi-Frame Vector Selection Post-Processing Algorithm

The purpose of the post-processing algorithm that was developed was to determine the optimal vector for each sub-region. Displacement data from each triplet was analyzed one triplet at a time. Within each triplet, three time spacings were correlated, meaning that initially there existed three displacement options for each sub-region in the final vector field (one from each of the three Δt's). If all three vectors for a given sub-region were deemed spurious, that vector space was left void. Vector interpolation was performed when necessary.

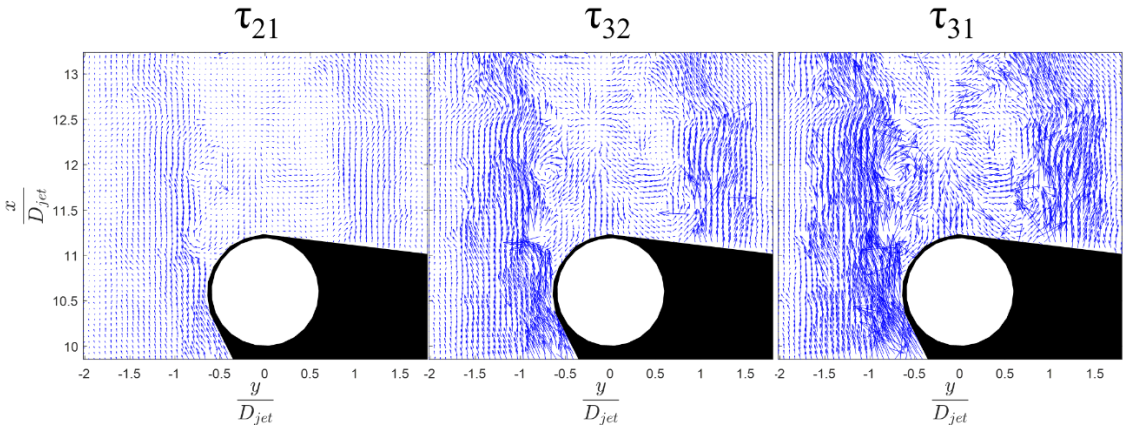

Figure 9. Processed images for each of the three time spacings, prior to any post-processing. Also, this is prior to converting to a common unit system, so vector lengths are still in units of px/frame.

The first step in post-processing was to detect obviously spurious vectors from each of the three individual vector fields. This was done by first setting displacement limits for each vector. Working from the one-quarter rule put forth by Adrian [26], the maximum allowed particle displacement for each sub-region was set to be one-quarter of the interrogation region size. During processing, a two-pass, image-shifting correlation was performed, and the size of the interrogation regions for the second pass was 16x16 pix^2. Hence, the maximum allowable displacement was set to 4 pix/frame. Because multi-pass, window shifting techniques were used during image correlation, the one-quarter could apply to the first pass interrogation region's size

(32x32 pix^2). Due to the large range of time spacings available, limiting max displacement did not result in a large loss of DVR. However, setting this limit did reduce error sources associated with large particle displacements. Initially, a minimum velocity limit was not set for any of the three time spacings. However, after further development of the algorithm, it was discovered the performance was enhanced if displacements less than the uncertainty level (0.1 pixels) for the shortest time spacing were rejected. This is intuitive, as such a small displacement over the shortest time spacing will obviously be better represented by a longer time spacing. Once the velocity limits were set, a standard deviation filter was used over the entire field to further eliminate extreme outliers. The threshold for the standard deviation filter was adjusted based on flow conditions.

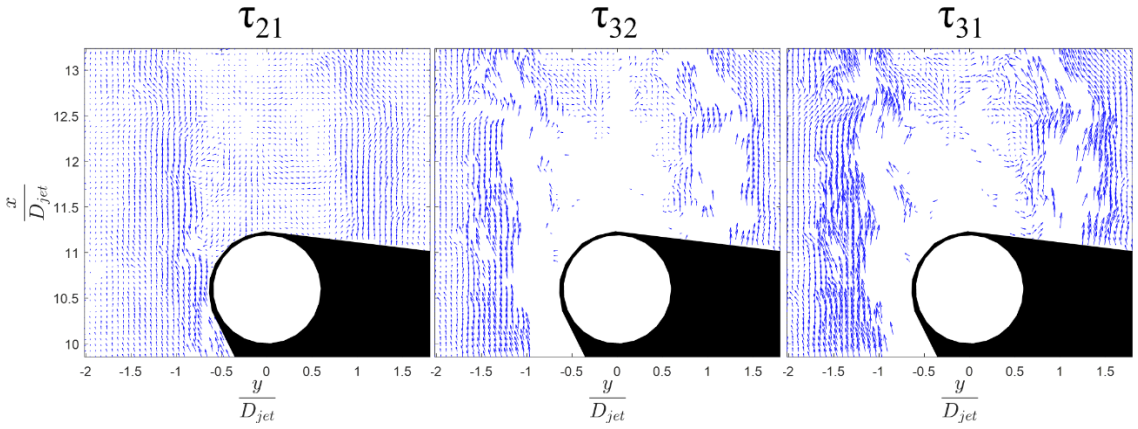

Figure 10. Processed vectors fields following the first post-processing step. Large amounts of vector rejection in τ_{32} and τ_{31} result from large pixel displacements.

Following the spurious vector detection, the three displacement fields were each converted to common units. Up until this point, the x and y components of each velocity vector were given in units of pixels per frame. A calibration image of a metric ruler was used to convert between pixels and meters, and the precise time spacing between each frame was known

with negligible uncertainty. Converting from pixels per frame to meters per second (m/s) made for a true comparison during vector selection.

Once each of the three vector fields were in a common unit, the initial vector selection was performed. Vector selection was based on principles adapted from work done by Xue et al. [43] and Charonko and Vlachos [42]. Both of these papers describe a method for quantifying PIV uncertainty using cross-correlation data. Signal-to-noise (SNR) ratio in the correlation plane is a good metric for the quality of the correlation. Therefore, both of these papers postulate that uncertainty values can be estimated on a vector by vector basis by analyzing the SNR of the correlation. In this instance, SNR is defined as the ratio of the primary peak to the secondary peak following normalization. This principle of strong SNR correlation to vector quality was adapted and used in vector selection. Upon completion of the FFT-CC processing, correlation plane data for each interrogation region was saved along with the displacement vector information. During vector selection, velocity fields from each of the three time spacings were traversed. At each vector location, the corresponding correlation plane data was analyzed for each time spacing. To normalize the data, the minimum value over the entire correlation plane was subtracted. Following this, the primary and secondary peak values were recorded and the ratio between the two was found. Once this was complete for all three time spacings, these three ratios were compared in order to find the optimal time spacing for that given vector location.

Ideally, the peak ratios alone would have been enough to determine optimal vectors. However, several specific instances required special accommodations. First, from synthetic data it was realized that above a certain threshold value of peak ratio, vector quality no longer displayed great improvements with increasing peak ratio. So, should one or more vectors contain peak ratios above this threshold, the most desirable vector would be the one from the

longest time spacing. This ensured that uncertainty was minimized in areas where vectors from multiple different time spacings would have provided sufficient quality. This peak ratio threshold was experimentally determined to be 1.6. Special considerations also needed to be taken for peak ratios that did not meet a minimum value. Similarly to the maximum ratio threshold, peak ratios below a certain threshold value were rejected. Because the peak ratio metric is essentially a measure of SNR, as values near unity, the true displacement becomes indistinguishable from the noise. Experimentally, the optimal value of minimum ratio threshold was found to be 1.2. For a given interrogation region, the vector space was left void if all three vectors possessed peak ratios less than 1.2.

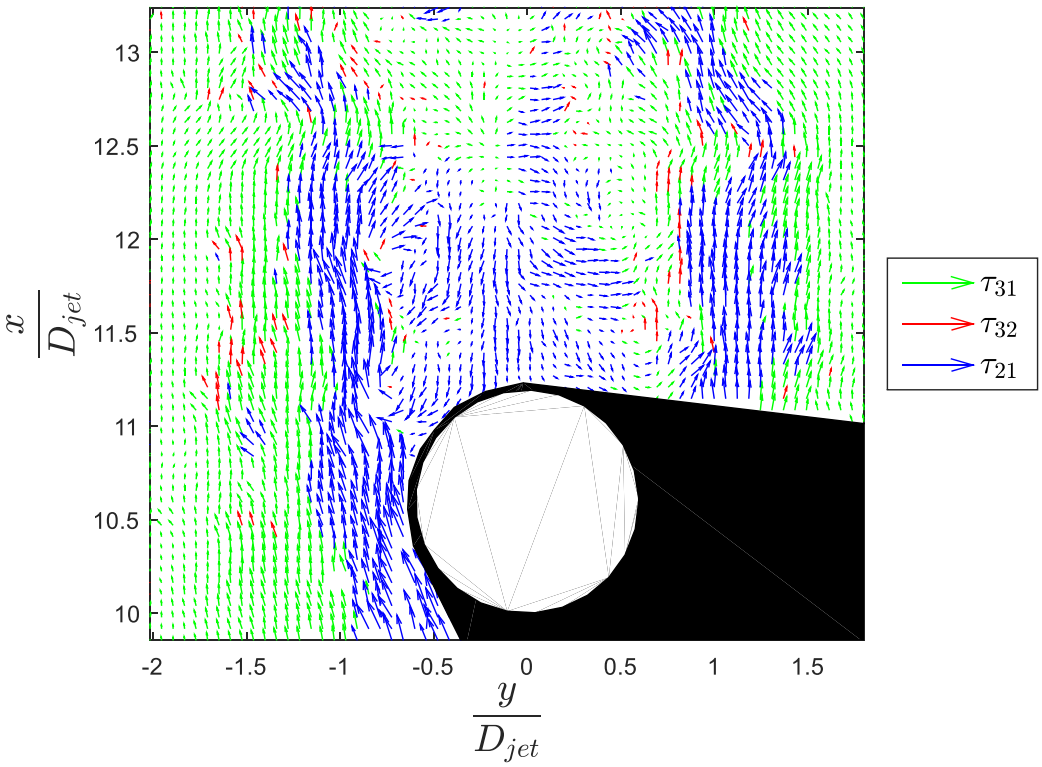

Figure 11. Resulting vector field from the vector selection step. This image is color-coded to display which vectors result from a particular time spacing. Slower velocity regions are dominated by longer time spacings, where the faster regions of the flow are dominated by τ_{21}.

Following the vector selection, the composite vector field was further post-processed. At this point, a sort of median filter was used to determine if there existed a better fitting vector for a given vector space. The median filter used a 5 x 5 kernel to traverse the composite vector field. The vector space at the center of the kernel was compared against the median value of the kernel. Corresponding vectors from the other two time spacings were also compared. Should one of those vectors prove to deviate less from the median of that kernel, it was used to replace the current vector. This part of the post-processing algorithm was used as a way to provide a sort of second pass to the vector selection. A common spurious vector detection method was used to identify poor vectors. However, instead of rejecting these vectors, the algorithm attempted to fill these spaces with better fitting vectors from other time spacings.

At this point in the post-processing, vector selection was completed. Despite all of the steps taken up to this point, resulting composite vector fields still contained spurious vectors. To remove spurious vectors, two common identification techniques were employed. First, velocity limits were set over the entire field. Second, a 3 x 3 median filter identified local outliers. The median filter used was the same that was described in Westerweel & Scarano [37]. Within the 3 x 3 kernel centered at U_0, the median values of all eight neighboring points were calculated (U_m). The residual of each kernel node and the median were found (Equation 12). The median of these residuals (r_m) was then used to normalize the residual of U_0 (Equation 13). To account for fact the residual of U_0 tends to zero in a perfectly uniform kernel, a minimum normalization level (ε) was introduced (Equation 14).

$$r_i = |U_i - U_m| \tag{12}$$

$$r_0' = \frac{|U_0 - U_m|}{r_m} \tag{13}$$

$$r_0^* = \frac{|U_0 - U_m|}{r_m + \varepsilon} \tag{14}$$

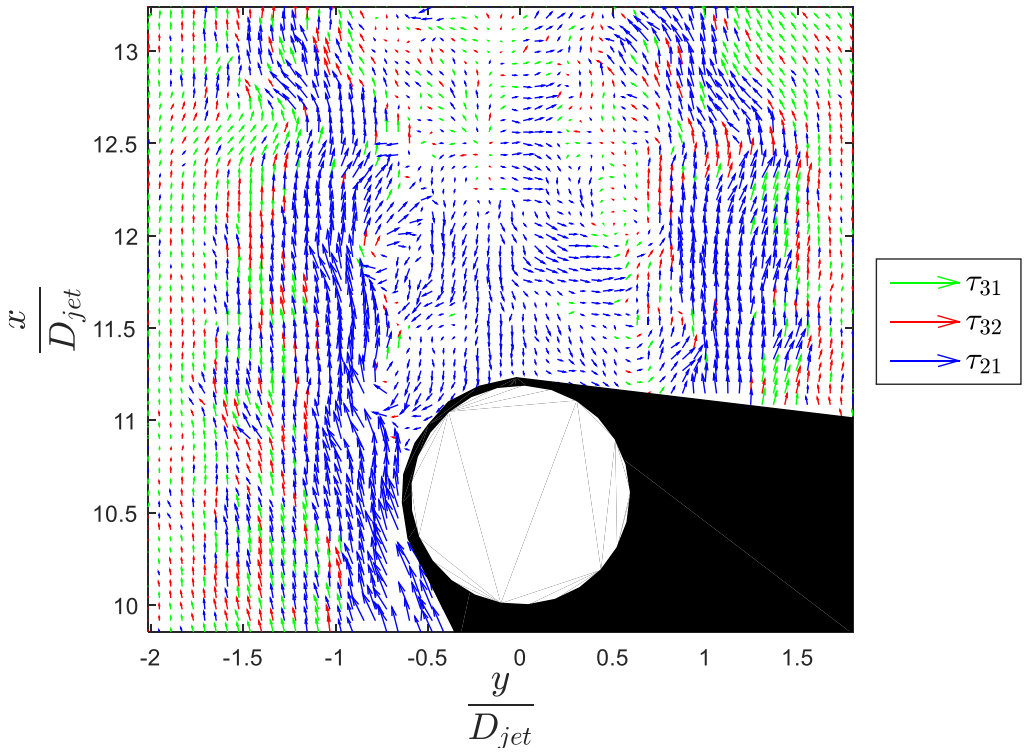

Figure 12. Vector field following the median filtering and second round of vector selection. Again fast regions are dominated by τ_{21}, where slower regions are filled in by τ_{32} and τ_{31}.

The value of ε was set to be 0.1, which corresponds to standard estimates of RMS noise in PIV data [41]. Residual values greater than a predetermined threshold were then rejected. Threshold values varied based on the expected velocity ranges of the flow. Typical values ranged from 4 to 6. Following spurious vector detection and removal, bi-linear interpolation was used to fill in missing vectors.

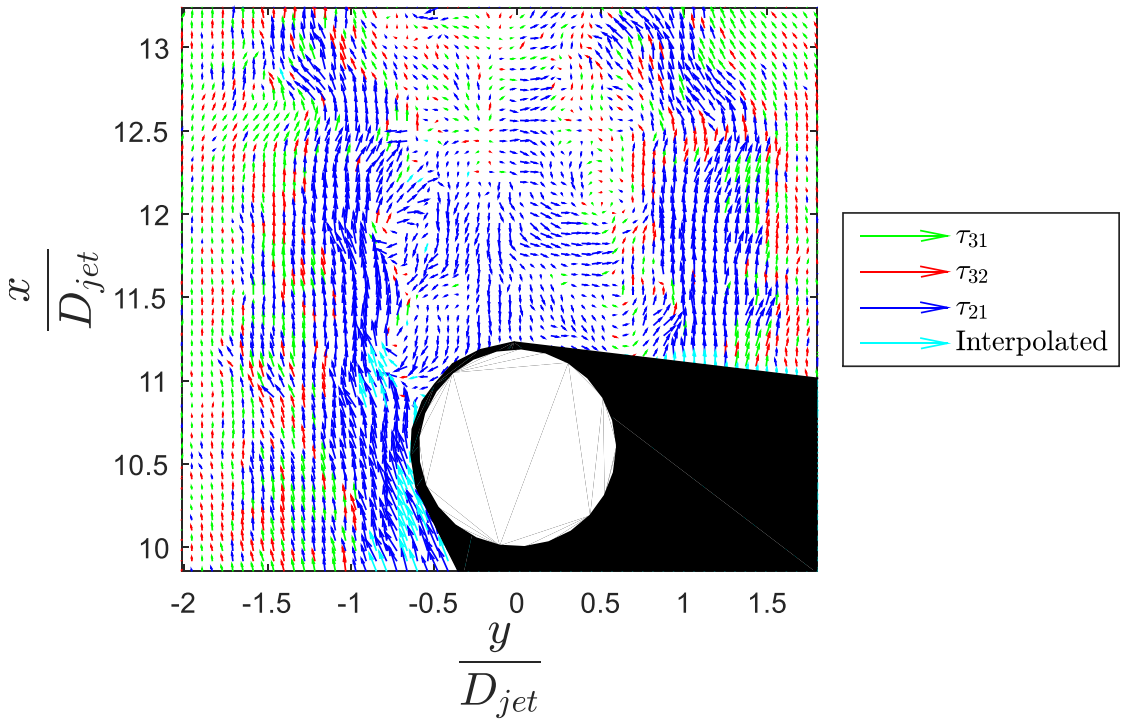

Figure 13. Final vector field, with interpolated vectors.

4.4 Uncertainty Estimation

Despite the advancements in PIV over the past 40 years, *a posteriori* uncertainty quantification of experimental PIV data remains a significant challenge. In recent years, several attempts at uncertainty estimation have been developed, but to this point no standard technique has been accepted. It is still commonplace for a fixed uncertainty estimate to be reported for the entire flow-field. Values for this field uncertainty typically range from 0.05-0.1 [78]. A similar approach was used in this study.

To compare standard PIV processing to the multi-frame algorithm described in chapter 4.3, the same particle images were used for both methods. For standard PIV processing, the first and second images from each image triplet (time spacing τ_{21}) were correlated. The same cross-

correlation processing described in chapter 4.2 was performed, and then spurious vectors were removed using displacement limit and standard deviation filters. No further post-processing was done following the filtering.

It was understood these particle images had uncertainty resulting from data collection as well as processing. It is documented that uncertainty from data acquisition stems from factors such as seed density effects, losses due to in-plane and out-of-plane motion, and velocity gradients. However, quantifying the effect of these factors on the overall uncertainty remains a great challenge in PIV. Because of this, efforts were made during data acquisition as well as during processing to minimize potential error sources. Short time spacings (1.5-7.5 μs) were selected for τ_{21}, which ensured that in-plane and out-of-plane losses as well as gradient effects were minimized. Also, during processing small interrogation regions (16x16 pix^2) were used during the second pass, further minimizing the effect of velocity gradients. Finally, particle displacements were limited by the one-quarter rule. Because two-pass processing with window shifting was used, applying the one-quarter rule to the first pass interrogation region size (32x32 pix^2) would have been acceptable. However, in order to further reduce error, the one-quarter rule was imposed on the second pass region size (16x16 pix^2), which limited the maximum particle displacement to 4 pix/frame. Despite these efforts, undoubtedly there was still uncertainty in the final velocity measurements from experimental factors. However, for the purposes of this study, these effects and their contribution to overall uncertainty were not accounted for using a fixed, whole field uncertainty metric.

Neglecting experimental factors meant sources of uncertainty were simplified to processing error. The primary source of error arose from sub-pixel estimation. Sub-pixel estimators for idealized conditions using synthetic data have produced particle displacement

measurements accurate to 0.01 pix. For actual PIV data, this number increases roughly one order of magnitude. The standard universal constant for PIV error is 0.1 pix [31]. Error studies were performed using synthetic data and those results supported this estimate, so 0.1 px was defined as the measurement uncertainty for the experimental data. Equation 15 and Equation 16 then show the derivation of the velocity normalized uncertainty (δ_{norm}) which was the primary tool used for comparison of processing techniques.

$$\delta_x = \frac{0.1}{\Delta t} \quad \Delta t = \tau_{21}, \tau_{32} \ or \ \tau_{31} \tag{15}$$

$$\delta_{norm} = \frac{\delta_x}{|\bar{V}_{i,meas}|} = \frac{0.1/\Delta t}{\sqrt{{u_i}^2 + {v_i}^2}} \tag{16}$$

4.5 Synthetic Image Generation

To test the post-processing algorithm and also to determine a metric for quantifying uncertainty, a synthetic particle image generator was created. The algorithm was developed in Matlab and it was based on the particle image generator available in PIVlab [35]. Particle image specifics such as image size, particle density, mean particle diameter and size distribution, out-of-plane motion, thickness and noise were specified prior to the image generation. Potential flow equations of shear flows, vortices, etc. were then used to create a fixed velocity field. While spatial gradients were allowed, there was no change in velocity for a given pixel location from frame to frame. Once all of the parameters were properly selected, particles of the desired diameter distribution were randomly created and distributed throughout the image. Particles were also distributed randomly in the z-direction. The depth of this distribution can be thought of as being equivalent to the laser sheet thickness. The theoretical laser sheet was given a Gaussian intensity profile in the z-direction. Because particles were randomly distributed throughout the sheet thickness, this Gaussian intensity profile subsequently controlled each

individual particle intensity. Once the particle field was set, frame sequences of any length could be created. Between each frame, particles were displaced in the x and y directions according to the velocity field created earlier. Finally, Gaussian noise was added over the entire image. The end result was a completely user-specified particle image flow field with user-defined characteristics and noise levels for any number of equally time spaced frames.

In order to validate the multi-frame processing technique, synthetically generated flow fields of a shear flow with a vortex overlay were created. In order to simulate multiple time-spacings, a sufficiently long series of images was generated. Each consecutive image generated had an arbitrary and equal time spacing. Recreating particular triplet time spacing was done by picking specific frames from the equally spaced series. Minimum particle displacements between consecutive frames (corresponding to τ_{21}) were chosen to be smaller than the standard 0.1 px uncertainty. Conversely, maximum particle displacement between the first frame and the frame chosen to represent the third pulse in the triplet (τ_{31}) was set to be larger than the maximum resolvable velocity for the cross-correlation processing. In essence, the DVR of the synthetic flow field was too high for the standard correlation. This ensured that no single time spacing was sufficient by itself for an accurate representation of the velocity field. Error results from the synthetic images will be discussed further in the following chapter.

CHAPTER 5 RESULTS AND DISCUSSION

5.1 Synthetic Data Results

5.1.1 Sub-Pixel Error and Field Uncertainty Calculation

As mentioned in Chapter 4.4, a standard measurement uncertainty of 0.1 pixels was used over the entire field. Synthetic particle images were used to validate this value. Particle images with a fixed displacement in the horizontal direction were generated. Particle displacements varied from 0.01-8 pix/frame. A multi-pass processing scheme with 32 x 32 and 16 x 16 pix^2 interrogation regions was used to correlate each image pair. Each image had a 1024 x 1024 resolution and yielded a total of 16,129 vectors. These vectors were used to plot a distribution and determine a 95% confidence interval. This was done for three different particle image densities. Figure 14 shows the calculated uncertainty as a function of known particle displacement. These results compare favorably to similar studies shown in the literature [27] [38]. Error due to peak-locking is evident, as integer values of displacement result in a greatly reduced uncertainty. The trend for all three curves shows that despite peak-locking error, maximum uncertainty plateaus at around 0.075 px for particle displacements up to 7 pix. While the uncertainty values do oscillate significantly between integer values of displacement, the maximum values remain quite constant over this region. These results show that a whole field uncertainty estimate of 0.1 px is somewhat conservative, but very reasonable.

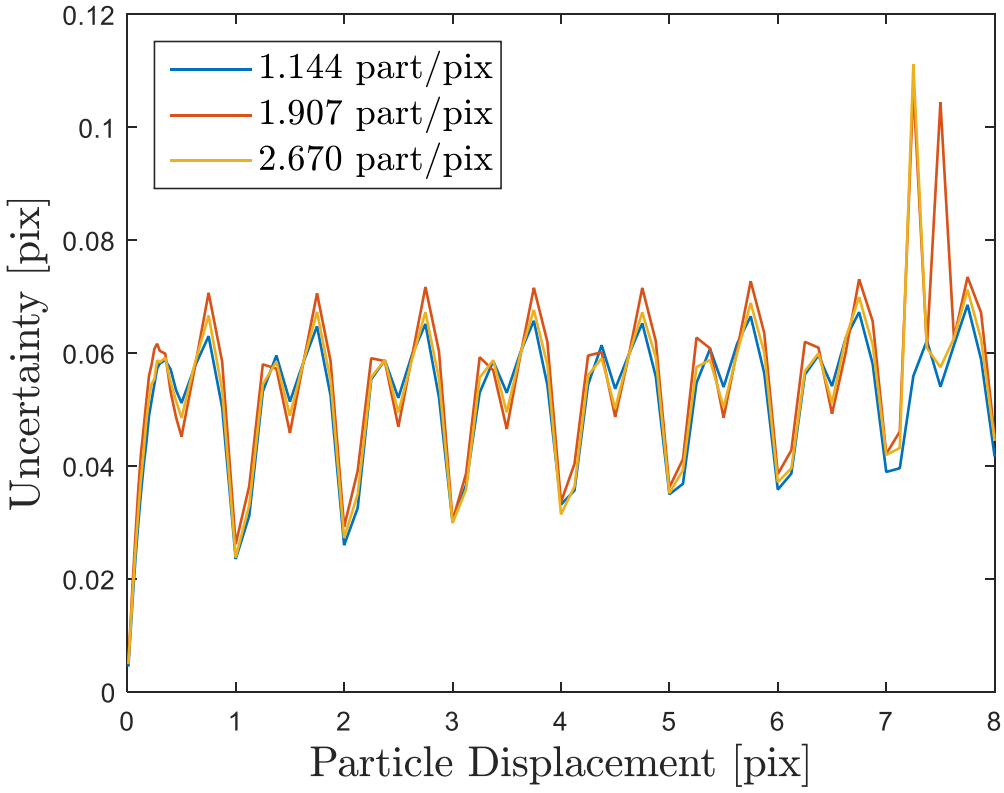

Figure 14. Displacement uncertainty for a 95% confidence interval. Three different particle densities are shown for known particle displacements up to 8 pix. Oscillating pattern is from peak locking effects. It is seen that uncertainty values appear to plateau at around 0.075 px, which means a whole field uncertainty estimate of 0.1 px is conservative but appropriate.

Maximum particle displacements for all empirical data in this study were limited to 4 px. This was done to satisfy the one-quarter rule for a 16 x 16 px^2 interrogation region. Since a multi-pass, window-shifting processing scheme was used to correlate images, the one-quarter rule could have been applied to the first pass interrogation region (32 x 32 px^2), but in order to decrease errors resulting from rotation and gradient effects, the more conservative maximum displacement limit was selected. Short pulse spacings for each test case were optimized to best resolve the high velocity regions of the flow, which often meant that particle displacements in low velocity regions were very small. Figure 15 shows the normalized RMS error given as a

function of particle displacement. RMS error increases dramatically for particle displacements less than 0.5 pix. Results in the following sections show multi-frame processing increased resolution in low velocity regions by correlating longer time spacings, which subsequently reduced measurement uncertainty. Also, despite the conservative maximum displacement limit, DVR increased due to the longer time spacings.

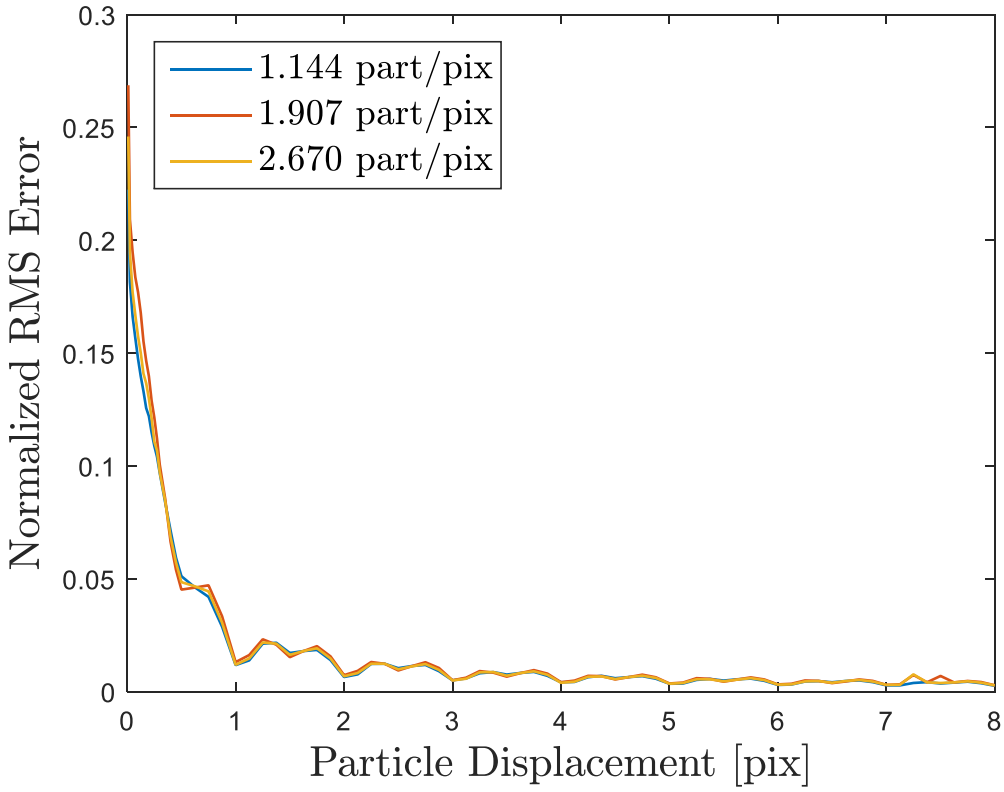

Figure 15. Normalized RMS error given as a function of particle displacement. Error is shown to increase dramatically for pixel displacements less than 0.5 pixels. This is why small pixel displacements were avoided if possible.

Uncertainty results show 4 pixels was indeed a conservative limit. Displacements beyond 7 pixels begin to close in on the maximum displacement limit for a 32 x 32 px^2 interrogation region if the one quarter rule is observed. Measurement uncertainty starts to

increase rapidly for non-integer displacements beyond 7 pix. This result shows longer time spacings could have been used in collecting experimental data, and uncertainty due to processing would have still remained low. Given the turbulent nature of the flows studied, measurement error would have certainly increased with larger particle displacements. A whole field uncertainty metric has no way to account for these errors, thus the conservative displacement limit was selected.

5.1.2 Multi-Frame Processing of Synthetic Image

During development of the multi-frame processing algorithm described in Chapter 4.3, initial tests were performed using synthetic data. Two sets of synthetic images were created, one corresponding to each of the camera resolutions used during data acquisition (512 x 456 and 328 x 768). Both synthetic particle images consisted of a shear flow with a counter-rotating Hamel-Oseen vortex overlaid. The vortex center was positioned below the frame, so the core was not part of the flow field. Ten images were generated for each resolution, which ensured that any ratio of time spacings could be reproduced. The synthetic flow fields were designed in such a way that the maximum particle displacement per frame was slightly less than the maximum allowable displacement for a 16x16 px interrogation region. This meant standard processing of non-consecutive images would result in dropped vectors due to in-plane losses of particle images. Creating images with this specification ensured correlating larger time steps (non-consecutive images) was not resolvable using standard PIV processing. Similarly, the smallest displacement approached zero in the stagnation region of the flow. Surrounding the stagnation point was a region of particle velocities less than the minimum resolvable velocity (0.1 pix/frame). Processing consecutive frames resulted in a large percentage of dropped vectors in

this region due to the small displacement. Table 3 shows the specific details of the synthetic image sets, and Figure 16 shows the actual vector field.

Table 3. Parameters for synthetically generated images. 25 images were generated for each resolution, each having the same settings.

Image Resolution	Maximum Displacement	Particle Density	Average Particle Diameter	Particle Diameter Variation	Gaussian Noise Coefficient
512x456, 328x768	3.5 [px/frame]	0.83 [part/px]	2 [px]	0.15 [px]	0.005

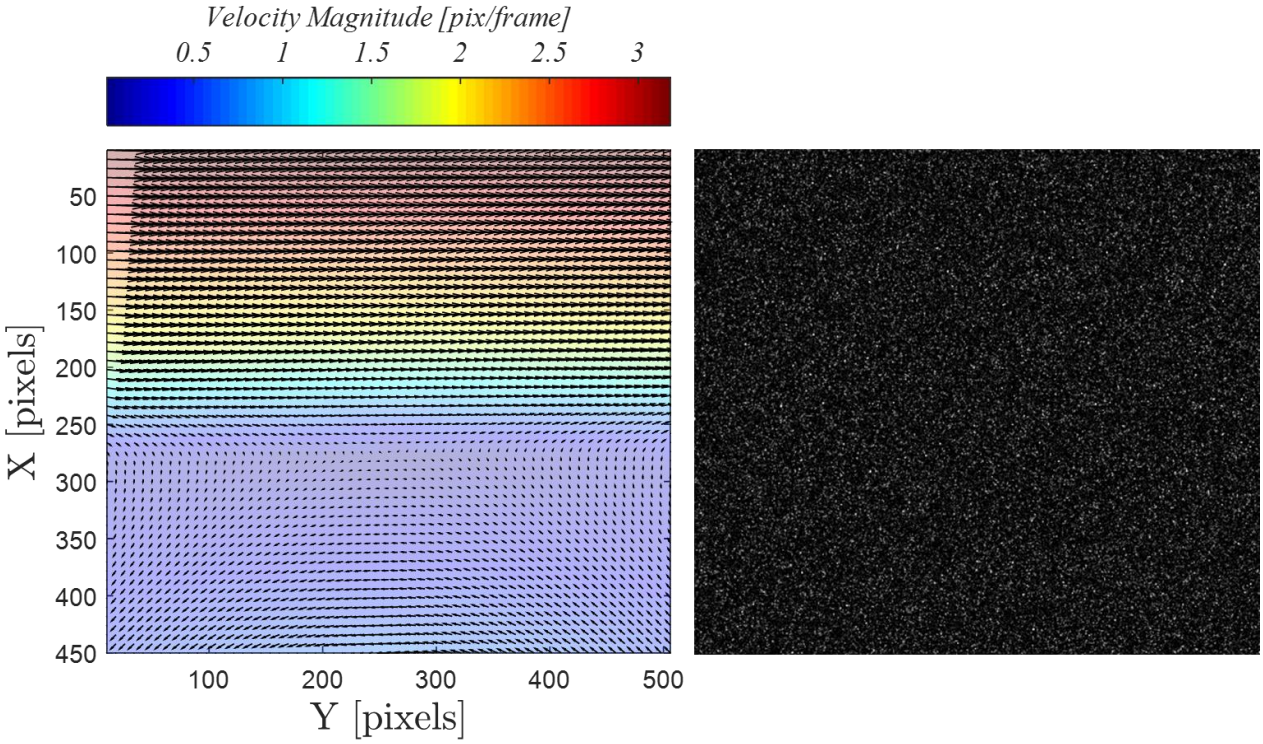

Figure 16. Actual vector field created from potential flow equations (left) and a synthetically generated particle image (right). The most important area of the flow is seen in the center of the frame, where the counter-rotating vortex causes the velocity to stagnate.

Synthetic image sets were analyzed using both standard and multi-frame methods. For standard PIV processing, consecutive frames were correlated using a FFT double-pass cross-correlation. Comparing consecutive frames was representative of correlating the shortest time spacing (τ_{21}) of an image triplet consisting of three time spacings. The multi-frame method used the same FFT double-pass cross-correlation to process three separate frame combinations corresponding to all three time spacings from an image triplet. For the short time spacing (τ_{21}), the first and second frames were correlated. To best represent experimental data, the ratio between short to long time spacing (τ_{21} and τ_{31}) from certain experimental datasets was used in the synthetic data.

$$time\ spacing\ ratio = r_\tau = \frac{dt_3}{dt_1} \tag{17}$$

For a given integer value of the time spacing ratio r_τ, the long time spacing (τ_{31}) correlated the first frame with frame number $(r_\tau + 1)$. As a result, the medium time spacing (τ_{32}) correlated frames two and $(r_\tau + 1)$.

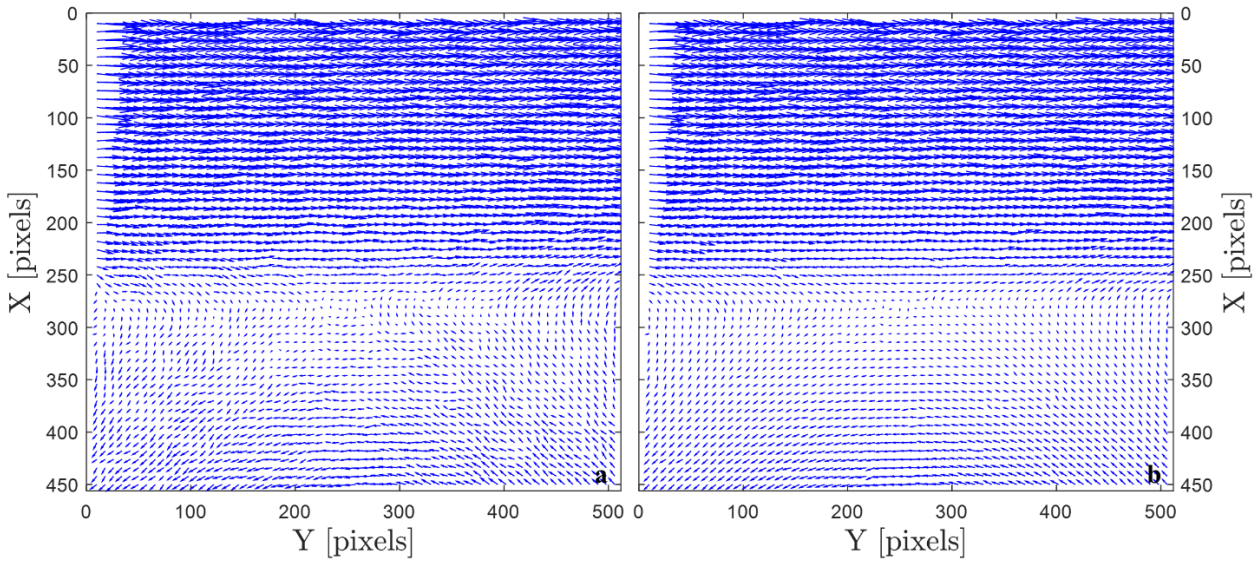

Figure 17. Vector field for r_τ = 5. Processed using (a) standard and (b) multi-frame processing techniques. Standard processing produces random fluctuations in the low velocity regions that are not seen in either the multi-frame processing or the actual vector field.

Figure 17 shows vector field results of a time spacing ratio of 5 for both standard and multi-frame processing methods. Visual inspection of the vector fields showed multi-frame more closely resembled the actual velocity field, particularly in the lower velocity regions. Figure 17b and Figure 18a show that standard processing of low velocity regions produced a fluctuating vector field, which created the illusion of turbulence. These fluctuations result from sub-pixel approximation error due to insufficient particle displacement. This becomes more apparent in Figure 18, which focused on just the stagnation region of the flow. Figure 18 shows how closely the vector field was approximated using the multi-frame processing algorithm, even for average pixel displacements in the region of less than 0.5 pix/frame.

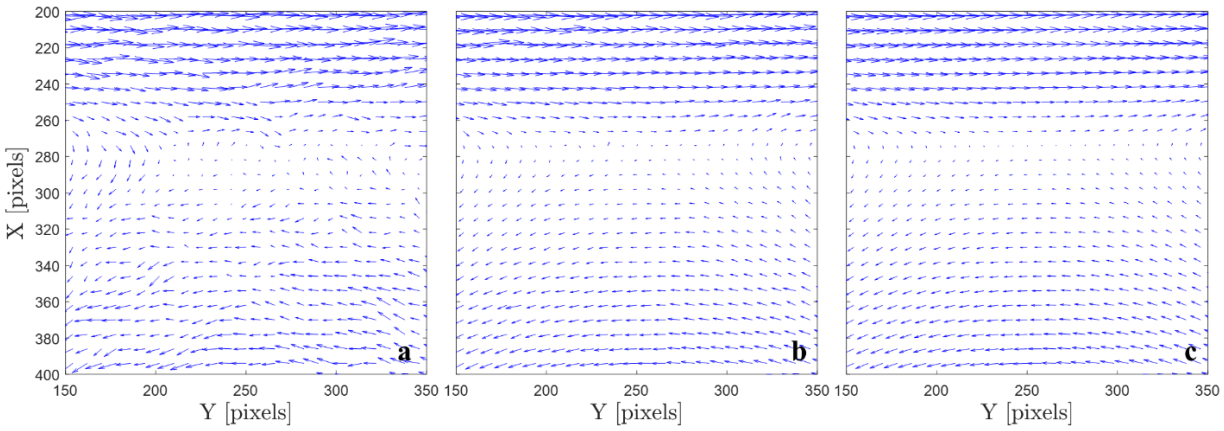

Figure 18. Zoomed views of the stagnation region. (a) standard processing (b) multi-frame processing (c) actual velocity vectors. Random fluctuations are seen in the standard processing. These fluctuations are clearly errors, as they are not seen in the actual vector field. Multi-frame much more closely approximates the actual vector field.

Velocity normalized error (ε_{norm}) maps confirmed the qualitative results from visual inspection of the vector fields (see Figure 19).

$$\varepsilon_{norm} = \frac{\left|\bar{V}_{i,meas} - \bar{V}_{i,act}\right|}{\bar{V}_{i,act}} \tag{18}$$

Figure 19 shows a comparison of the absolute measurement error normalized by the actual velocity for both processing methods. Approaching zero velocity in the center of the stagnation region caused the error to increase dramatically for both processing methods. This was to be expected, as the actual velocities at these points resulted from displacements that were far less than the minimum allowable 0.1 pix, even for the longest time spacing. Visually, it is apparent that multi-frame provided dramatic improvements over standard processing. The lower velocity regions especially show dramatic decreases in normalized error. Despite local velocity gradients and rotational flow, using longer time spacings in slower regions of the flows resulted in vast reduction in error.

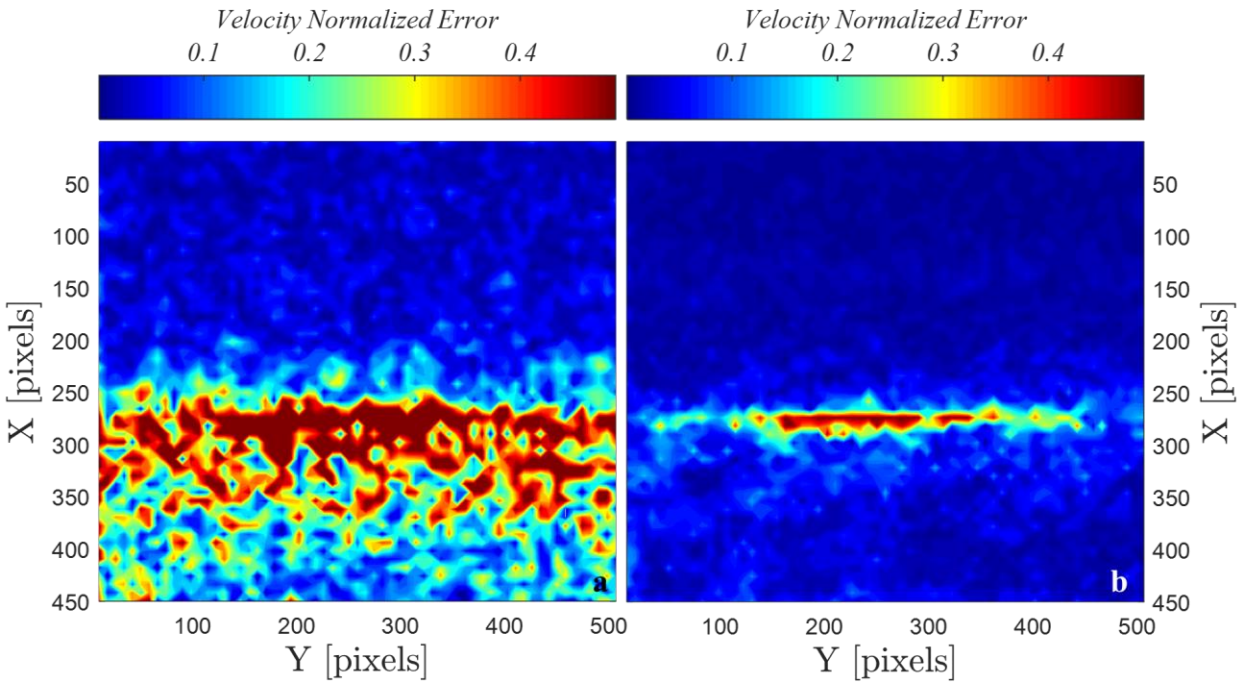

Figure 19. Velocity normalized error of synthetic images. (a) standard (b) multi-frame. Error magnitudes are much higher in for standard processing when compared to multi-frame.

Velocity normalized uncertainty (δ_{norm}) maps were also generated for both processing techniques.

$$\delta_{norm} = \frac{\delta_x}{|\bar{V}_{i,meas}|} = \frac{0.1/\Delta t}{\sqrt{{u_i}^2 + {v_i}^2}} \tag{19}$$

Figure 20 shows a comparison of δ_{norm} between standard and multi-frame processing. The uncertainty maps produced the similar trends to those seen in the error maps from Figure 19. As the flow approached stagnation, the uncertainty increased dramatically. However, similar to measurement error, multi-frame processing produced a much lower uncertainty over the majority of the flow field. Multi-frame processing provided improved resolution of low velocities, leading to increased DVR as well.

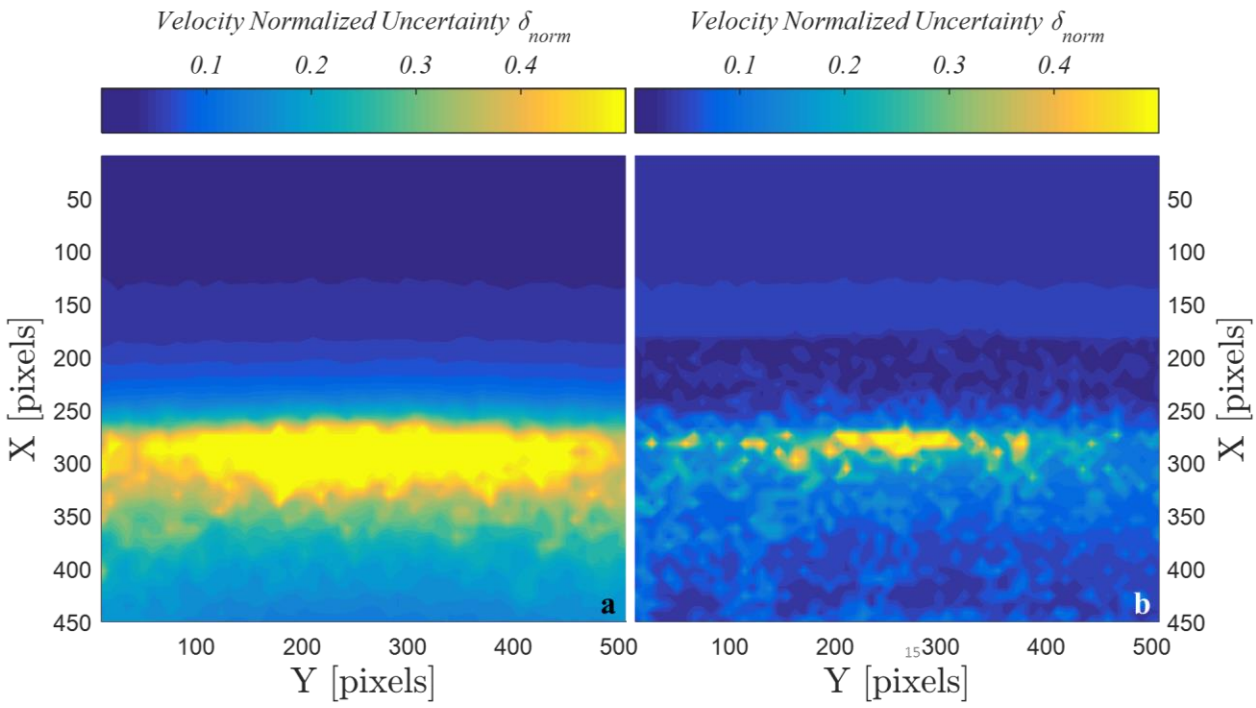

Figure 20. Velocity normalized uncertainty maps. (a) standard (b) multi-frame. Uncertainty results show a similar trend to what is seen in the error results. Large errors are seen in the standard processing, where multi-frame greatly reduces uncertainty.

5.2 Experimental Results

5.2.1 Test Conditions

Experimental PIV data of a turbulent jet was collected in both free jet and cylindrical bluff-body flow cases. Table # contains flow data and time spacing data for each test condition. This test matrix was used for both free jet and bluff-body cases at both magnifications (0.206 and 0.326). For every test condition, 128 laser bursts were collected. Each burst contained 150 pulses or 50 pulse triplets. In total, each test condition yielded 5760 instantaneous velocity field measurements.

Table 4. Testing matrix used during data collection. Each of these Reynolds numbers were run for both camera configurations and both flow configurations.

Re	Jet Exit Velocity [m/s]	Laminar Co-Flow Velocity [m/s]	τ_{21} [μs]	τ_{32} [μs]	τ_{31} [μs]	Burst Length [ms]
10,000	19.4	1.13	2.5	22.5	25.0	5
10,000	19.4	1.13	5.0	20.0	25.0	5
10,000	19.4	1.13	7.5	17.5	25.0	5
30,000	58.2	1.13	1.5	23.5	25.0	5
30,000	58.2	1.13	2.5	22.5	25.0	5
30,000	58.2	1.13	5.0	20.0	25.0	5
50,000	94.0	1.13	1.5	23.5	25.0	5
50,000	94.0	1.13	2.5	22.5	25.0	5
50,000	94.0	1.13	3.5	21.5	25.0	5

5.2.2 Instantaneous Vector Fields and Uncertainties

Instantaneous velocity fields were created using multi-frame processing as well as standard two-frame PIV processing for comparison. Using a second pass of 16x16 pix^2 interrogation regions and 50% overlap resulted in totals of 3528 and 3800 vectors per field for magnifications of 0.326 and 0.206 respectively. Composite vector fields generated by multi-frame processing contained vectors from each of the three time spacings in the given laser triplet. Figure 21 gives an example of a composite vector field where vectors from each time spacing are

color coded. Intuitively, high-velocity regions were best processed using the short time spacings while slower regions were best handled by processing longer interframe times.

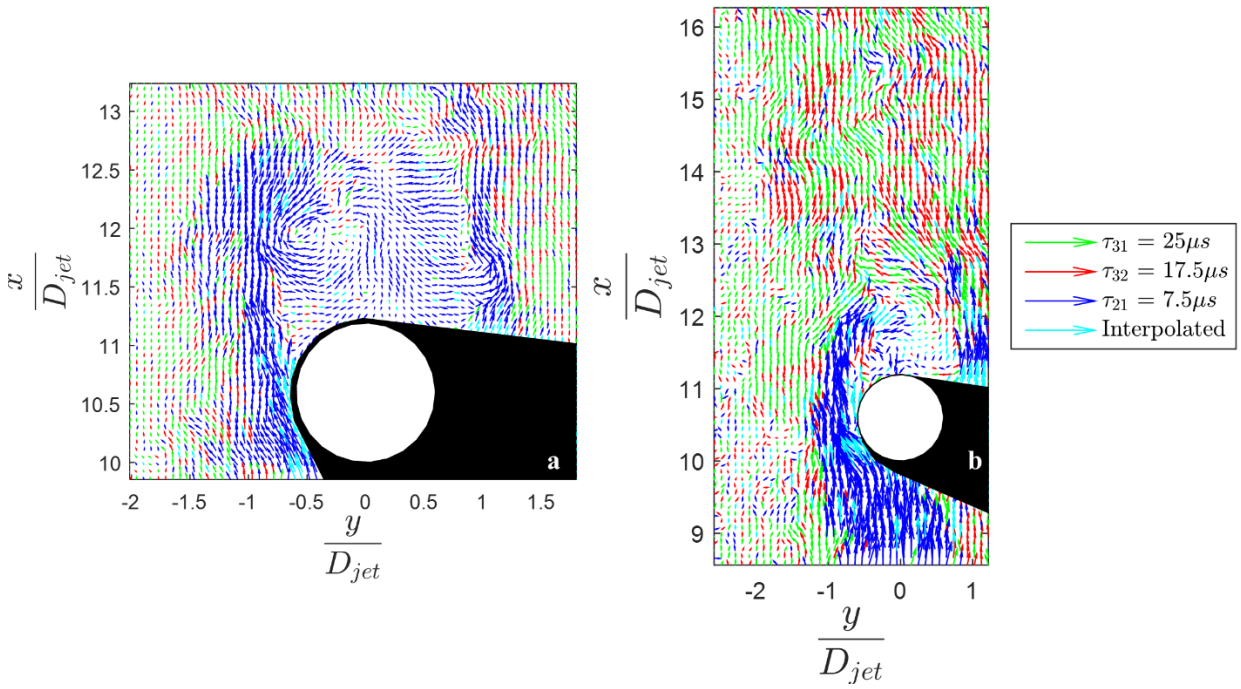

Figure 21. Composite vector field for Re = 10,000 bluff-body flow at a short time spacing τ_{21} = 2.5 μs. (a) shows a magnification of 0.326 and (b) shows a magnification of 0.206. Composite vector fields are color coded to show which time spacing was selected for a particular vector.

Dynamic Velocity Range (DVR) and velocity normalized uncertainty (δ_{nrom}) were the two metrics used to demonstrate the improvements of multi-frame processing. Visual comparisons of flow fields were also used as a qualitative metric for quality. Figure 22 shows a comparison of between multi-frame and standard processing of a Re = 50,000 case. Standard two-frame processing was done using the short time spacing, in order to best capture the high-speed areas of the flow. The turbulent jet at these Reynolds numbers experienced high velocities in the jet core and large velocity gradients in the shear layer. Outside of the shear layer, the flow was laminar and very slow compared to the jet core. Velocity magnitudes are shown in Figure

23, which graphically illustrates the wide range of velocities present in this flow. Standard PIV processing of a flow with a large velocity range proved insufficient.

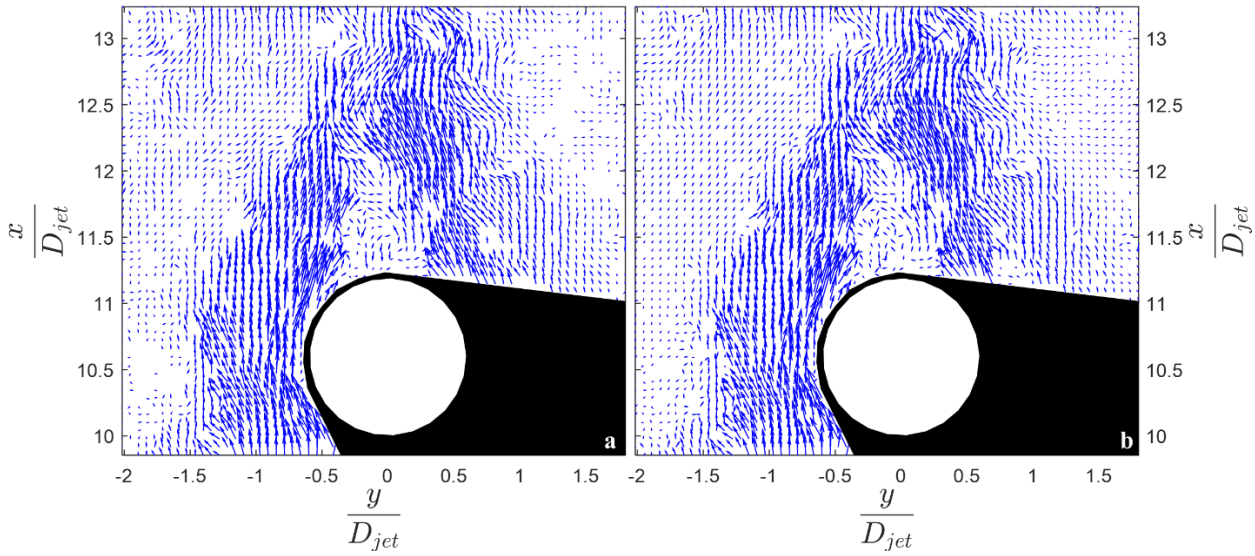

Figure 22. Vector field for Re = 50,000, τ_{21}= 2.5 μs test case. (a) standard (b) multi-frame

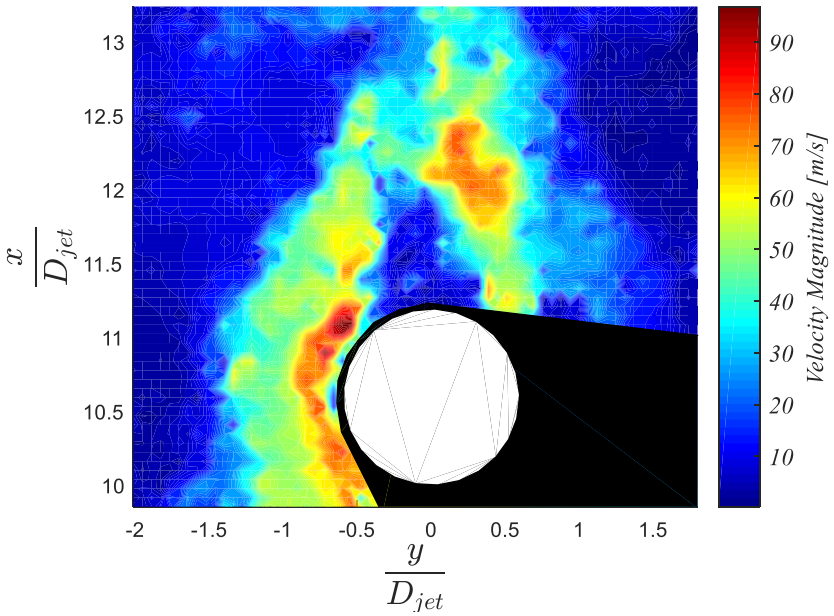

Figure 23. Velocity magnitudes for Re = 50,000 τ_{21}= 2.5 μs test case.

Figure 24 shows expanded windows of the vector fields shown previously in Figure 22. Closer inspection of Figure 24a and Figure 24b revealed vector quality for both methods was high in the large turbulent structure shedding off the cylinder. However, outside the shear layer, standard processing fails to resolve the low velocity, laminar co-flow region. Multi-frame processing utilized longer time spacings (τ_{32} = 22.5 μs and τ_{31} = 25 μs) in the co-flow region which resulted in increased accuracy over the co-flow region.

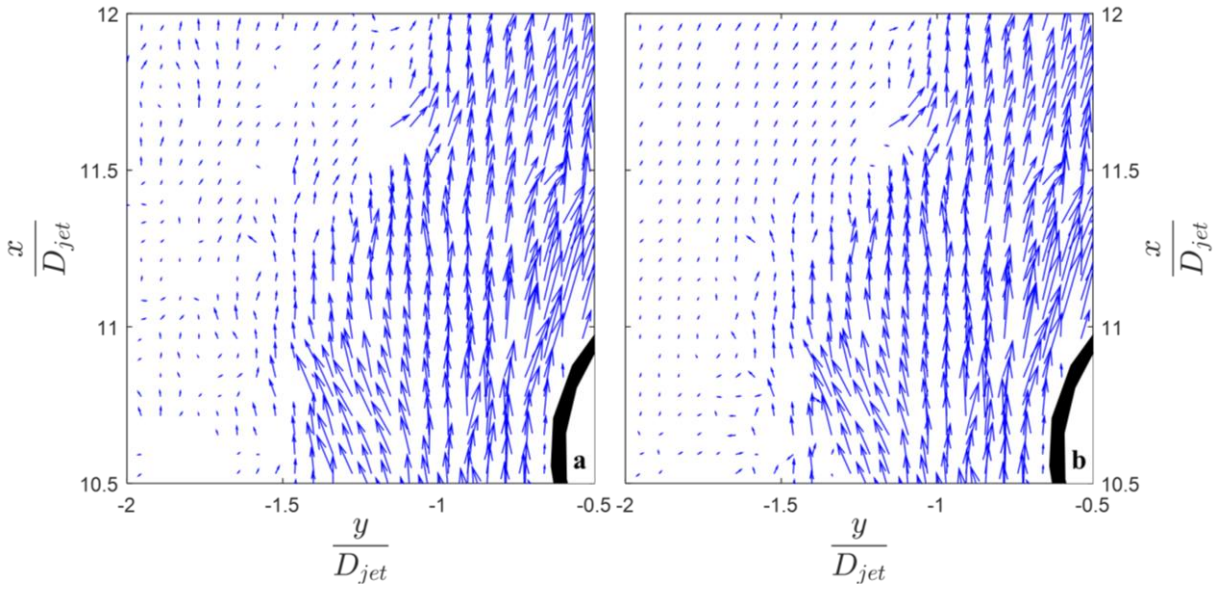

Figure 24. Re = 50,000, τ_{21}= 2.5 μs test case. Zoomed region shows vortex shedding on the left side of the cylinder. (a) standard (b) multi-frame. Random fluctuations are seen in the standard processing of the low velocity regions. These fluctuations are not seen when using multi-frame processing.

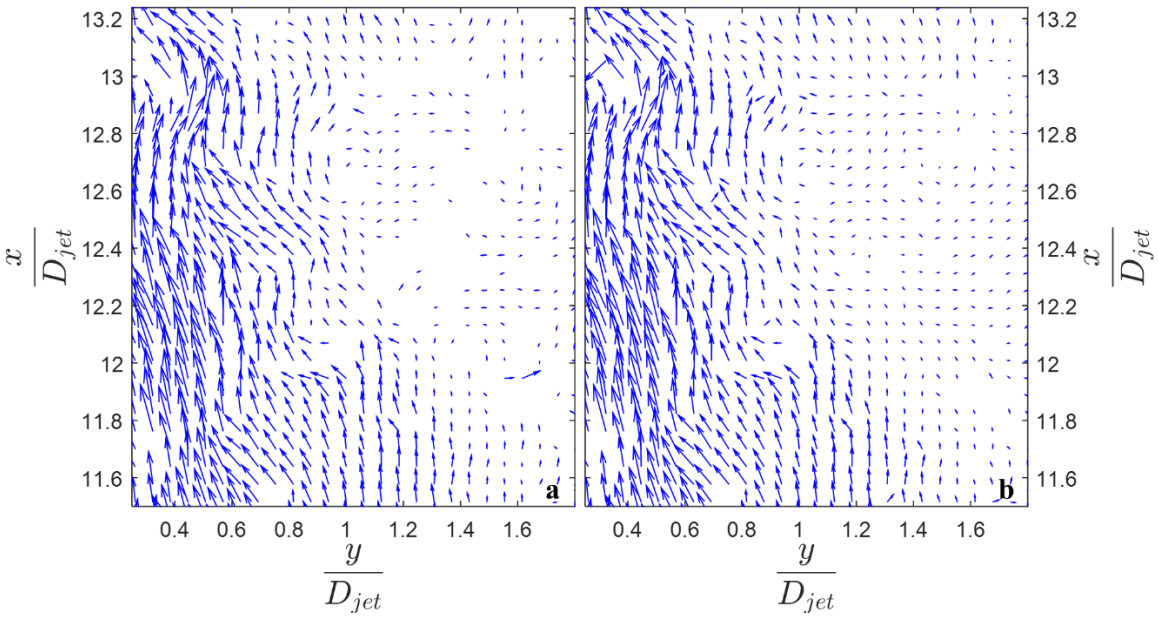

Figure 25. Re = 50,000, τ_{21}= 2.5 μs μs test case. Zoomed region shows extreme low velocity region on the right side of the cylinder, approximately 1 jet diameter downstream. (a) standard (b) multi-frame. Large amounts of dropped vectors are seen in low velocity regions when using standard processing. Much better vector fill is achieved when using multi-frame processing.

Figure 24b shows similarities to the standard processing of stagnation region in the synthetically generated velocity field shown in Figure 18a. The expanded window of the synthetic image showed standard processing of such small particle displacements produced random fluctuations in the resulting flow, which introduced large amounts of error. A similar behavior is seen in the upper left hand corner of Figure 24a and on the right hand side of Figure 25a. This region of the flow appears to be dominated by small scale turbulent structures. However, based on synthetic results, this fluctuating phenomenon is more likely random error introduced by sub-pixel estimation error of small particle displacements. Multi-frame processing of this same region produced a much more uniform velocity field. Again, this correlates well to the synthetic data shown in Figure 18b. A uniform vector field in the region of the flow also seems logical given this sample was taken from the laminar co-flow.

Multi-frame processing did not allow particle displacements less than the minimum resolvable displacement limit (σ_{min}), which was defined to be 0.1 pix/frame. For the standard processing scheme, no such limit was set. The only post processing steps administered to the standard method were standard deviation and median filtering to remove spurious vectors. Despite not having a minimum displacement limit, standard processing saw a large percentage of dropped vectors in the co-flow regions. As mentioned before, it was observed that in these low velocity regions, standard processing produced random fluctuations that were most likely incorrect representations of the actual flow field. Figure 26 shows results from a 10 x 10 vector region for both processing methods. Mean pixel displacements over the region of 0.34 and 1.67 pixels were found for standard and multi-frame processing respectively. In the multi-frame processing case, longer time spacings resulting in larger particle displacements produced a much more uniform field. However, while mean particle displacements were more than ten times that of standard processing, displacements were still limited to under 1.5 pix. Despite the time spacings used to measure these displacements were roughly ten times τ_{21}, particle displacements were not exceeding the maximum allowable velocity. However for standard processing, such small particle displacements will naturally lead to increased error. Figure 15 shows the normalized RMS error for particle displacements less than one pixel increases dramatically. The large error associated with such small displacements almost certainly is responsible for the fluctuations and dropped vectors shown in the standard processing data. However, the increased DVR of multi-frame processing allowed for vectors from longer interframe times to fill in the gaps. In this particular test case, the time spacing ratio was 10, which equated to a theoretical increase in DVR from standard to multi-frame of 10.

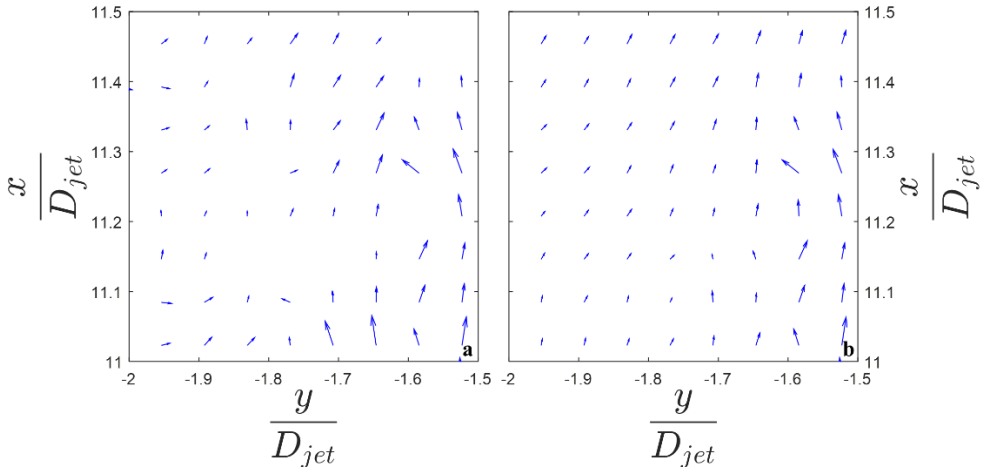

Figure 26. 10 x 10 samples of a low velocity region from the Re = 50,000, τ_{21}= 2.5 μs test case. (a) standard processing produced a mean pixel displacement of 0.34 pixels, while (b) multi-frame processing produced a mean of 1.67 pix.

Table 5. Mean velocity range and dropped vector rates for multi-frame and standard processing schemes, given optimal τ_{21} value at each flow condition

Re	τ_{21} [μs]	Flow Type	Percentage of Dropped Vectors [%]	
			Multi-Frame	Standard
10,000	7.5	Bluff-body	9.8	16.6
30,000	2.5	Bluff-body	6.7	21.9
50,000	2.5	Bluff-body	11.1	21.3
10,000	7.5	Free Jet	4.8	9.8
30,000	2.5	Free Jet	6.7	22.2
50,000	2.5	Free Jet	16.2	20.9

The Re = 50,000, bluff-body flow case shown previously, contained the maximum velocity range of any flow studied. As a result, the benefits of multi-frame processing were most evident in those vector fields. However, multi-frame processing still showed improvements over standard processing for both Re = 30,000 and Re = 10,000 cases. Table 5 shows improvement in dropped vector rates for all Reynolds numbers. Qualitative results can also be made by observing the flow field. Figure 27 shows an instantaneous vector field from the Re = 10,000,

τ_{21} = 7.5 μs test case. The range of velocities present in Re = 10,000 test cases was better covered by standard processing's DVR, resulting in lower dropped vector percentages. However, fluctuations are still seen in the co-flow region. Again, multi-frame produced superior results in these regions of the flow.

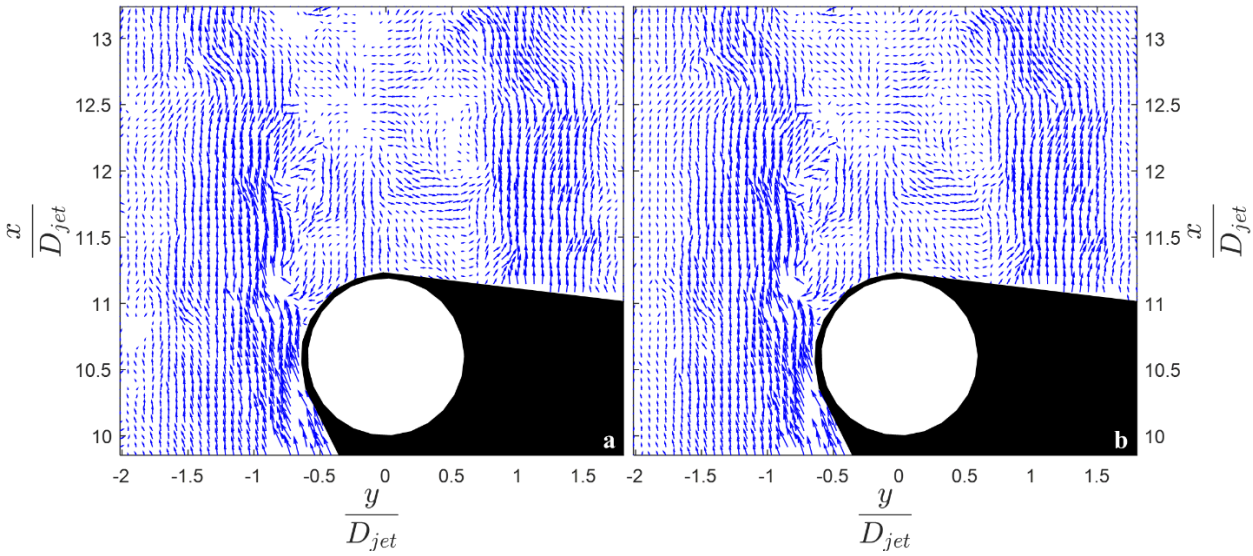

Figure 27. Instantaneous vector field for the Re = 10,000, τ_{21} = 7.5 μs test case. (a) standard (b) multi-frame. Higher fluctuations and dropped vector rates are seen in the standard processing image when compared to multi-frame.

For the free jet cases, vector fields processed using the multi-frame scheme still showed improvements to standard processing for each Reynolds number. The free jet flows did not contain the same level of turbulence due to the lack of an obstruction. The large coherent structures present in the bluff-body flows were not present in the free jet. However, due to the decrease in turbulence, the low velocity co-flow region was mostly unperturbed, which resulted in extremely low velocity regions along the periphery of the frame. These low velocities along with gradient effects in the shear layer led to increased dropped vector rates with standard processing. An example flow field comparison from a Re = 50,000 case is shown in Figure 29.

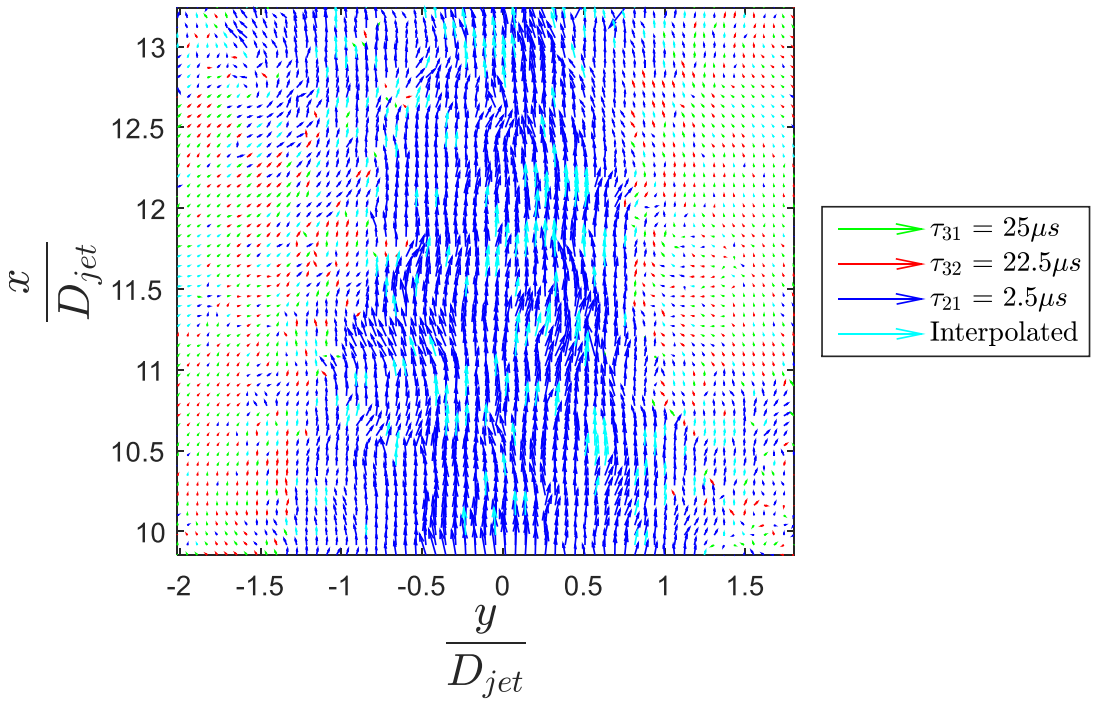

Figure 28. Final composite image for one instance of the Re = 50,000, τ_{21} = 2.5 μs test case. Time spacing selection is color-coded. Color-coding corresponds to time spacing.

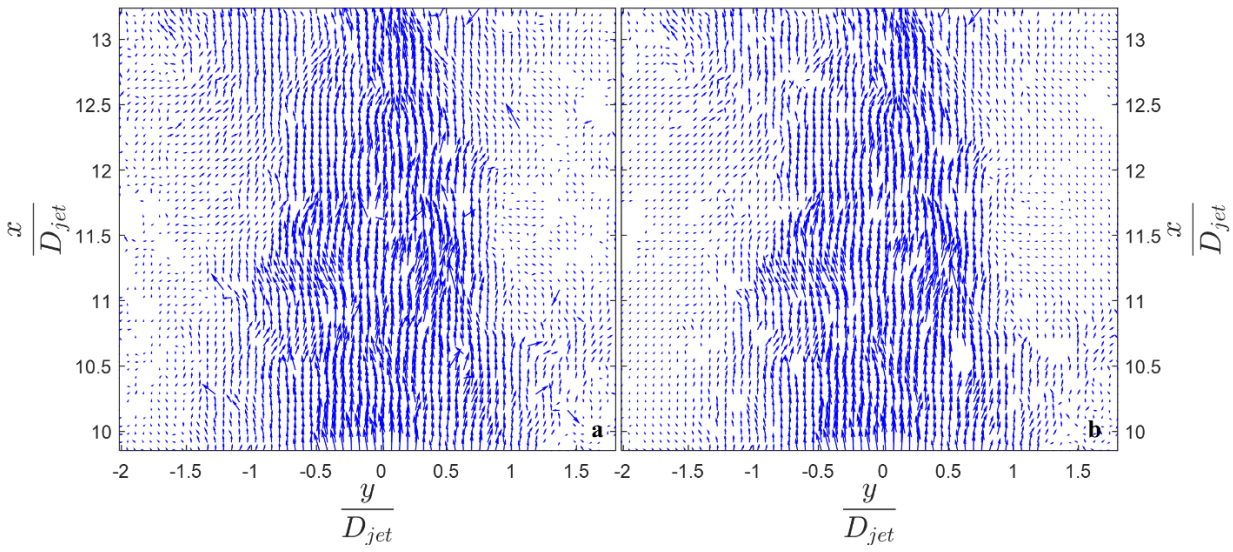

Figure 29. Instantaneous vector field for the Re = 50,000, τ_{21} = 2.5 μs free jet test case. (a) standard (b) multi-frame. Similar trends are seen in the free jet case when compared to the bluff body flow.

Free jet test cases of each Reynolds number should have proved to be less challenging to process than their bluff-body counterparts. The decrease in vortical motion present in each flow greatly reduced potential sources for dropped vectors. However, for certain instances, dropped vector rates actually increased for the free jet case. This was likely due to the decreased seed density present in the jet core. As mentioned in chapter 3.5, the co-flow was seeded and the interrogation area was positioned 10 jet diameters downstream to allow for turbulent mixing to evenly disperse seed particles throughout the flow. Visual inspection of particle images for the free jet showed a decreased seed density along the centerline. These results suggested the axial position of the interrogation area was not sufficiently far downstream from the jet exit. Low seed densities were not experienced along the centerline in the bluff-body cases. This was most likely due to the cylinder aiding in turbulent mixing, which resulted in more entrainment of seed from the co-flow. These effects were most noticeable in the Re = 50,000 test case. For Re = 30,000 and Re = 10,000 these seed density effects rarely affected vector detection in the jet core. While this loss in seed density did affect total drop rates, the overall drop percentage for multi-frame processing was still low. This meant the images were still high enough quality to produce PIV data which accurately represented of the flow field.

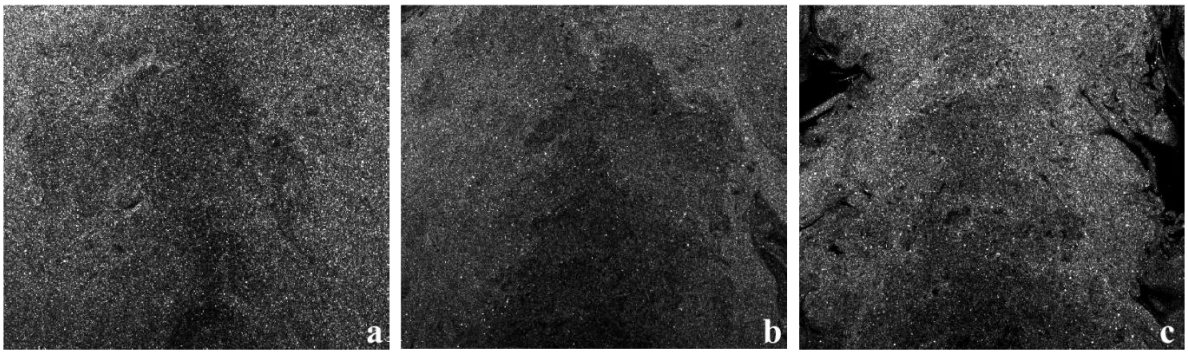

Figure 30. Free jet particle images for (a) Re = 10,000, (b) Re = 30,000 and (c) Re = 50,000. Noticeable centerline seed density decrease for each case.

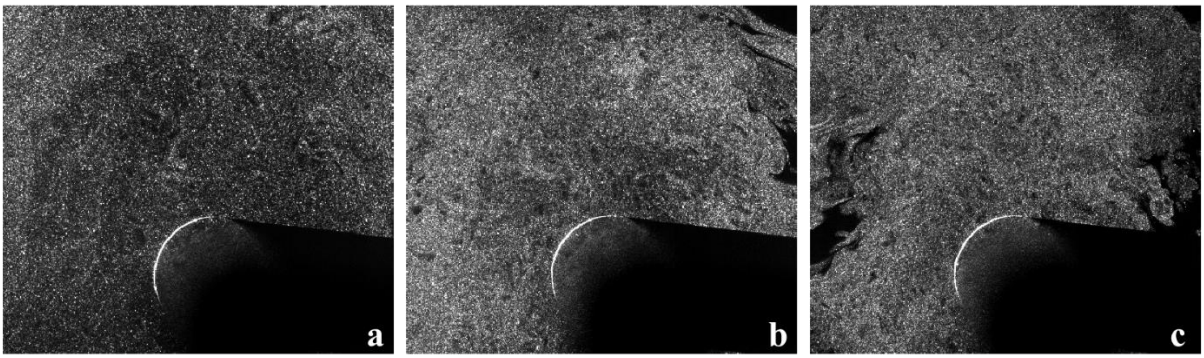

Figure 31. Bluff-body particle images for comparison. (a) Re = 10,000, (b) Re = 30,000 and (c) Re = 50,000. No noticeable seed density decrease on the centerline.

Instantaneous Velocity-Normalized Uncertainty

Instantaneous velocity-normalized uncertainty (δ_{norm}) maps were generated along with the vector fields for each test condition. Results for the Re = 50,000, τ_{21} = 2.5 μs test case are shown in Figure 32. Qualitative results from visual inspection of the flow field in Figure 22 were supported by the normalized uncertainty field. Uncertainty was low for standard processing in high velocity regions, which was to be expected due to the short 2.5 μs time spacing used in the correlation. However, in the co-flow regions as well as the stagnation region

behind the cylinder, standard processing uncertainties rapidly increased to unacceptable levels. In comparison, multi-frame processing performed identically to single frame in high velocity regions, but longer time spacings allowed for uncertainty to be decreased up to one order of magnitude in the co-flow and stagnation regions. This resulted in a much more uniform uncertainty field.

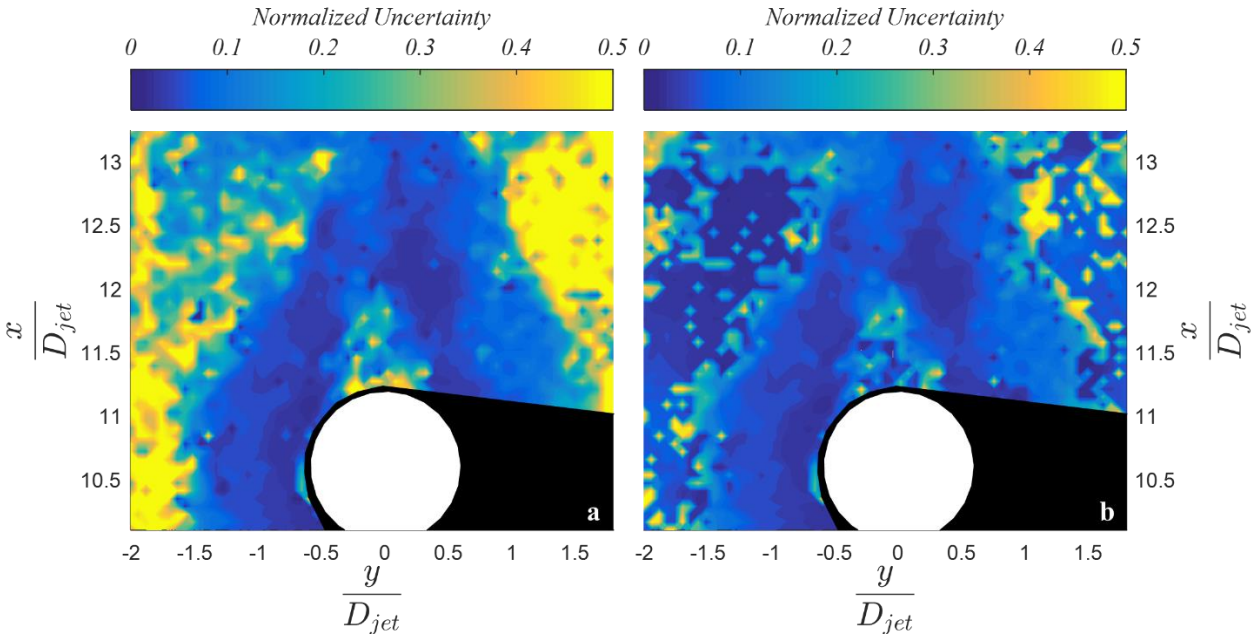

Figure 32. Velocity normalized uncertainty plots for Re = 50,000, τ_{21} = 2.5 μs test case. (a) standard (b) multi-frame. Uncertainty plots confirm the qualitative results seen in the instantaneous vector fields.

Similar results were seen for all Reynolds numbers, all of which supported the conclusions drawn from visual inspection of the flow fields. For low Reynolds number bluff-body flows, the lower uncertainty regions developed a distinct separation directly behind the cylinder, which corresponded to the large recirculation zone seen at this jet velocity. Recirculation and stagnation directly behind the cylinder caused fluid velocities to drop to near zero. Particle displacements were too small to resolve in this region, which was evident by the

vector field comparison. Due to insufficient particle displacements, uncertainty in this region increased dramatically. This recirculation zone was significantly smaller for the higher velocity flows. As a result, mean uncertainty for the Re = 10,000 case did not improve when compared to either the Re = 30,000 or Re = 50,000 test cases.

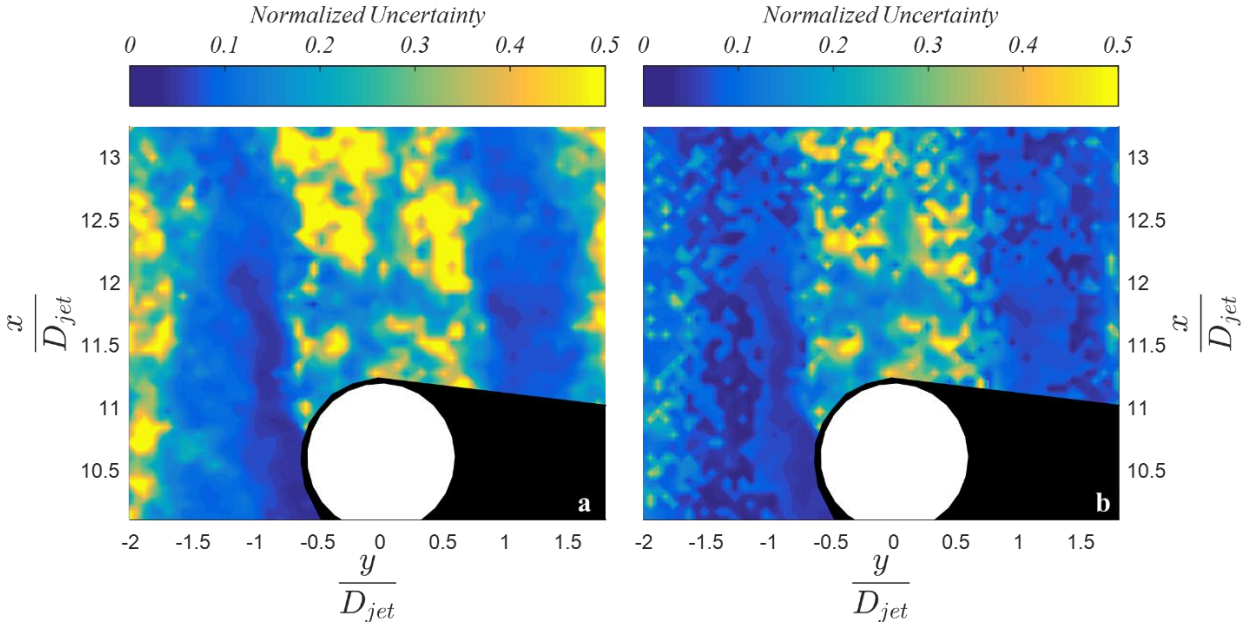

Figure 33. Velocity normalized uncertainty plots for Re = 10,000, τ_{21} = 7.5 μs bluff-body test case. (a) standard (b) multi-frame. Very similar results seen for all Reynolds numbers.

Velocity-normalized results for the free jet test cases again quantified the conclusions drawn from the vector field analysis. Figure 34 shows an instantaneous uncertainty map for the Re = 50,000, τ_{21} = 2.5 μs test case. Uncertainty improvement in the co-flow as well as shear layer was dramatic. This type of uncertainty decrease was noticed for every Reynolds number.

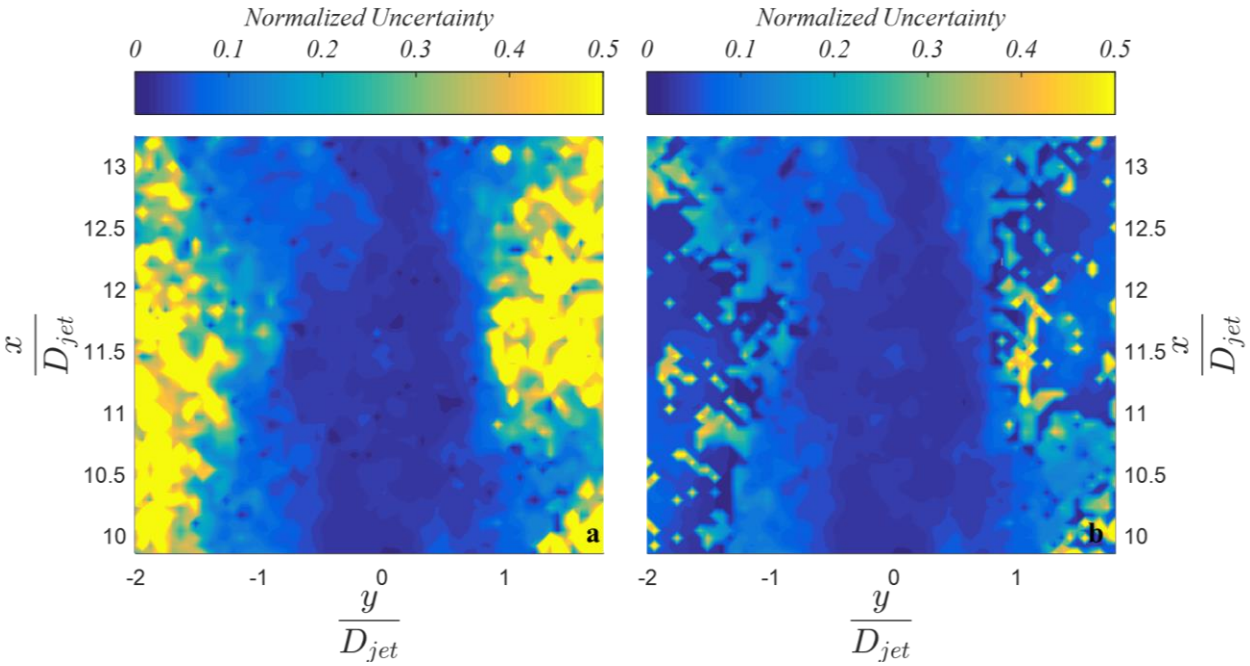

Figure 34. Velocity-normalized uncertainty plots for Re = 50,000, τ_{21} = 2.5 μs free jet test case. (a) standard (b) multi-frame. Free jet results show similar trends to those seen in the bluff body cases.

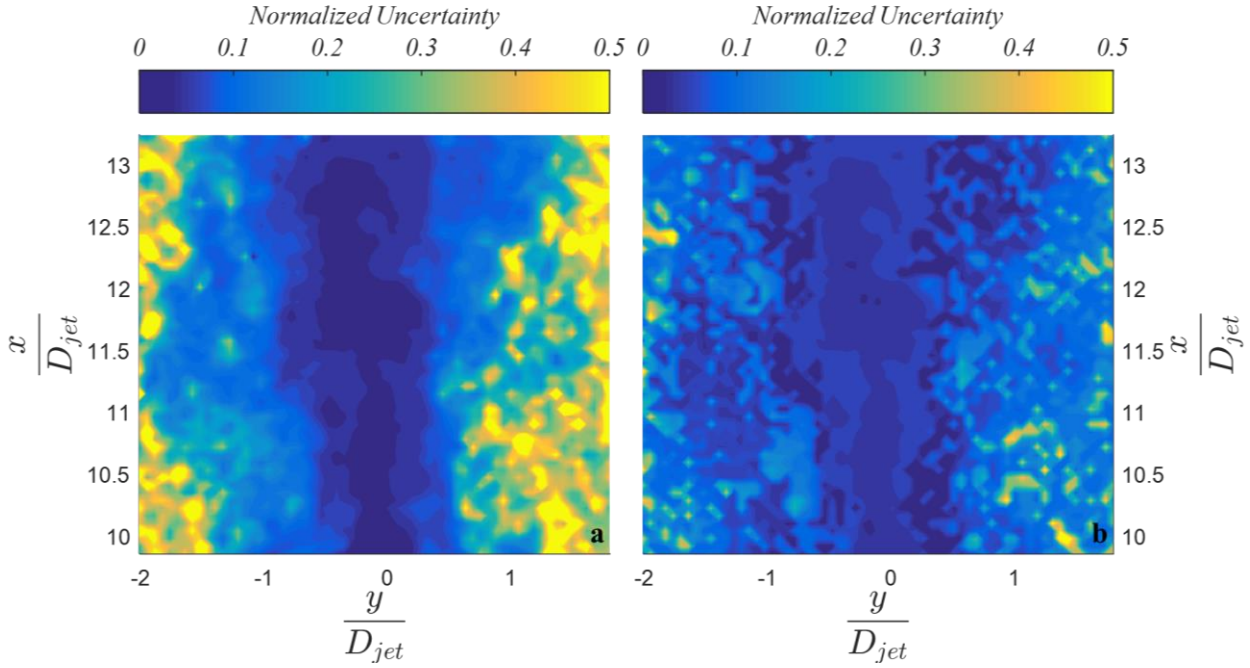

Figure 35. Velocity-normalized uncertainty plots for Re = 10,000, τ_{21} = 7.5 μs free jet test case. (a) standard (b) multi-frame.

Instantaneous realizations of all flow cases demonstrated decreased uncertainty and increased DVR with multi-frame processing. Standard processing techniques will always be limited by the sub-pixel accuracy. Vector fields produced by standard processing showed increased dropped vector rates and increased uncertainty in low velocity regions of the flows. Multi-frame processing was also limited by sub-pixel accuracy, but low velocity areas were better resolved using longer time spacings. Longer time spacings allowed larger particle displacements resulting in an increased likelihood of producing a strong correlation. However, other error sources were introduced with increased particle displacement. These errors stemmed from non-uniform particle displacements across the interrogation region (velocity gradients). Using small interrogation regions minimized these effects, but gradients remain a challenge for all types PIV processing.

5.2.3 Time Averaged Results

For each test case, a total of 5760 instantaneous realizations were collected. This was more than enough to produce statistically converged time averaged data. Time averaging of normalized uncertainty showed multi-frame processing produced consistent and definitive improvements over standard processing. Comparing these uncertainty field to mean velocity fields provided more insight into the strengths and weaknesses of each processing method. Figure 36 and Figure 37 show time averaged axial velocity and uncertainty respectively for the Re = 10,000, τ_{21} = 7.5 μs test case. In this instance, uncertainty values were comparable in areas of high velocity, but multi-frame greatly decreased uncertainty in low velocity regions. Standard processing consistently produced uncertainty values one order of magnitude larger than multi-frame for the co-flow and stagnation regions. Multi-frame processing did show increased

uncertainty in the recirculation area directly downstream from the cylinder. However, this was not an unreasonable result as the average velocity in this region approached zero.

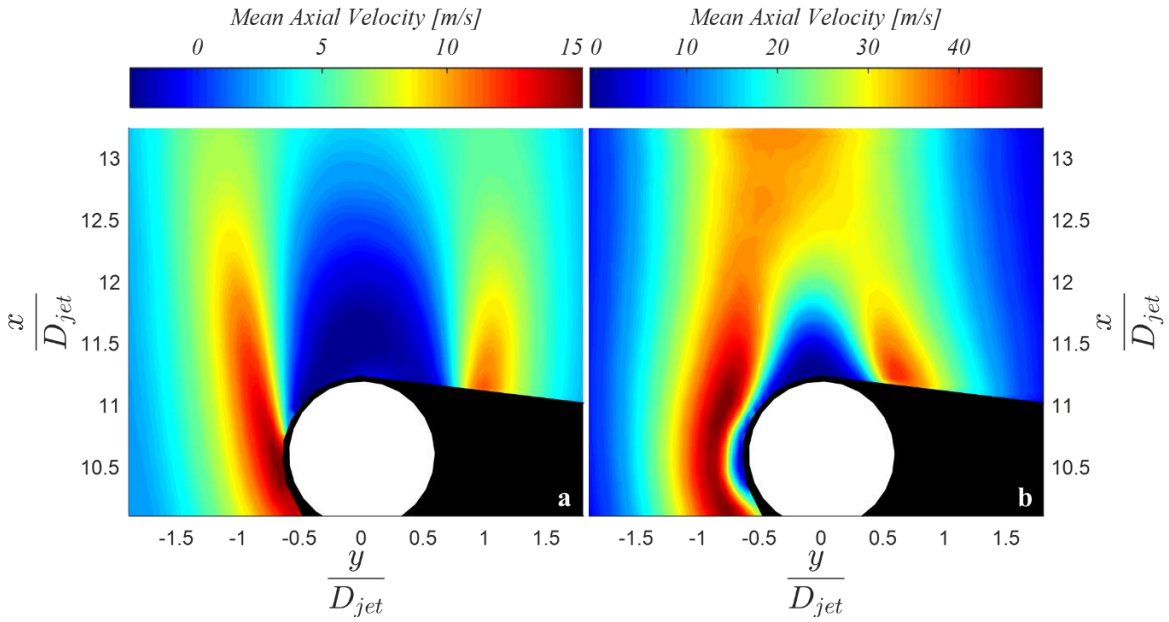

Figure 36. Mean axial velocity. (a) Re = 10,000 (b) Re = 50,000. Figure produced with multi-frame processing.

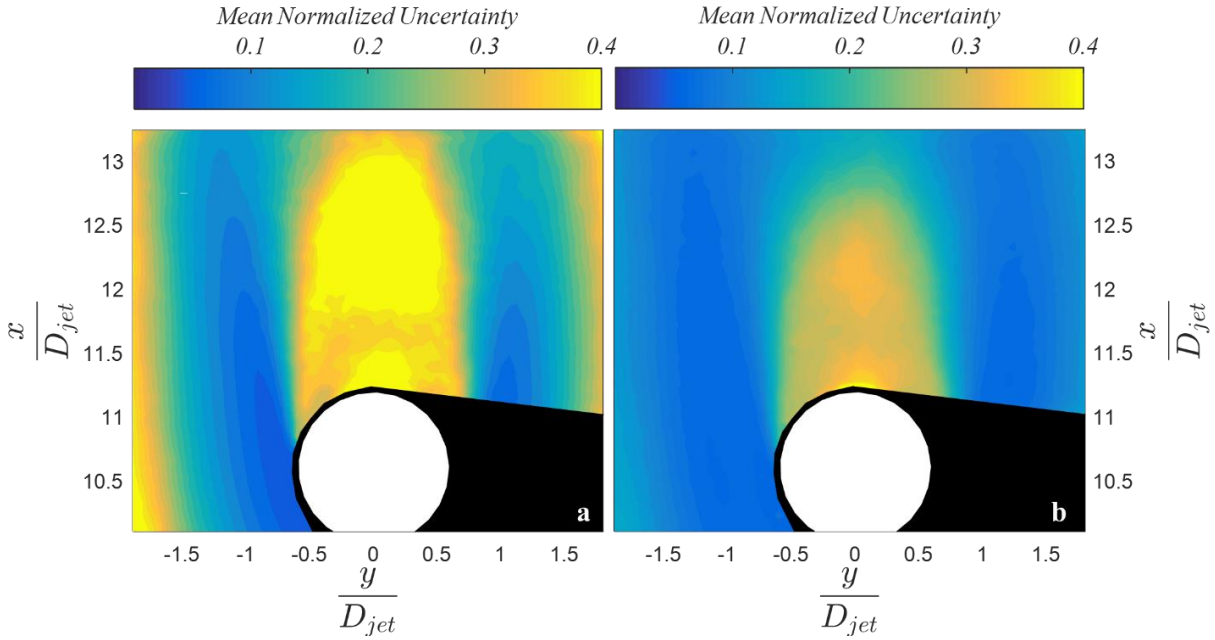

Figure 37. Mean normalized uncertainty for Re = 10,000, τ_{21} = 7.5 μs text case. (a) Standard processing (b) Multi-frame processing. Averaged uncertainty fields show same trend seen in instantaneous results.

As Reynolds number increased, time averaged uncertainty results for both standard and multi-frame processing improved over the whole field as a result of the increase in mean velocity. Figure 38 shows decreased mean uncertainty for both methods when compared to the Re = 10,000 test case. While standard processing did perform better for the Re = 50,000 test case, multi-frame was still far superior over the entirety of the flow field.

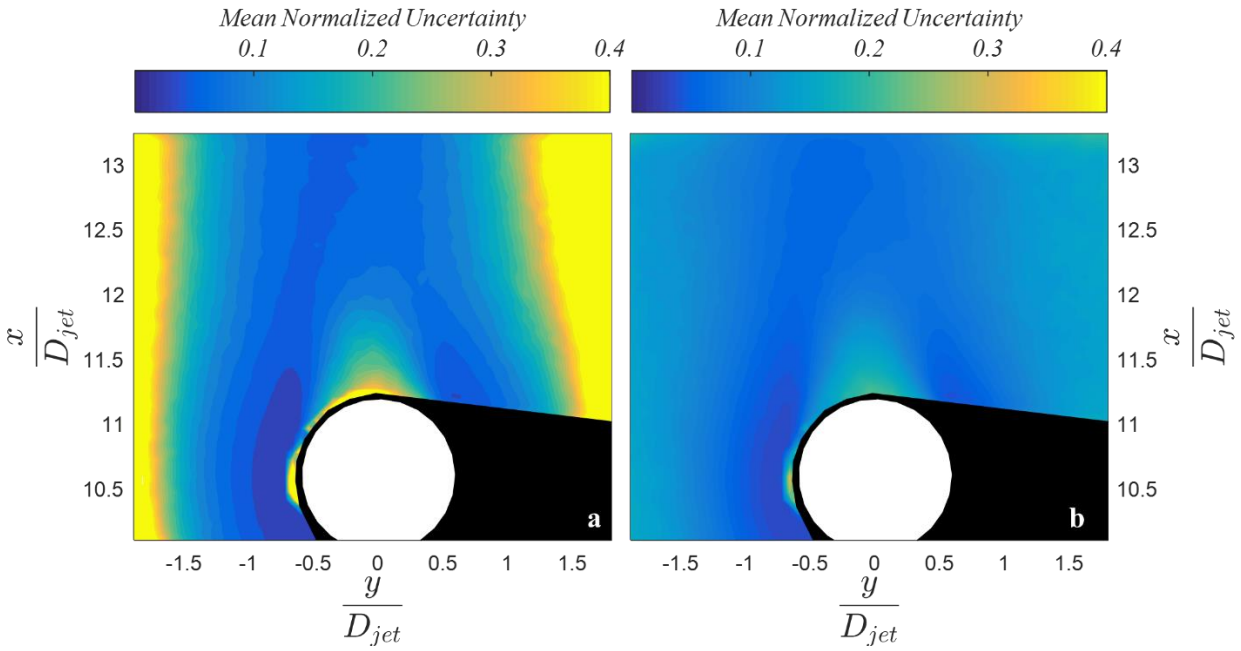

Figure 38. Mean normalized uncertainty for Re = 50,000, τ_{21} = 2.5 μs text case. (a) Standard processing (b) Multi-frame processing. Averaged uncertainty fields show same trend seen in instantaneous results.

Free jet test cases produced even lower uncertainty values, which followed the results of the instantaneous flow field results. Turbulence was fully developed for all three Reynolds numbers tested, however turbulent kinetic energy (TKE) levels were much higher for the bluff-body test cases (TKE results are shown in the following section). The increased turbulent fluctuations associated with vortex shedding from the cylinder subsequently resulted in increased

uncertainty in certain areas of the flow. Contrary to the bluff-body test cases, mean uncertainty in the free jet cases was uniformly distributed across the jet. Again, vast improvements were seen from multi-frame processing Figure 39 and Figure 40.

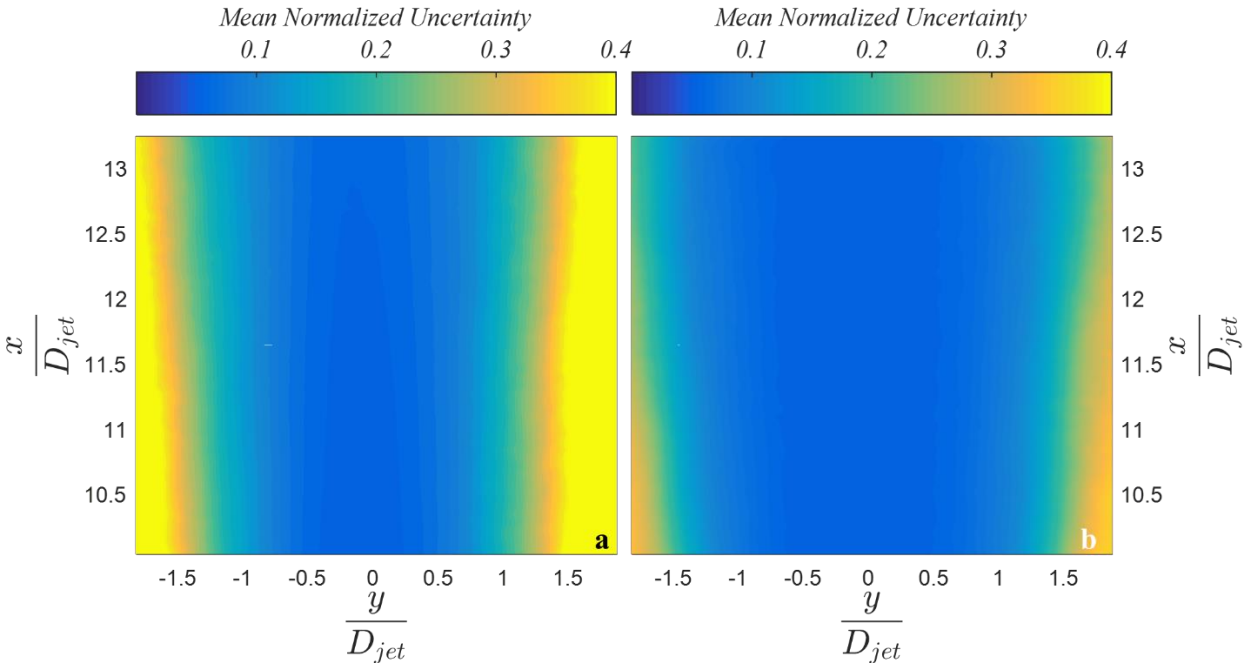

Figure 39. Time averaged uncertainty maps for the Re = 10,000, τ_{21} = 7.5 μs test case. (a) standard processing (b) multi-frame processing.

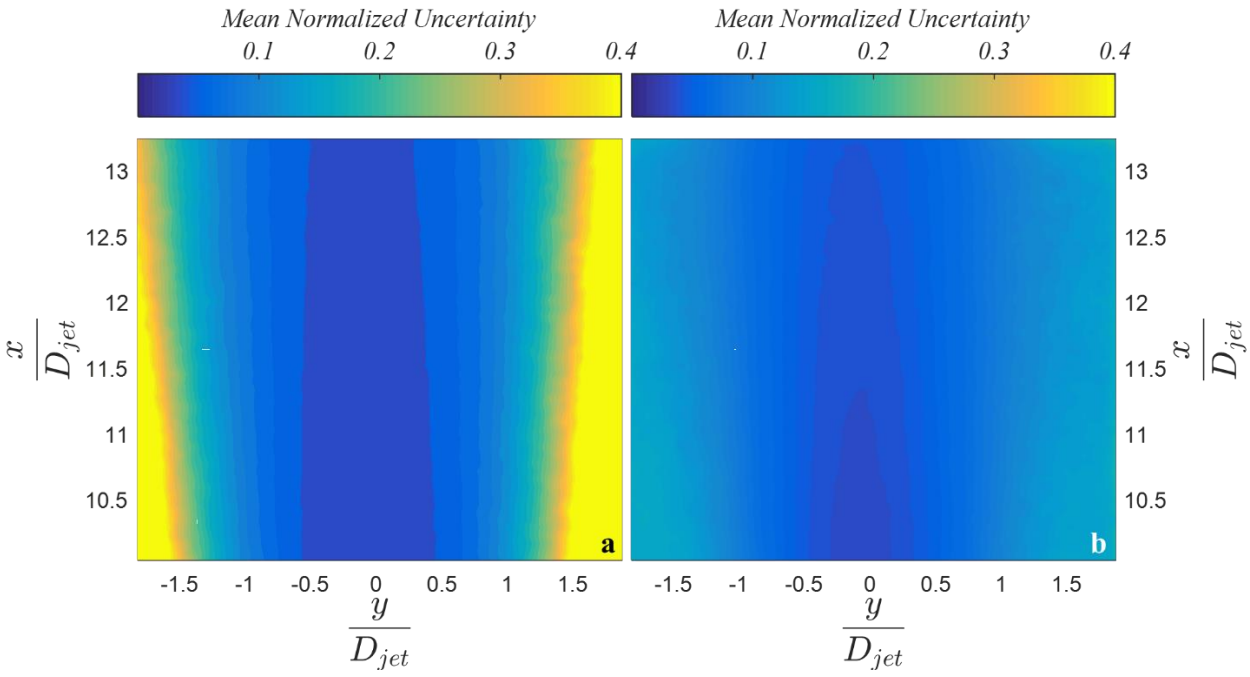

Figure 40. Time averaged uncertainty maps for the Re = 50,000, τ_{21} = 2.5 μs test case. (a) standard processing (b) multi-frame processing

Turbulent Kinetic Energy (TKE)

For time-averaged turbulence data, mean flow fields cannot provide any insight or measure of turbulence levels in the flow. However, velocity fluctuations about the mean can characterize turbulent intensities. Statistical turbulence models define the turbulent velocity to be a sum of the mean velocity and a fluctuation term.

$$u = \bar{u} + u' \tag{20}$$

For a given point in the flow, the RMS of the fluctuation term is equivalent to the turbulent kinetic energy (TKE).

$$TKE = \frac{1}{2}(\overline{u'u'} + \overline{v'v'}) \tag{21}$$

After the mean flow field was generated, the fluctuations at vector locations for all realizations were calculated. This data was then used to calculate the RMS fluctuations (TKE) at vector location, giving insight into the turbulence levels in the flow. All TKE maps have been normalized by the centerline jet velocity.

Mean flow field and TKE plots for the Re = 10,000 and Re = 50,000 bluff-body test cases are shown in Figure 41 and Figure 42 respectively. Both of the TKE maps show fairly symmetric high energy regions along the sides of the cylinder and propagating downstream. These regions correspond to the large scale structures produced by vortex shedding. Processing of the free jet shows the cylinder was not perfectly centered on the centerline of the jet, which produced consistently higher energies on the left side of the cylinder.

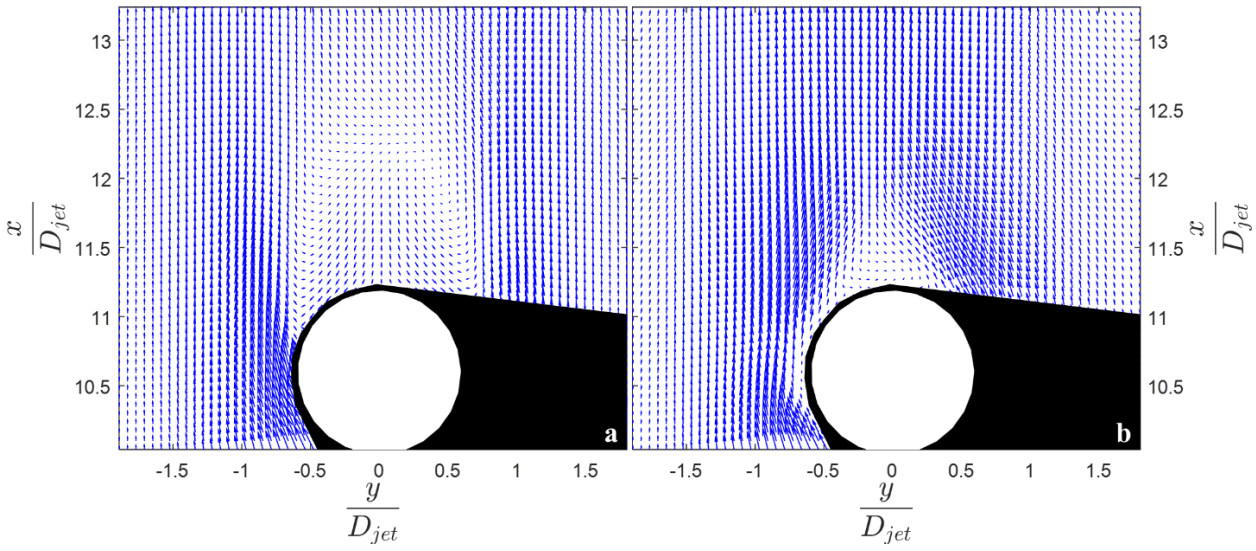

Figure 41. Mean vector fields found using multi-frame processing. (a) Re = 10,000 (b) Re = 50,000. The two vector fields are not scaled the same, so vector length is arbitrary. A mean negative axial velocity is seen in the recirculation zone behind the cylinder in (a) but is not seen in the higher Reynolds number case (b).

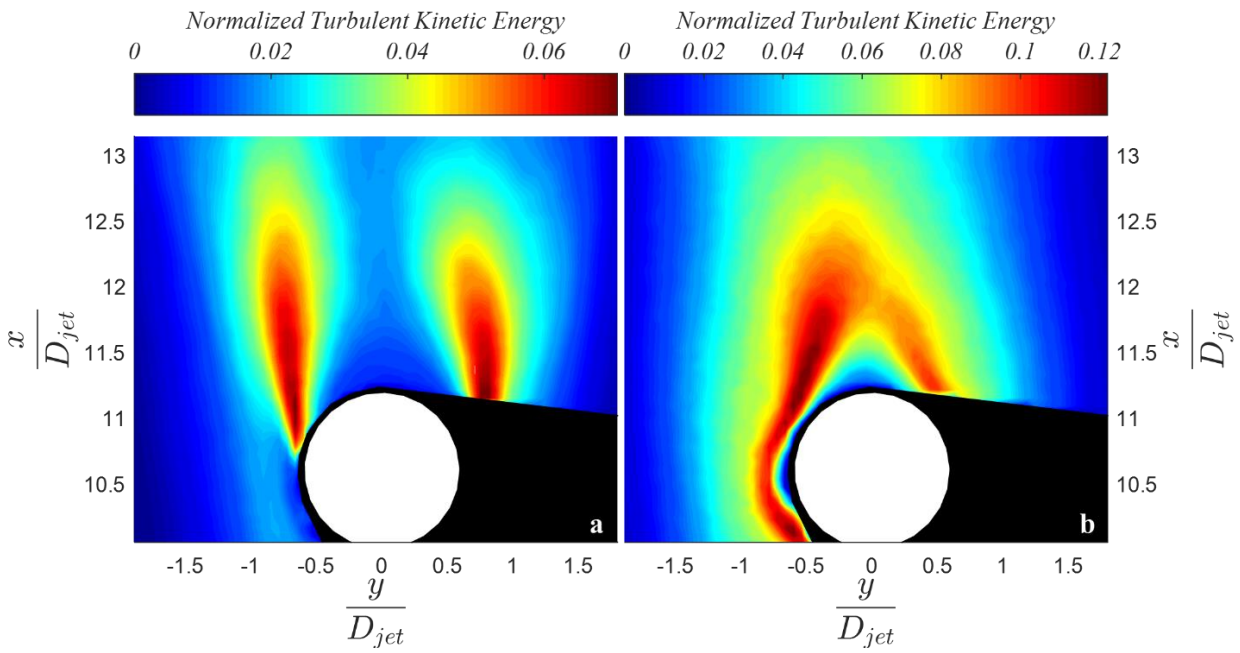

Figure 42. TKE maps (a) Re = 10,000 (b) Re = 50,000. Turbulent kinetic energy maps show areas of highest fluctuations occur in the area of vortex shedding around the sides of the cylinder.

5.2.4 Time-Resolved Velocity Fields

Pulse-burst laser systems allow for unmatched temporal resolution in PIV measurements. All test cases described in this work achieved a temporal resolution of 100 μs. This made it possible to study the time evolution of flow features using derived parameters such as vorticity, as well as modal analysis with techniques like Proper Orthogonal Decomposition (POD) and Dynamic Mode Decomposition (DMD).

Time resolved turbulent PIV data allows for identification and characterization of vortical structures. Vorticity is easily derived from two-dimensional vector data. Plots of vorticity and its evolution in time gives valuable insight on turbulent structures and their strengths. Figure 43 shows vorticity maps from the Re = 10,000 bluff-body test case at equal 100 μs time intervals.

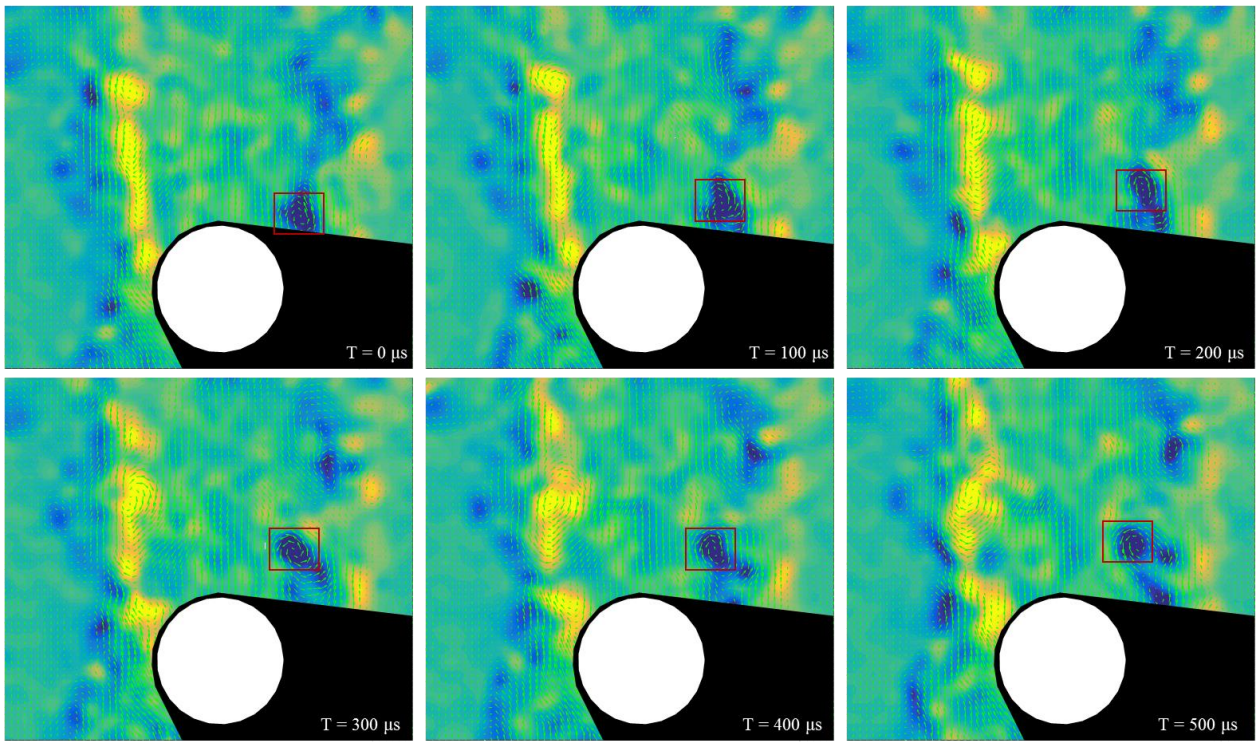

Figure 43. Vorticity map for the Re = 10,000 test case. Boxed area shows a vortical structure propagating downstream. The strongest areas of vorticity are seen to be vortex shedding from the cylinder.

Vortex shedding can be seen on both sides of the cylinder. These areas appear to produce the highest vorticity. However, it is apparent that the entire flow field contains high turbulence due to the presence of many small scale vortical structures throughout. To better visualize the dominant vorticity regions of the flow, a threshold was applied to isolate just the highest vorticity regions. Figure 44 shows more clearly that the shedding from the cylinder produces the strongest vorticity regions. It also appears the shedding is symmetric and potentially cyclical. For laminar flows, vortex shedding has a very distinct frequency given by the Strouhal number. In order to determine if the shedding seen in these vorticity maps is cyclical, modal decomposition methods were used.

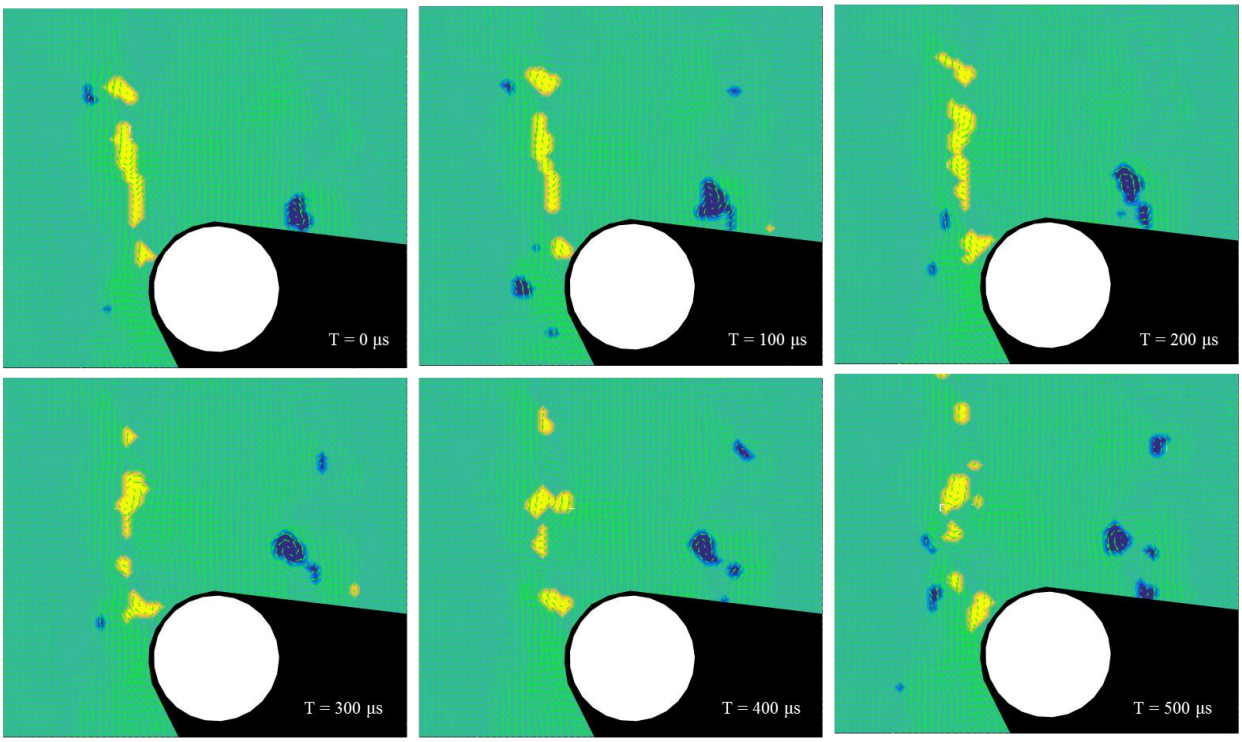

Figure 44. Vorticity map for the Re = 10,000 test case. Threshold value removes lower intensity structures. Here the high intensity structures are isolated. Again, highest vorticity is produced from vortex shedding from the cylinder.

For bluff-body test cases, visual inspection of the time resolved flow field and vorticity data revealed the presence of eddies possibly associated with vortex shedding from the cylinder. For laminar flow cases, vortex shedding frequencies have been well characterized for cylindrical bluff bodies. However, for fully developed turbulent flows, large and small scale eddies are present throughout the whole flow field, so the effects of vortex shedding become more difficult to observe visually. Because of this, the modal decomposition method POD was used. POD is a means for identifying coherent structures in turbulent flows and ranking them by their energy. # shows the first 12 modes for a Re = 10,000. The zeroth-order mode represents the mean flow field, and as a result this mode contains the majority of the energy. Modes one and two appear to

be large symmetric structures, which is possibly the result of Von-Karman vortex shedding. The rest of the modes show the presence of smaller structures throughout the wake region of the bluff-body

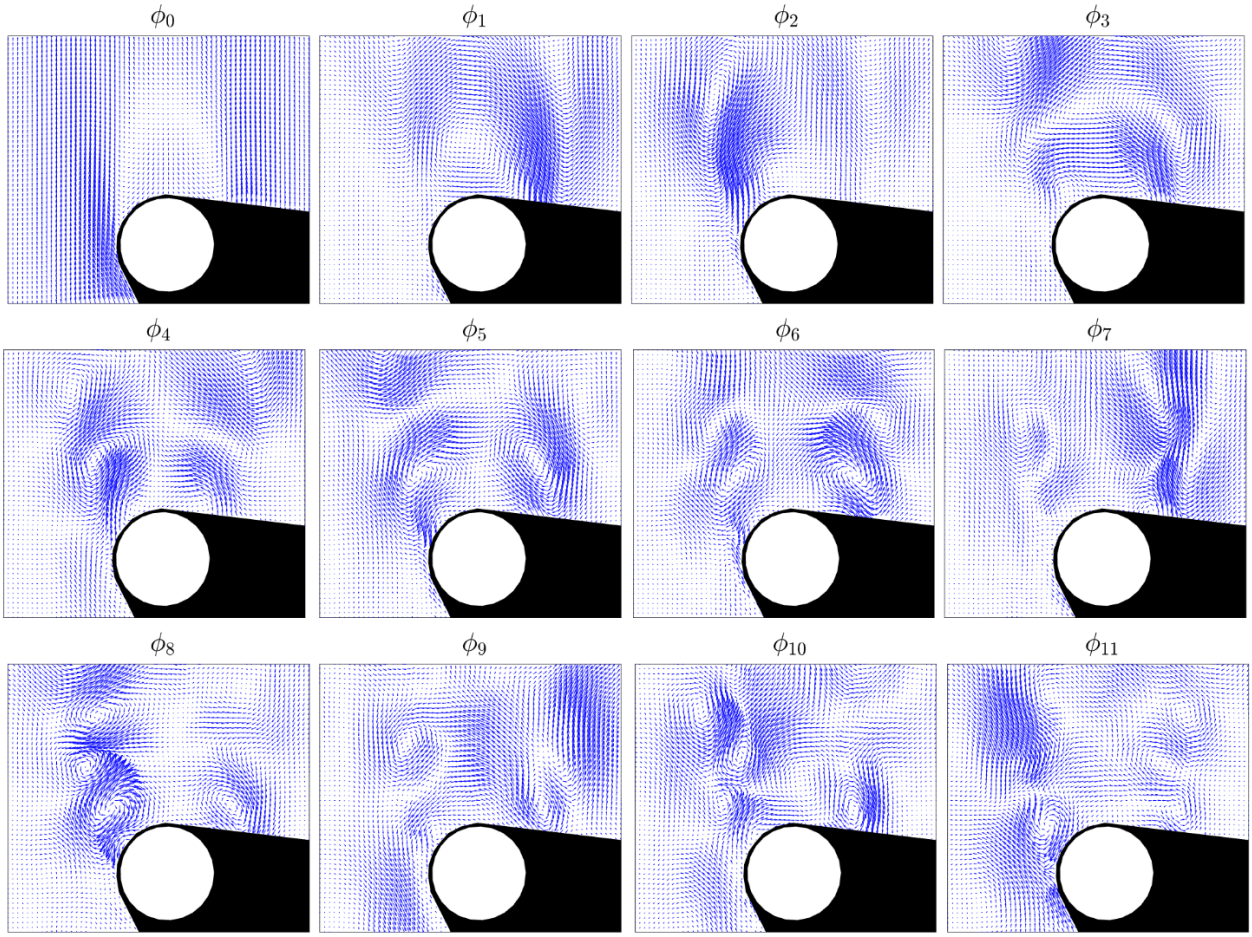

Figure 45. POD results of the Re = 10,000 bluff-body flow test case. Modes 0 – 11. Modes 1 and 2 show the two dominate modes appear to be symmetrical.

POD vector fields for the first 12 modes do not provide definitive conclusions of the presence of symmetrical, periodic Von-Karman vortex shedding. There is potential that modes one and two represent symmetrical structures, but more evidence is required. Looking at

vorticity maps of the same 12 modes reveals modes one and two do produce symmetric structures with almost equal energies.

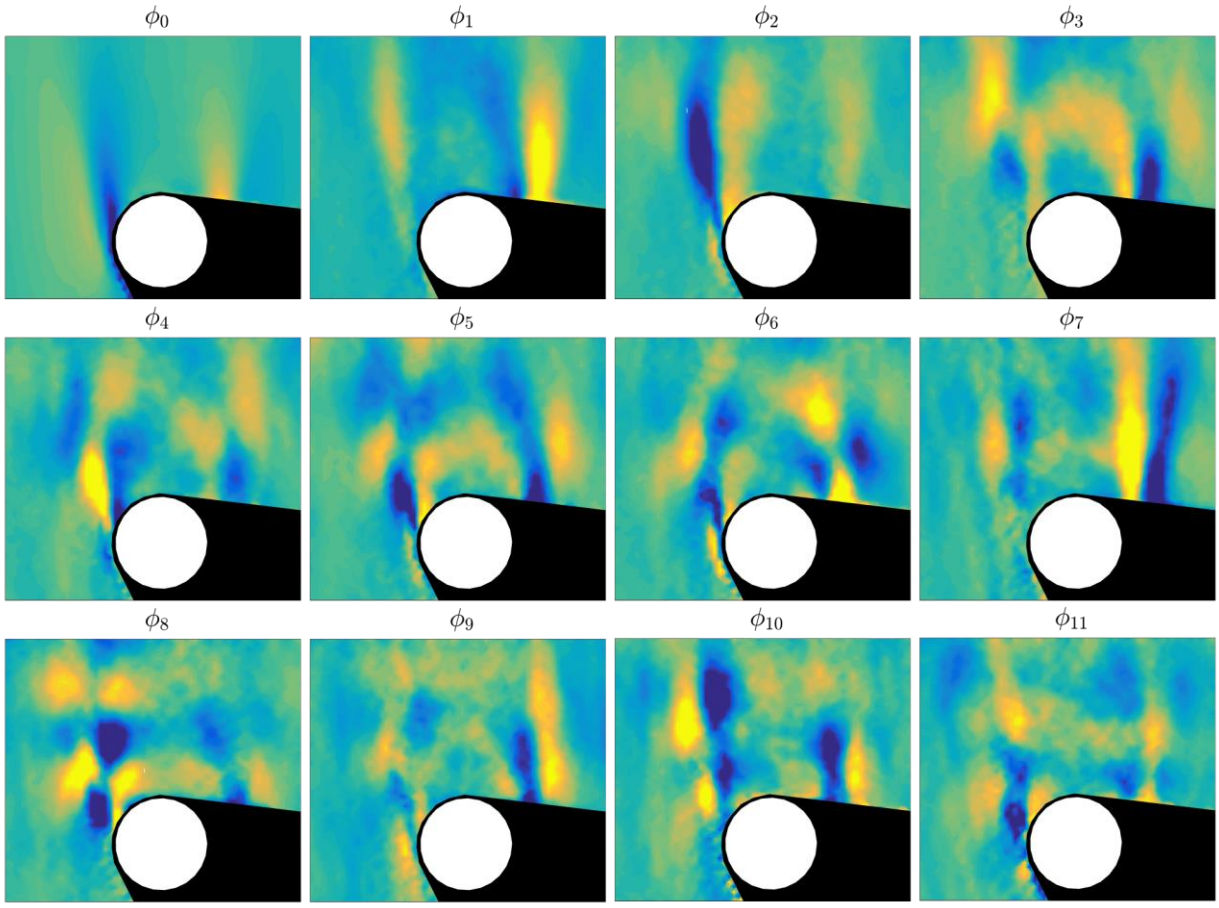

Figure 46. Vorticity of each mode for the Re = 10,000 bluff-body flow test case. Symmetrical structures are possibly noticed in modes 1-2 and modes 3-4, but it is not definitive from this analysis.

These results support the time-resolved vorticity results shown in Figure 43 and Figure 44. However, to provide evidence of cyclical vortices, a shedding frequency must be determined. POD results were used in an attempt to determine this frequency. Fourier transform of the POD times coefficients should have revealed the presence of a dominant frequency should one have existed (see Figure 47). However, the pulse-burst data was collected 45 snapshots at a time. A five second relaxation time between each burst from the laser separated each set of

realizations. This did not have an effect on the modal decomposition, but it did result in out-of-phase frequency data. This rendered POD ineffective at producing a shedding frequency.

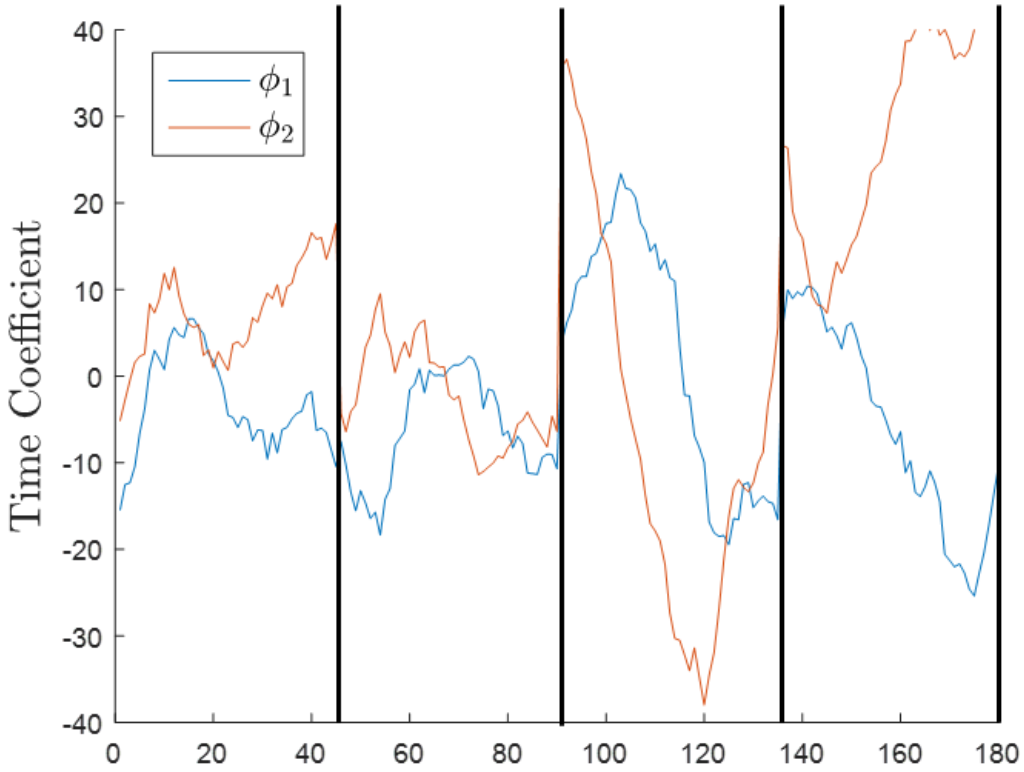

Figure 47. Time coefficient data plotted for each realization. Every 45 realizations, a discrete jump is seen which is due to the length of each laser burst. Frequency content might reveal cyclic nature of vortex shedding, but POD analysis requires a continuous time series. Because of this, frequency results were inconclusive.

5.3 System Optimization and Multi-Frame Limitations

Discussion on Pulse-Burst Optimization

The Re = 50,000 test cases approached the extreme with regards to flow DVR as well as the pulse-burst laser in conjunction with the SA-X2 high-speed camera. To study a turbulent jet at a Re = 50,000 along with the shear layer and entrainment of ambient, low-velocity air, a wide range of time spacings was required. Additionally, it was imperative there was at least one sufficiently short time spacing to ensure the highest velocity region of the flow was resolved. The pulse-burst was capable of much shorter pulse spacings, but in this case 2.5 μs was found to be optimal. In multi-frame processing of three time spacings, ideally the shortest and longest spacings sufficiently resolve the highest and lowest velocity regions respectively. The middle time spacing would then lie roughly half-way between the other two spacings. Again, the pulse burst-laser was capable of producing such a situation. However, in dealing with only three pulses, the first two pulses must come sufficiently close in time to resolve high speeds, and the time from the first to third pulse must allow enough time to resolve low speed. As a result, the time spacing from pulse two to three was quite large in this case. This meant the middle time spacing had a minimal contribution to the resulting vector field.

The incredible capability of the pulse-burst allowed for four pulses per burst to be produced, which would theoretically remedy this issue as well as produce another three potential time spacings for comparison. This would improve the accuracy of the technique. Unfortunately, limitations of the camera would not allow such a setup. For this particular test case, the desired camera resolution was on the order of 0.25 megapixels. Because of this, the camera frame rate was limited to 50 kHz. At this frame rate, the maximum exposure was slightly less than 20 μs. For this cross-correlation based processing scheme, particle images

must be singly exposed. As a result, even using frame straddling, this 20 μs exposure will set the minimum time between the first and third pulses of a burst. In order to accommodate quadruple pulsing while maintaining the time spacing from the first to last pulses, the camera would need to be run at least twice as fast. The SA-X2 was capable of running at 100 kHz, however the resolution would have been roughly one-quarter of the resolution at 50 kHz. This small of an area would not allow studying the desired flow field.

Discussion on Multi-Frame Optimization and Limitations

Optimization of multi-frame PIV processing was done using both qualitative and quantitative data. A trial and error process was initially employed to develop the algorithm to a point where it was producing adequate results. From there, post-processing was approached one step at a time to best optimize the system. Following the correlation of the three time spacings for a particular instance, the first step in post-processing was a fairly routine step with regard to common PIV practices, and did not require much for optimization.

The vector selection step required much more rigorous evaluation. The concept for vector selection was based on the work done by Charonko and Vlachos with regard to correlation-plane data analysis for PIV uncertainty quantification [42]. Their work states SNR of the correlation plane directly correlates to the uncertainty of that measurement. This idea was adapted for optimal selection of time spacing for each vector. The primary to secondary peak ratio from each vector correlation plane was found, and the vector with the best ratio was selected. This metric was not sufficient as the only step for vector selection, however. It was determined that correlation plane data for displacements less than one pixel often did not contain a secondary peak due to the small particle shifts. The algorithm would identify this as a large peak ratio, and subsequently created a bias toward the short times spacing τ_{21}. To combat this,

vectors containing particle displacements less than one pixel for τ_{21} were temporarily rejected. This was done out of necessity, but it also aided in promoting filling the vector field with longer time spacings, leading to decreased uncertainty.

Another issue arose in the situation of all three vectors containing very small correlation peak ratios. In the case of three peak ratios indistinguishable from the noise, the best vector cannot be determined by this metric. This is why in the vector selection step, vectors with peak ratios less than 1.2 were temporarily rejected. A test was conducted on two uncorrelated images to determine the noise threshold. It was discovered that for uncorrelated images, the average peak ratio was 1.06 with a standard deviation of 0.03. This showed limit of 1.2 was just above the noise threshold, making a good limit for temporary vector rejection.

The final limitation used in vector selection was a maximum limitation of 1.6. It was found the vectors with peak ratios above this point produced very low uncertainty, regardless of time spacing. Thus, to minimize uncertainty it was desirable to select a vector with a longer time spacing if multiple vectors had peak ratios greater than 1.6.

The next step in the post-processing algorithm was a vector fill method based on a median filter. The median for a 3 x 3 kernel centered on a particular vector location was found, excluding the center of the kernel. Then values for that vector location from all three time spacings were compared to the median and the optimal vector was selected. This step was fairly straight forward and did not require much adjustment.

The final step in post-processing was a vector rejection based on median filtering. The median filter described in the work by Westerweel and Scarano was used [37]. This filtering

process was described in detail in chapter 4.3. Threshold values were varied between four and six based on visual inspection of the resulting vector field.

While this method of PIV processing did show improvements over standard processing, several limitations need to be addressed. First, for a large amount of vectors with particle displacements larger than the maximum allowable 4 pixel displacement, the algorithm will tend to fill these areas with uncorrelated vectors from longer time spacings. These issues were not seen in the experimental data because the time spacings were optimized for the flow velocity. However, should a situation arise where the maximum velocity of the flow is not resolvable by the shortest time spacing, problems could arise. The maximum displacement limit will always reject vectors with too large of displacements, but the algorithm will try to fill these empty spaces with vectors from the other two time spacings which most certainly will be uncorrelated. If this high velocity region in the flow is relatively small, the median filter will catch these spurious vectors and reject them. But if the high velocity region is large, spurious vectors might make it through all post-processing steps. To combat this, one idea might be to move the rejection based on large velocity to after the median filter. This would hopefully result in improved correlation in these high velocity regions. If this worked, that would mean non-spurious vectors would be rejected by the maximum velocity filter, but the increased uncertainty that comes with such large displacements in high velocity flows would justify their rejection. Ideally, this problem would never be a real issue if the time spacings were properly optimized to resolve all high velocity structures of the flow.

Another potential issue with multi-frame processing results from the centers of each time spacing not lining up on one another. In two-frame PIV, the exact moment in time corresponding to a particular instance is often thought of as lying halfway in between the two

pulses. However, because only two frames are being correlated, this exact temporal location of each instance is unimportant. This is not the case in multi-frame processing. Vectors from three time spacings were combined to create a composite image, resulting in three different exact temporal locations for each of those vector sets. For this study, this effect was assumed to be negligible due to the short pulse spacings used, but it should be addressed. In a flow experiencing local accelerations, vectors from three separate time spacings might improperly represent the actual flow field. The idea of convecting results from each time spacing to a common, central time was considered. This was not implemented for this study, but it remains a question that must be answered in future work.

CHAPTER 6 CONCLUSIONS

Several conclusions can be drawn from the results of this study. First, it was shown through the use of synthetic data that processing multiple time spacings to form a composite vector field was a viable method to increase dynamic velocity range. Processing of synthetically generated particle images showed greatly improved resolution of low velocity regions with multi-frame compared to standard two-frame processing. It was also seen that error was greatly reduced in these low velocity regions. Because the maximum displacement was limited conservatively, error from velocity gradients and rotation was also minimized. A standard metric for estimating uncertainty was defined, and uncertainty maps of synthetically processed images showed the same trends as the error maps.

Experimental pulse-burst PIV data was collected for a fully-developed turbulent jet in both free jet and cylindrical bluff-body test cases. Pulse triplets with specific time spacings were generated to optimize coverage of all flow time-scales studied. Multi-frame processing revealed decreased instantaneous and time averaged uncertainty in all test cases when compared to standard PIV processing. These findings supported the synthetic results. Also, multi-frame processing produced DVR improvements ranging from 3.3-10 times that of standard PIV. Because of this, multi-frame processing covered the velocity range of all Reynolds numbers studied, where standard processing often failed to resolve low velocity regions.

Finally, time-resolved multi-frame PIV data was shown and analyzed in order to draw conclusions about the turbulent flows studied. Temporal resolution of 100 μs was achieved for all data, which allowed for the evolution of turbulent structures to be tracked. Especially with regard to the bluff body test cases, vorticity results revealed symmetrical vortex shedding, which was expected. Due to the fully developed turbulent nature of the flow, many smaller structures

were also seen. POD was used for identification and energy ranking of these structures, however the results were inconclusive. Evidence was seen that supported the existence of cyclical vortex shedding. However, because time series were not continuous, discontinuities were contained in the time coefficient data which prevented the extracting of a shedding frequency should one have existed. DMD was suggested as a method to attain a frequency for the energetic modes discovered using POD.

In summary, the results of this thesis show pulse-burst PIV has tremendous capabilities with regards to triple pulsing at high repetition rates. In order to best optimize these capabilities, multi-frame processing was used. Multi-frame processing of time-resolved PIV data shows consistent increase in DVR while simultaneously decreasing processing uncertainty.

WORKS CITED

1. R. J. Adrian, "Particle-Imaging Techniques for Experimental Fluid Mechanics," 261–304 (1991).
2. C. E. Willert and M. Gharib, "Digital particle image velocimetry," Exp. Fluids **10**, 181–193 (1991).
3. D. B. Barker and M. E. Fourney, "Measuring fluid velocities with speckle patterns.," Opt. Lett. **1**, 135–137 (1977).
4. "Time Resolved PIV System," http://www.tsi.com/Time-Resolved-PIV-System/.
5. L. W. Shakal and D. Troolin, "Accuracy, Resolution, and Repeatability of Powersight PDPA and LDV Systems," (2013).
6. "Laser Doppler Anemometry," http://www.dantecdynamics.com/laser-doppler-anemometry.
7. A. Krothapalli, "The development of laser speckle velocimetry for the study of vortical flows," NASA STI/Recon Tech. Rep. N **91**, 16289 (1991).
8. J. Westerweel, "Digital Particle Image Velocimetry - Theory and Application.pdf," 236 (1993).
9. I. Grant, "Particle image velocimetry: a review," Proc. Inst. Mech. Eng. Part C (Journal Mech. Eng. Sci. Publ Mech. Eng. Publ. IMechE **211**, 55–76 (1997).
10. M. Raffel, C. E. Willert, and J. Kompenhans, *Particle Image Velocimetry: A Practical Guide* (1998).
11. W. Merzkirch, "Particle image velocimetry," Opt. Meas. 341–357 (2001).
12. D. Dabiri, "Cross-Correlation Digital Particle Image Velocimetry-A Review," Turbulência, Ed., Freire, AS, Iiha, A., Breidenthal, B., … 1–54 (2006).
13. R. J. Adrian and J. Westerweel, *Particle Image Velocimetry* (2010).
14. "Imaging the Flow," http://www.vision-systems.com/articles/2010/10/imaging-the-flow.html.
15. a Melling, "Tracer particles and seeding for particle image velocimetry," Meas. Sci. Technol. **8**, 1406–1416 (1999).
16. D. L. Reuss, R. J. Adrian, C. C. Landreth, D. T. French, and T. D. Fansler, "Instantaneous planar measurements of velocity and large-scale vorticity and strain rate in an engine using particle-image velocimetry," SAE **SAE paper**, (1989).
17. L. Muniz, R. E. Martinez, and M. G. Mungal, "Applications of PIV to turbulent reacting flow," in *Proc. 8th Int. Symp. on Applications of Laser Techniques to Fluid Mechanics, Lisbon* (1996), p. paper 3.3.
18. R. Hocker and J. Kompenhans, "Application of particle image velocimetry to transonic

flow," in *Applications of Laser Techniques to Fluid Mechanics (Proc. 5th Int. Symp., Lisbon* (1990), pp. 415–34.

19. J. W. Cooley and J. W. Tukey, "J.W Cooley, J.W. Tukey - An Algorithm for the Machine Calculation of Complex Fourier Series.pdf," Math. Comput. **19**, 297–301 (1965).

20. J. Westerweel, "Fundamentals of digital particle image velocimetry," Meas. Sci. Technol. **8**, 1379–1392 (1997).

21. F. Scarano, "Iterative image deformation methods in PIV," Meas. Sci. Technol. **13**, R1–R19 (2002).

22. H. Nobach, N. Damaschke, and C. Tropea, "High-precision sub-pixel interpolation in particle image velocimetry image processing," Exp. Fluids **39**, 299–304 (2005).

23. M. R. Brady, "Subpixel Resolution Schemes for Multiphase Flows by Subpixel Resolution Schemes for Multiphase Flows," 35 (2006).

24. H. Nobach and E. Bodenschatz, "Limitations of accuracy in PIV due to individual variations of particle image intensities," Exp. Fluids **47**, 27–38 (2009).

25. R. J. Adrian, "Dynamic ranges of velocity and spatial resolution of particle image velocimetry," Meas. Sci. Technol. **8**, 1393–1398 (1999).

26. R. J. Adrian, "Image shifting technique to resolve directional ambiguity in double-pulsed velocity.," Appl. Opt. **25**, 3855–3858 (1986).

27. J. Westerweel, D. Dabiri, and M. Gharib, "The effect of a discrete window offset on the accuracy of cross-correlation analysis of digital PIV recordings," Exp. Fluids **23**, 20–28 (1997).

28. F. Scarano and M. L. Riethmuller, "Iterative multigrid approach in PIV image processing with discrete window offset," Exp. Fluids **26**, 513–523 (1999).

29. F. Scarano and M. L. Riethmuller, "Advances in iterative multigrid PIV image processing," Exp. Fluids **29**, S051–S060 (2000).

30. A. M. Fincham and G. R. Spedding, "Low cost, high resolution DPIV for measurement of turbulent fluid flow," Exp. Fluids **23**, 449–462 (1997).

31. A. Sciacchitano, B. Wieneke, and F. Scarano, "PIV uncertainty quantification by image matching," Meas. Sci. Technol. Meas. Sci. Technol **24**, 45302–45302 (2013).

32. D. J. Forliti, P. J. Strykowski, and K. Debatin, "Bias and precision errors of digital particle image velocimetry," Exp. Fluids **28**, 436–447 (2000).

33. L. Gui and S. T. Wereley, "A correlation-based continuous window-shift technique to reduce the peak-locking effect in digital PIV image evaluation," Exp. Fluids **32**, 506–517 (2002).

34. J. Nogueira, a Lecuona, and P. a Rodríguez, "Data validation, false vectors correction and derived magnitudes calculation on PIV data," Meas. Sci. Technol. **8**, 1493–1501 (1999).

35. W. Thielicke and E. J. Stamhuis, "PIVlab – Towards User-friendly, Affordable and

Accurate Digital Particle Image Velocimetry in MATLAB," J. Open Res. Softw. **2**, e30 (2014).

36. J. Westerweel, "Efficient detection of spurious vectors in particle image velocimetry data," Exp. Fluids **16**, 236–247 (1994).

37. J. Westerweel and F. Scarano, "Universal outlier detection for PIV data," Exp. Fluids **39**, 1096–1100 (2005).

38. B. H. Timmins, B. W. Wilson, B. L. Smith, and P. P. Vlachos, "A method for automatic estimation of instantaneous local uncertainty in particle image velocimetry measurements," Exp. Fluids **53**, 1133–1147 (2012).

39. R. D. Keane and R. J. Adrian, "Optimization of particle image ve I oci m e te rs . Part I : Double pulsed systems," Meas. Sci. Technol. **1**, 1202–1215 (1990).

40. R. D. Keane and R. J. Adrian, "Theory of cross-correlation analysis of PIV images," Appl. Sci. Res. **49**, 191–215 (1992).

41. J. Westerweel, "Theoretical analysis of the measurement precision in particle image velocimetry," Exp. Fluids **29**, S003–S012 (2000).

42. J. J. Charonko and P. P. Vlachos, "Estimation of uncertainty bounds for individual particle image velocimetry measurements from cross-correlation peak ratio," Meas. Sci. Technol. **24**, 065301 (2013).

43. Z. Xue, J. J. Charonko, and P. P. Vlachos, "Particle image velocimetry correlation signal-to-noise ratio metrics and measurement uncertainty quantification," Meas. Sci. Technol. **25**, 115301 (2014).

44. A. Sciacchitano, D. R. Neal, B. L. Smith, S. O. Warner, P. P. Vlachos, B. Wieneke, and F. Scarano, "Collaborative framework for PIV uncertainty quantification: comparative assessment of methods," Meas. Sci. Technol. **26**, 074004 (2015).

45. "Fastcam SA Series," (2016).

46. C. J. Kähler, S. Scharnowski, and C. Cierpka, "On the resolution limit of digital particle image velocimetry," Exp. Fluids **52**, 1629–1639 (2012).

47. R. J. Adrian, "Twenty years of particle image velocimetry," Exp. Fluids **39**, 159–169 (2005).

48. R. D. Keane and R. J. Adrian, "Theory of cross-correlation analysis of PIV images," Appl. Sci. Res. **49**, 191–215 (1992).

49. C. J. Kähler and J. Kompenhans, "Fundamentals of multiple plane stereo particle image velocimetry," Exp. Fluids **29**, S070–S077 (2000).

50. H. Hu, "Stereo Particle Imaging Velocimetry Techniques: Technical Basis, System Setup, and Application," Handb. 3D Mach. Vis. Opt. Metrol. Imaging 71–100 (2013).

51. G. E. Elsinga, F. Scarano, B. Wieneke, and B. W. Van Oudheusden, "Tomographic particle image velocimetry," Exp. Fluids **41**, 933–947 (2006).

52. R. Hain and C. J. Kähler, "Fundamentals of multiframe particle image velocimetry (PIV)," Exp. Fluids **42**, 575–587 (2007).

53. F. Pereira, A. Ciarravano, G. P. Romano, and F. Di Felice, "Adaptive Multi-Frame PIV," 1–12 (n.d.).

54. S. J. Beresh, S. P. Kearney, J. L. Wagner, D. R. Guildenbecher, J. F. Henfling, R. W. Spillers, B. O. M. Pruett, N. Jiang, M. N. Slipchenko, J. Mance, and S. Roy, "Pulse-Burst PIV in a High-Speed Wind Tunnel," Meas. Sci. Technol. **26**, 13 (2015).

55. B. Thurow, N. Jiang, M. Samimy, and W. Lempert, "Narrow-linewidth megahertz-rate pulse-burst laser for high-speed flow diagnostics.," Appl. Opt. **43**, 5064–5073 (2004).

56. J. B. Michael, H. Subramani, and T. R. Meyer, "Organized by the Western States Section of the Combustion Institute and hosted by the University of Utah High speed imaging and analysis of turbulent flames," (2013).

57. B. Thurow, N. Jiang, and W. Lempert, "Review of ultra-high repetition rate laser diagnostics for fluid dynamic measurements," Meas. Sci. Technol. **24**, 012002 (2013).

58. M. P. Wernet, "Temporally resolved PIV for space-time correlations in both cold and hot jet flows," Meas. Sci. Technol. **18**, 1387–1403 (2007).

59. J. D. Miller, J. B. Michael, M. N. Slipchenko, S. Roy, T. R. Meyer, and J. R. Gord, "Simultaneous high-speed planar imaging of mixture fraction and velocity using a burst-mode laser," Appl. Phys. B Lasers Opt. **113**, 93–97 (2013).

60. D. Litwiller, "CCD vs. CMOS," Photonics Spectra **35**, 154–158 (2001).

61. S. Pfadler, F. Dinkelacker, F. Beyrau, and A. Leipertz, "High resolution dual-plane stereo-PIV for validation of subgrid scale models in large-eddy simulations of turbulent premixed flames," Combust. Flame **156**, 1552–1564 (2009).

62. G. Usera, A. Vernet, and J. A. Ferré, "Time Resolved PIV Measurements for Validating LES of the Turbulent Flow Within a PCB Enclosure Model," Eng. Turbul. Model. Exp. 6 411–420 (2005).

63. R. J. Adrian, K. T. Christensen, and Z.-C. Liu, "Analysis and interpretation of instantaneous turbulent velocity fields," Exp. Fluids **29**, 275–290 (2000).

64. A. Agrawal and A. Prasad, "Properties of vortices in the self-similar turbulent jet," Exp. Fluids **33**, 565–577 (2002).

65. O. Semeraro, G. Bellani, and F. Lundell, "Analysis of time-resolved PIV measurements of a confined turbulent jet using POD and Koopman modes," Exp. Fluids **53**, 1203–1220 (2012).

66. S. B. Pope, *Turbulent Flows* (2000).

67. H. J. Hussein, S. P. Capp, and W. K. George, "Velocity measurements in a high-Reynolds-number, momentum-conserving, axisymmetric, turbulent jet," J. Fluid Mech. **258**, 31–75 (1994).

68. E. J. List, "Turbulent Jets and Plumes," Annu. Rev. Fluid Mech. **14**, 189–212 (1982).

69. G. L. Brown and A. Roshko, "On density effects and large structure in turbulent mixing layers," J. Fluid Mech. **64**, 775–816 (1974).

70. S. C. Morris, "Shear-Layer Instabilities: Particle Image Velocimetry Measurements and Implications for Acoustics," Annu. Rev. Fluid Mech. **43**, 529–550 (2011).

71. A. Schröder, R. Geisler, K. Staack, G. E. Elsinga, F. Scarano, B. Wieneke, A. Henning, C. Poelma, and J. Westerweel, "Eulerian and Lagrangian views of a turbulent boundary layer flow using time-resolved tomographic PIV," Exp. Fluids **50**, 1071–1091 (2011).

72. W. J. a. Dahm and P. E. Dimotakis, "Measurements of entrainment and mixing in turbulent jets," AIAA J. **25**, 1216–1223 (1987).

73. W. J. a. Dahm and P. E. Dimotakis, "Mixing at large Schmidt number in the self-similar far field of turbulent jets," J. Fluid Mech. **217**, 299 (1990).

74. A. R. Masri, B. B. Dally, M. Engineering, R. S. Barlow, S. N. Laboratories, and C. D. Carter, "The Structure of the Recirculation Zone of a Bluff-Body Combustor," in *Twenty-Fifth Symposium on Combustion/The Combustion Institute* (1994), Vol. m, pp. 1301–1308.

75. H. Chen, D. L. Reuss, D. L. Hung, and V. Sick, "A practical guide for using proper orthogonal decomposition in engine research," Int. J. Engine Res. **14**, 307–319 (2013).

76. P. J. Schmid, L. Li, M. P. Juniper, and O. Pust, "Applications of the dynamic mode decomposition," Theor. Comput. Fluid Dyn. **25**, 249–259 (2011).

77. Coats, "Dynamic mode decomposition of numerical and experimental data," Combust. Flame **157**, 1–6 (2007).

78. B. Wieneke, "Generic a-posteriori uncertainty quantification for PIV vector fields by correlation statistics," 17th Int. Symp. Appl. Laster Tech. to Fluid Mech. 1–9 (2014).

APPENDIX A INSTANTANEOUS FLOW FIELD RESULTS

A.1 Re = 30,000, Magnification = 0.326, Bluff-Body Flow

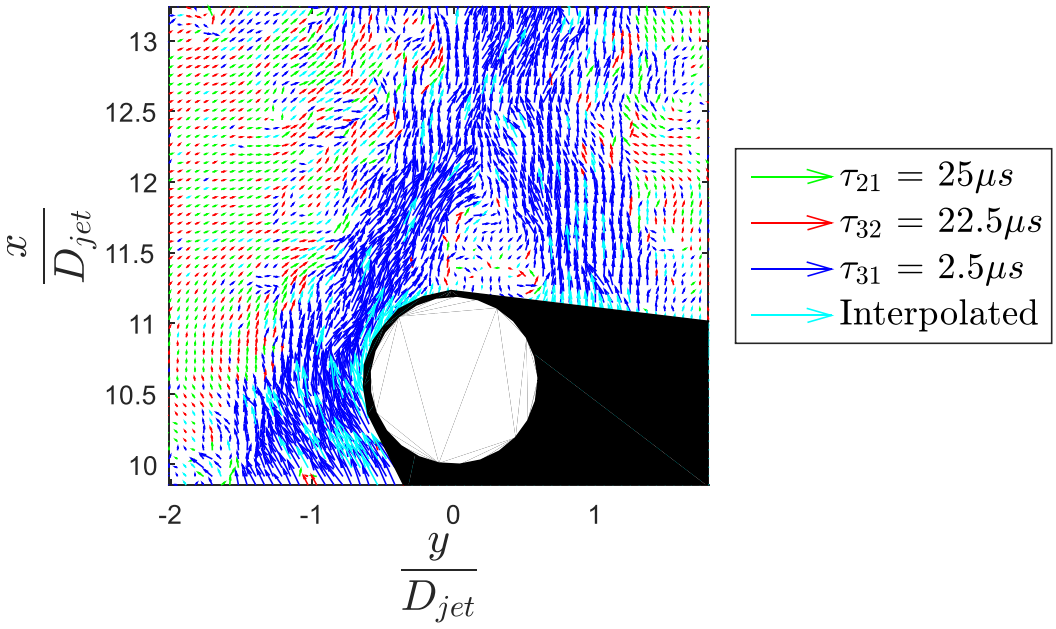

Figure 48. Composite vector field for the Re = 30,000, τ_{21} = 2.5 μs test case.

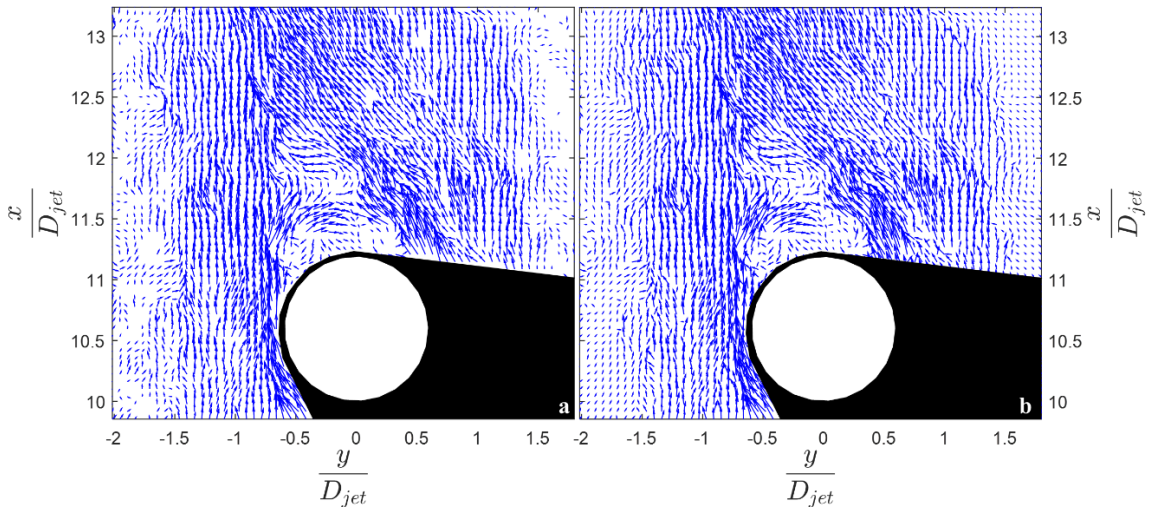

Figure 49. Instantaneous vector field for the Re = 30,000, τ_{21} = 2.5 μs test case. (a) standard (b) multi-frame.

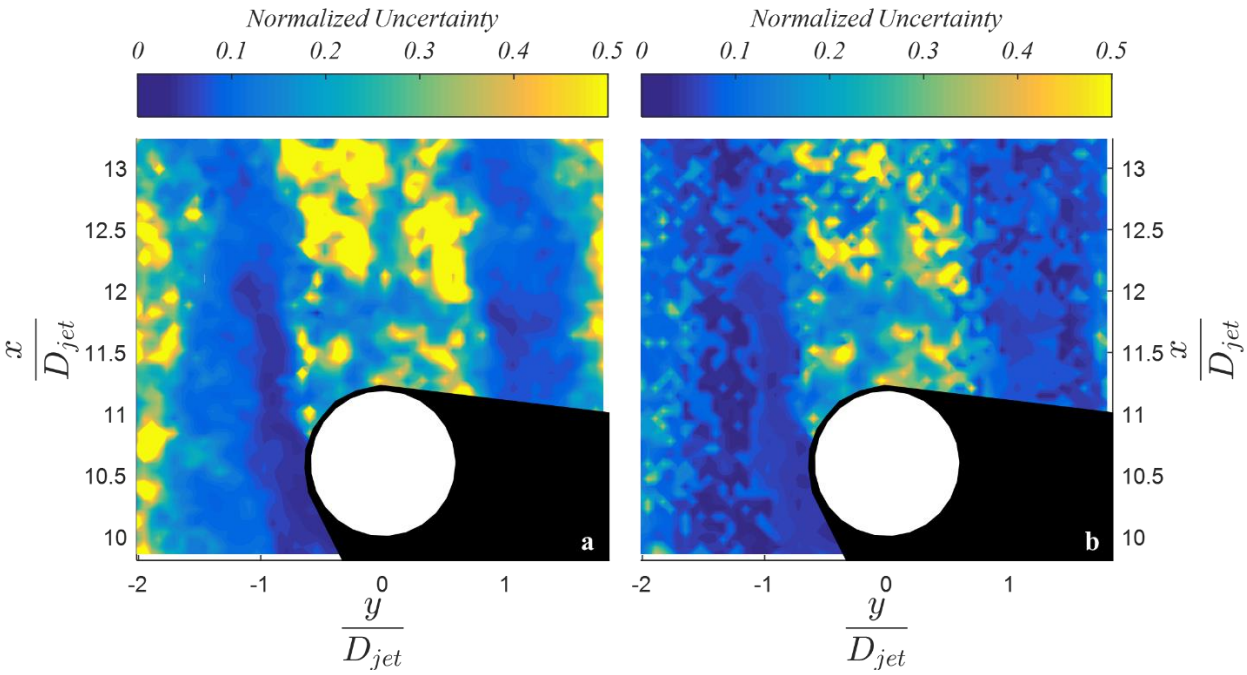

Figure 50. Instantaneous uncertainty map for the Re = 30,000, τ_{21} = 2.5 μs test case. (a) standard (b) multi-frame.

A.2 Re = 30,000, Magnification = 0.326, Jet Only Flow

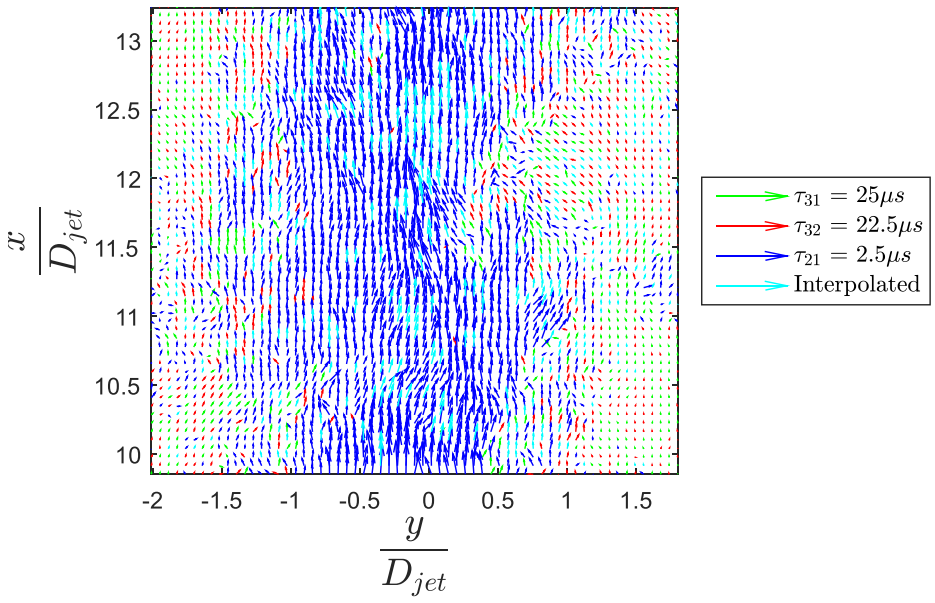

Figure 51. Instantaneous composite vector field the Re = 30,000, τ_{21} = 2.5 μs free jet test case. (a) standard (b) multi-frame.

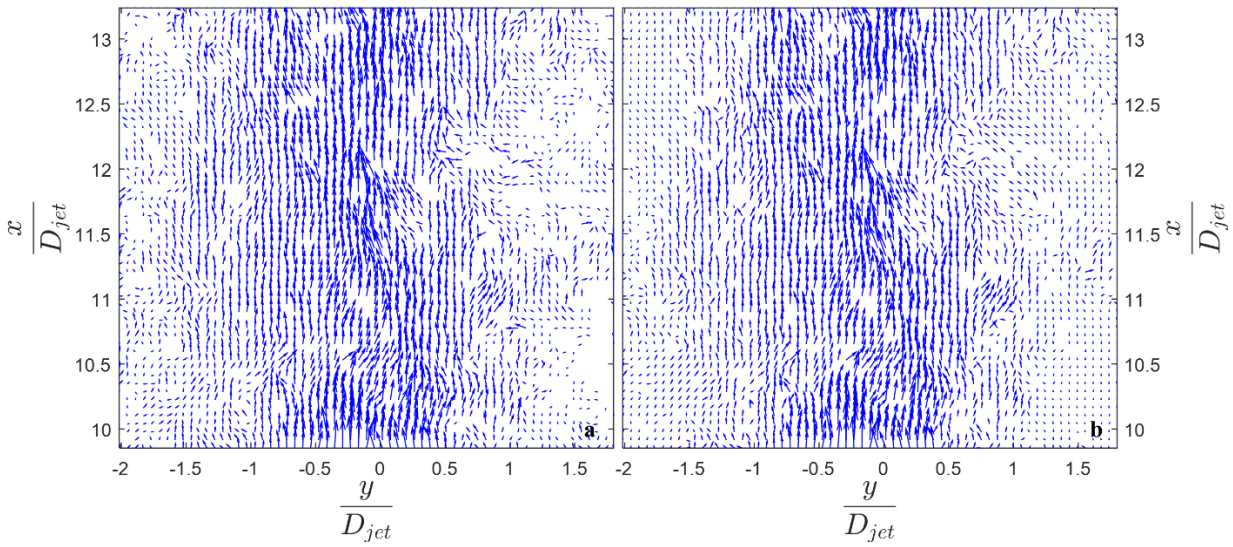

Figure 52. Vector fields for the Re = 30,000, τ_{21} = 2.5 μs free jet test case. (a) standard (b) multi-frame.

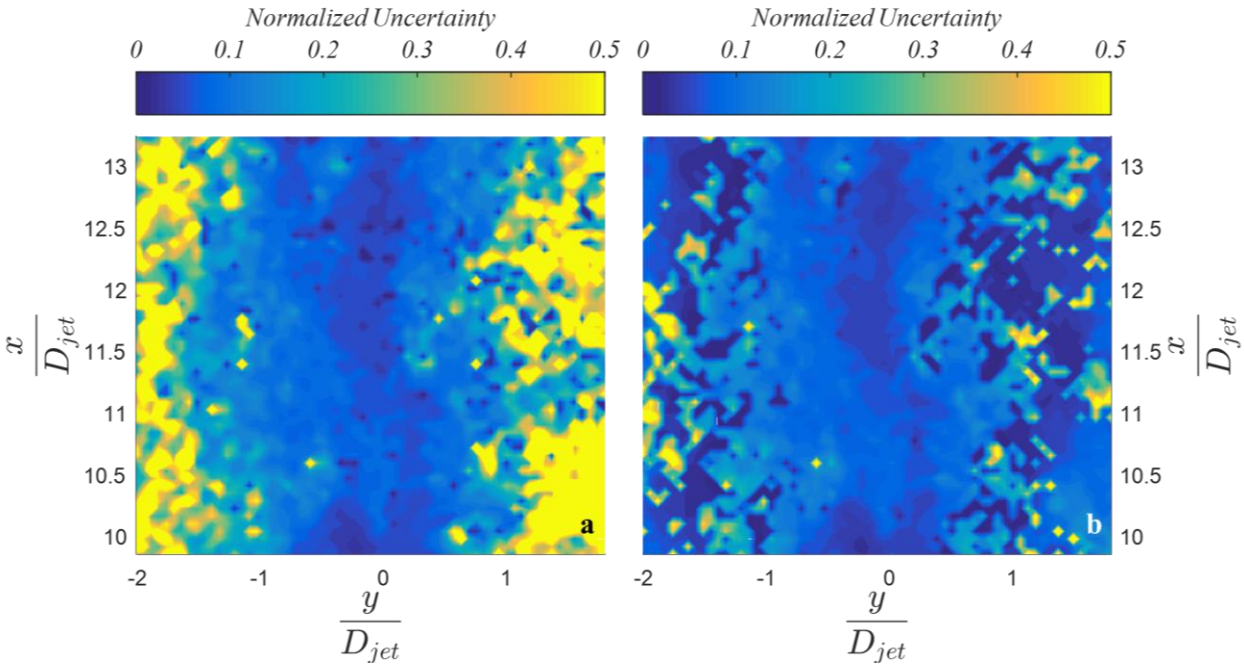

Figure 53. Instantaneous uncertainty map for the Re = 30,000, τ_{21} = 2.5 μs free jet test case. (a) standard (b) multi-frame.

A.3 Re = 10,000, Magnification = 0.206, Bluff-Body Flow

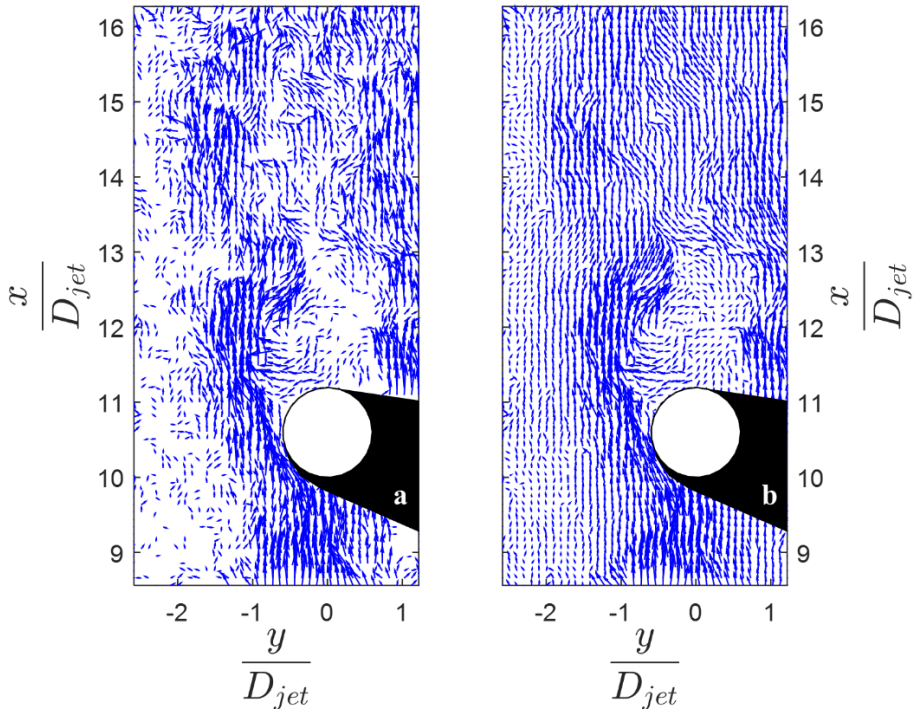

Figure 54. Vector fields for the Re = 10,000, τ_{21} = 7.5 test case. (a) standard (b) multi-frame.

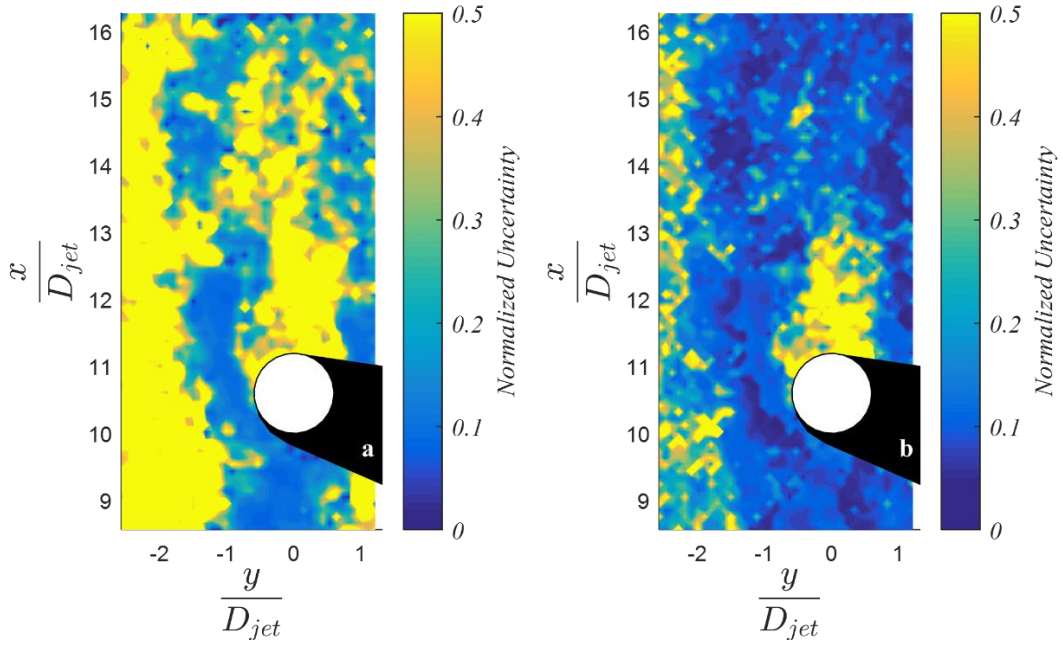

Figure 55. Instantaneous uncertainty maps for the Re = 10,000, τ_{21} = 7.5 test case. (a) standard (b) multi-frame.

A.4 Re = 30,000, Magnification = 0.206, Bluff-Body Flow

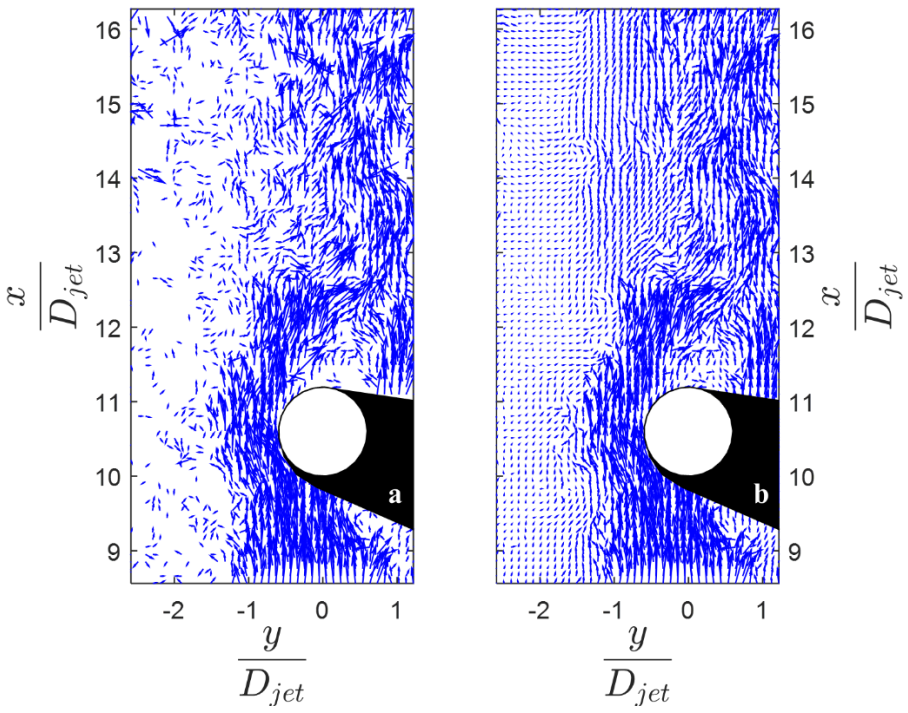

Figure 56. Vector fields for the Re = 30,000, τ_{21} = 2.5 test case. (a) standard (b) multi-frame.

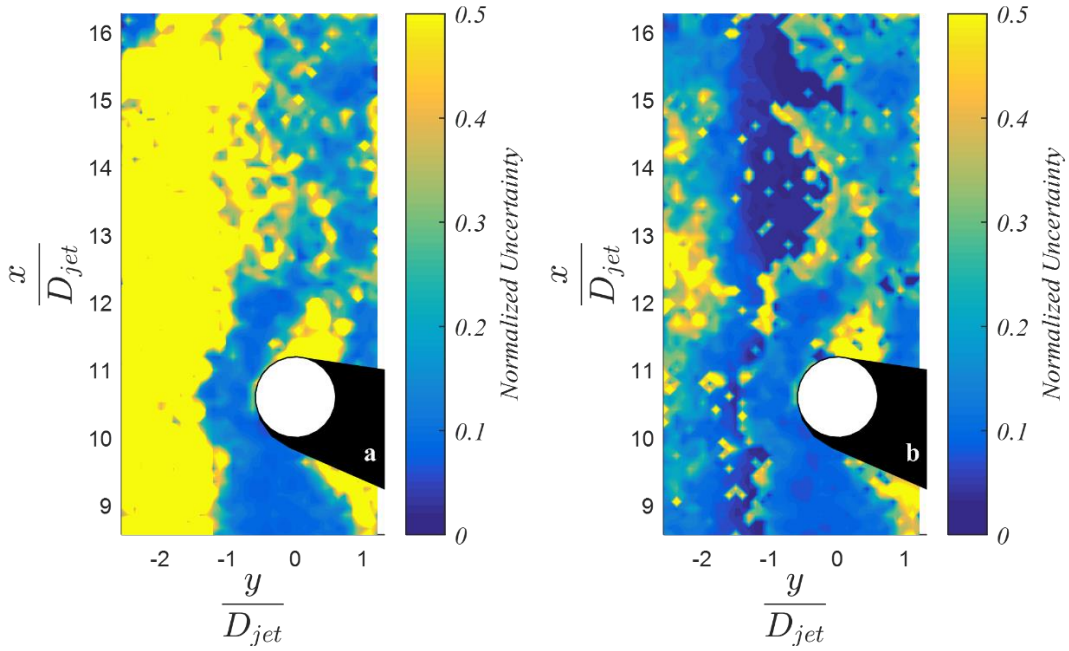

Figure 57. Instantaneous uncertainty maps for the Re = 30,000, τ_{21} = 2.5 test case. (a) standard (b) multi-frame.

A.5 Re = 50,000, Magnification = 0.206, Bluff-Body Flow

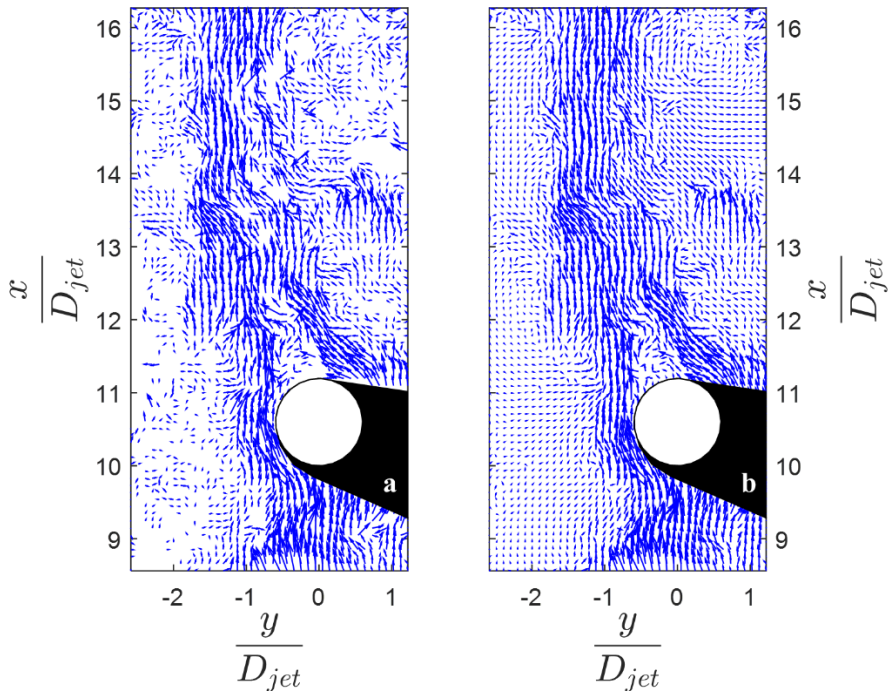

Figure 58. Vector fields for the Re = 50,000, τ_{21} = 2.5 test case. (a) standard (b) multi-frame.

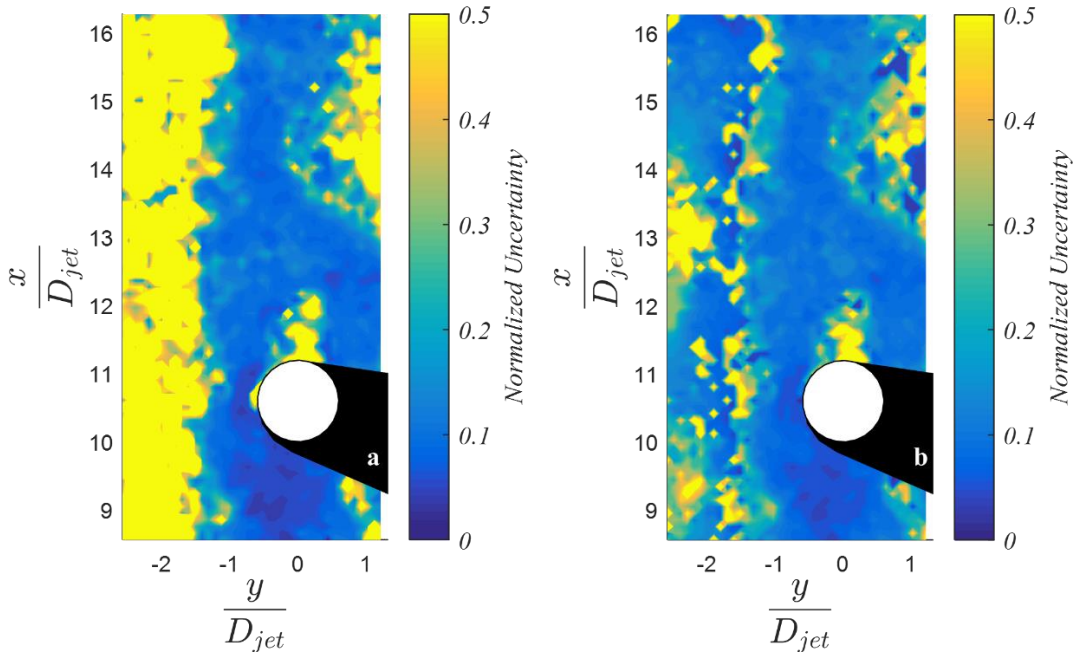

Figure 59. Instantaneous uncertainty maps for the Re = 50,000, τ_{21} = 2.5 test case. (a) standard (b) multi-frame.

A.6 Re = 10,000, Magnification = 0.206, Jet Only Flow

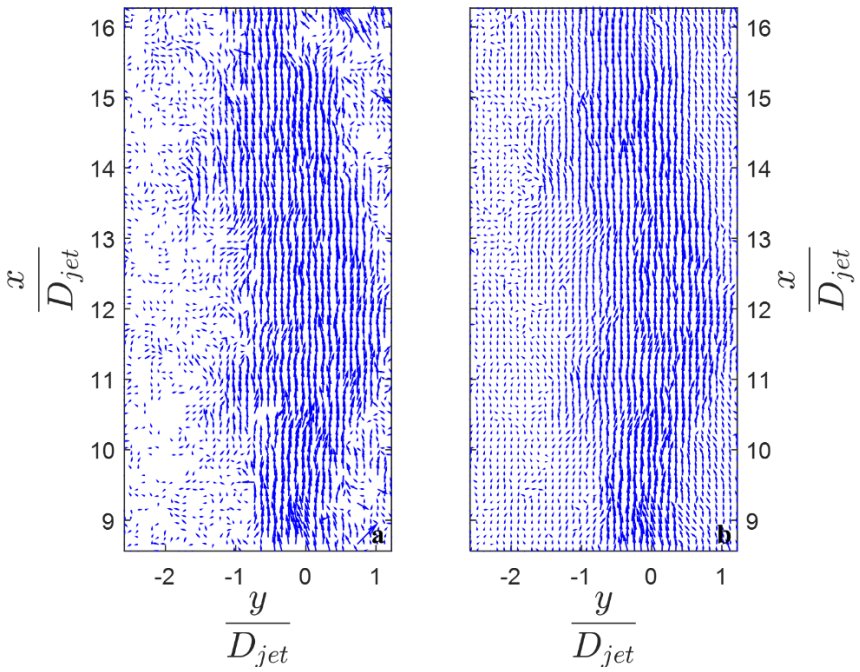

Figure 60. Vector fields for the Re = 10,000, τ_{21} = 7.5 jet only test case. (a) standard (b) multi-frame.

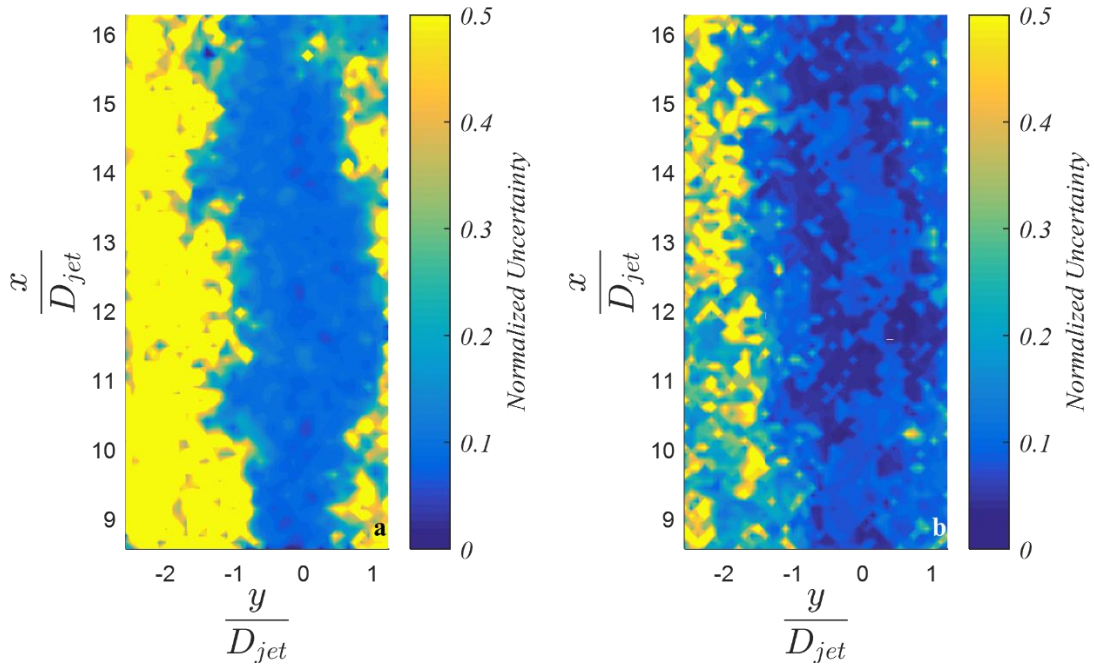

Figure 61. Instantaneous uncertainty maps for the Re = 10,000, τ_{21} = 7.5 jet only test case. (a) standard (b) multi-frame.

A.7 Re = 30,000, Magnification = 0.206, Jet Only Flow

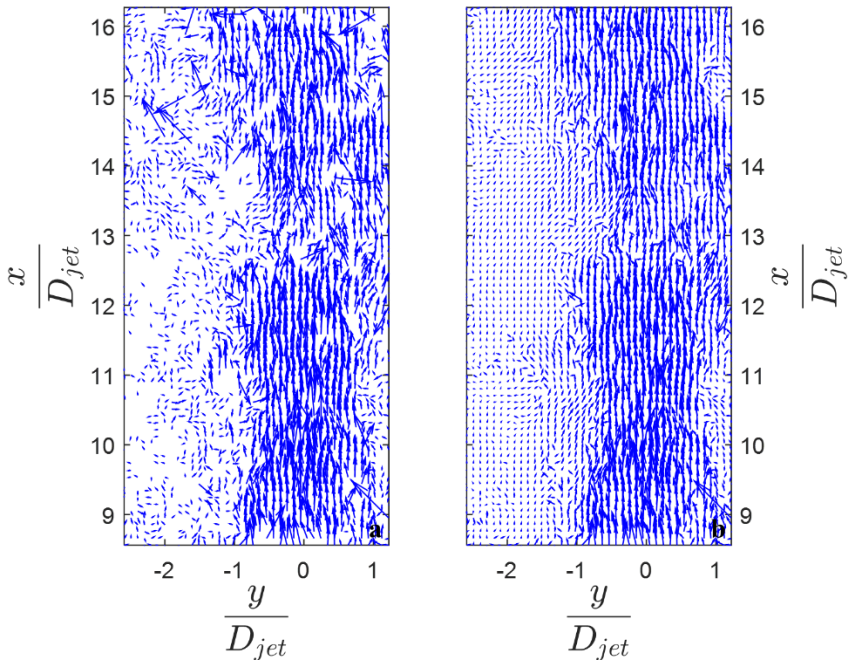

Figure 62. Vector fields for the Re = 30,000, τ_{21} = 2.5 jet only test case. (a) standard (b) multi-frame.

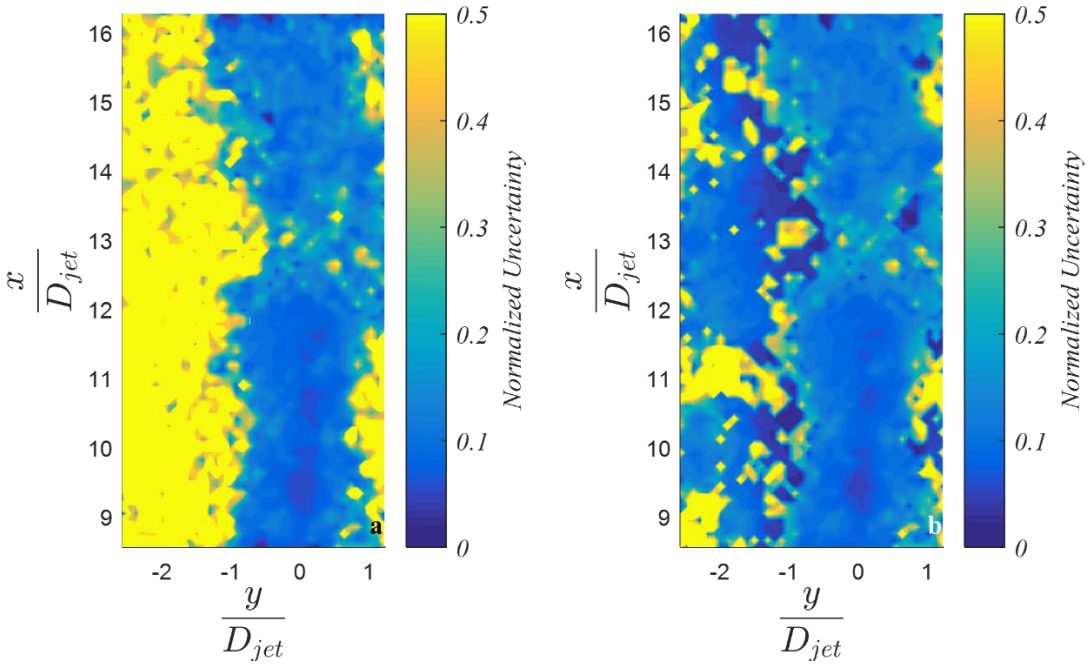

Figure 63. Instantaneous uncertainty maps for the Re = 30,000, τ_{21} = 2.5 jet only test case. (a) standard (b) multi-frame.

A.8 Re = 50,000, Magnification = 0.206, Jet Only Flow

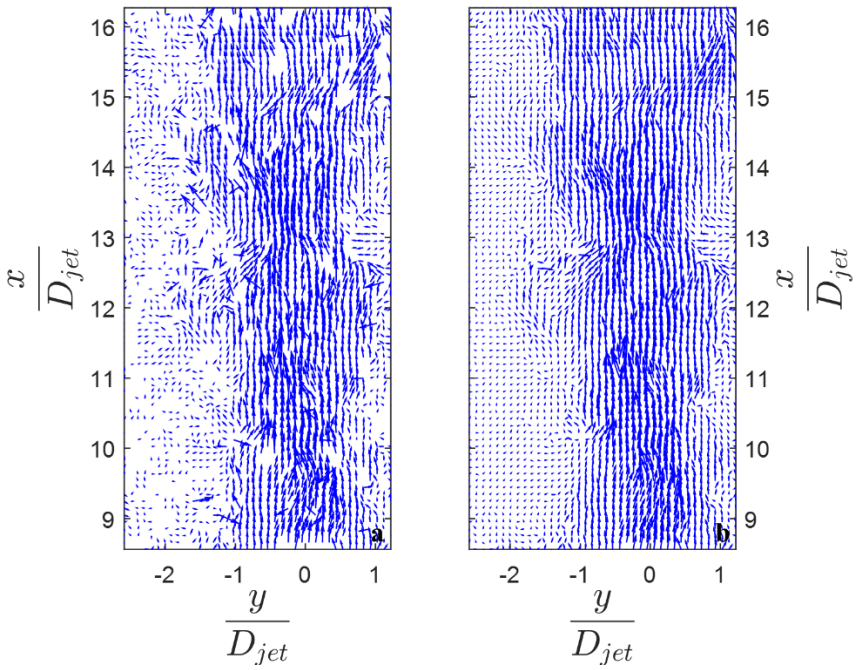

Figure 64. Vector fields for the Re = 50,000, τ_{21} = 2.5 jet only test case. (a) standard (b) multi-frame.

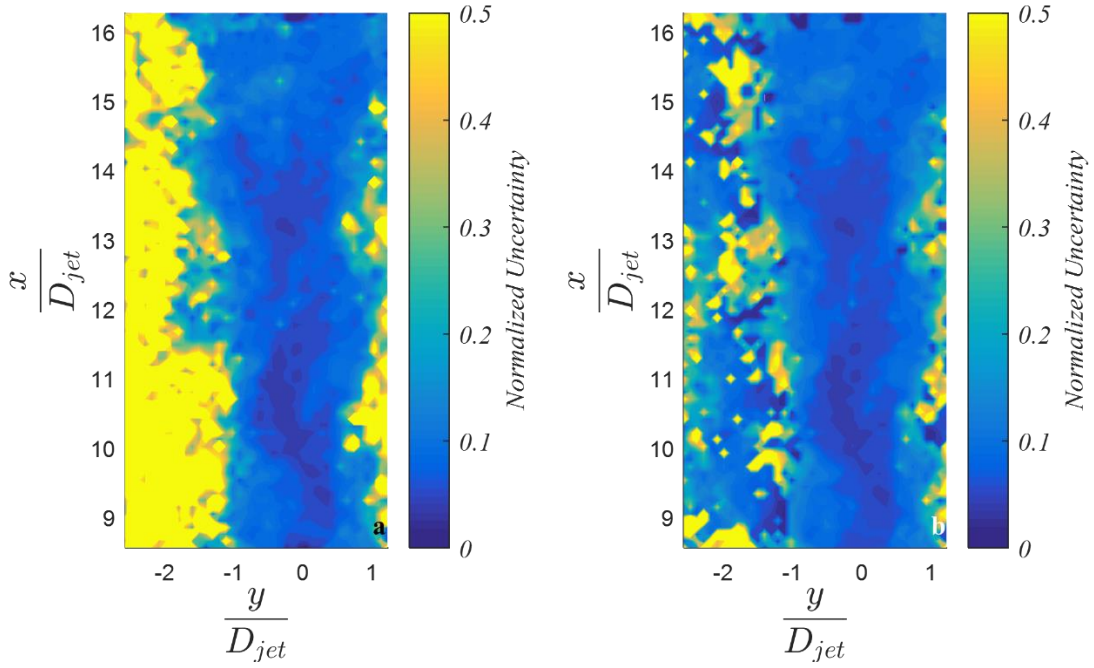

Figure 65. Instantaneous uncertainty maps for the Re = 50,000, τ_{21} = 2.5 jet only test case. (a) standard (b) multi-frame.

APPENDIX B CODE

B.1 Multi-Frame Processing Algorithm

```
% Multi-Frame Processing Algorithm
% Mark Jeffrey Johnson
% 7/20/2016
clear all;
close all;
clc;

%% Set dt's, Shot, and Scale of Velocity Vectors in Composite Plots

scale           = 0.005;        % Scaling factor for plots
sequence        = 1;            % Image sequence
shot            = 2;            % Particular laser burst
Re              = 10000;
dt1             = 7500;
dt3             = 25000;
dt2             = dt3 - dt1;
passes          = 2;
interrogation   = 32;
step            = interrogation / 2;

%% Define Frame Counters, Selects only frames containing particle images

count1 = 1;
frame1 = 1;
frame2 = 2;
frame3 = 3;
end_frame = 223;
frame_counter_short  = zeros((end_frame + 2) * 4 / (5 * 2),1);
frame_counter_medium = zeros((end_frame + 2) * 4 / (5 * 2),1);
frame_counter_long   = zeros((end_frame + 2) * 4 / (5 * 2),1);

for i = 1:((end_frame + 2) / 5)

    frame_counter_short(count1)      = frame1 + (5 * (i - 1));
    frame_counter_short(count1 + 1)  = frame2 + (5 * (i - 1));
    frame_counter_medium(count1)     = frame2 + (5 * (i - 1));
    frame_counter_medium(count1 + 1) = frame3 + (5 * (i - 1));
    frame_counter_long(count1)       = frame1 + (5 * (i - 1));
    frame_counter_long(count1 + 1)   = frame3 + (5 * (i - 1));
    count1 = count1 + 2;

end

clear frame1 frame2 frame3;

%% Set Read Directory, Filename and Mask (if applicable)

read_filename =
['F:\GraduateSchool\PIV\TriplePulsePIV_LongRuns\TriplePulse_CamPos1_BluffBody\Re',num2str(Re),'_d
t',num2str(dt1),'ns_seq',num2str(sequence),'\Re',num2str(Re),'_dt',num2str(dt1),'ns',num2str(shot
,'%03d'),'seq',num2str(sequence),'.tif'];
im = imread(read_filename,1);
width  = length(im(:,1));
height = length(im(1,:));
mask_temp = load('Mask_CamPos1.mat');
mask = cell(1,2);
mask{1,1} = mask_temp.xmask(:,1);
mask{1,2} = mask_temp.ymask(:,1);
load('CP1_BB_PlotParameters.mat');  % .mat file containing non-dimensionalized axis and mask
information
```

```
%% Load calibration image and get conversion factor

figure;
imagesc(imread('F:\GraduateSchool\PIV\TriplePulsePIV_LongRuns\TriplePulse_CamPos1_JetOnly\Ruler.t
if'));
axis equal;
[calx,caly] = getline;
abs(calx(1) - calx(2));
cf = abs(calx(1) - calx(2)); clear calx caly; close all;

%% Process Loops

tic
count = 1;

for im = 1:2:length(frame_counter_short)

    %% Define Image 1,2,3, Crop, Preprocess, Process, Postprocess 1

    image1 = fliplr(rot90(imread(read_filename,frame_counter_short(im)),3));
    image2 = fliplr(rot90(imread(read_filename,frame_counter_short(im + 1)),3));
    image3 = fliplr(rot90(imread(read_filename,frame_counter_long(im + 1)),3));

    image1 = PREPROCESSING(image1,[1 1 width - 1 height - 1],1,20,1,15,0,0,3);
    image2 = PREPROCESSING(image2,[1 1 width - 1 height - 1],1,20,1,15,0,0,3);
    image3 = PREPROCESSING(image3,[1 1 width - 1 height - 1],1,20,1,15,0,0,3);

    %% Process images using PIVlab's FFT cross-correlation function

    [~, ~, dxshort, dyshort, ~] = PIVLAB_FFT(image1,image2,interrogation,step,1,mask,[1 1 width -
1 height - 1],passes,interrogation / 2,interrogation / 4,interrogation / 8,'linear');
    corr_short = corr_results; clear corr_results;
    u_unc_short = dxshort; v_unc_short = dyshort;
    [~, ~, dxmed, dymed, ~]     = PIVLAB_FFT(image2,image3,interrogation,step,1,mask,[1 1 width -
1 height - 1],passes,interrogation / 2,interrogation / 4,interrogation / 8,'linear');
    corr_med = corr_results; clear corr_results;
    [x, y, dxlong, dylong, ~]   = PIVLAB_FFT(image1,image3,interrogation,step,1,mask,[1 1 width -
1 height - 1],passes,interrogation / 2,interrogation / 4,interrogation / 8,'linear');
    corr_long = corr_results; clear corr_results;

    %% First post-processing step (POST1)

    [dxshort,dyshort] = POST1(dxshort,dyshort,3,interrogation / 3,0.1);
    [dxmed,dymed]     = POST1(dxmed,  dymed,  1,interrogation / 3,0);
    [dxlong,dylong]   = POST1(dxlong, dylong, 1,interrogation / 3,0);

    dxshort(isnan(dyshort) == 1) = NaN;
    dyshort(isnan(dxshort) == 1) = NaN;
    dxmed  (isnan(dymed)   == 1) = NaN;
    dymed  (isnan(dxmed)   == 1) = NaN;
    dxlong (isnan(dylong)  == 1) = NaN;
    dylong (isnan(dxlong)  == 1) = NaN;

    %% Convert from px/frame to m/s

    ushort = dxshort * ((0.01 / cf) / (dt1 * 1e-9));
    umed   = dxmed   * ((0.01 / cf) / (dt2 * 1e-9));
    ulong  = dxlong  * ((0.01 / cf) / (dt3 * 1e-9));
    vshort = dyshort * ((0.01 / cf) / (dt1 * 1e-9));
    vmed   = dymed   * ((0.01 / cf) / (dt2 * 1e-9));
    vlong  = dylong  * ((0.01 / cf) / (dt3 * 1e-9));

    %% Compiler function

    [u,v,uc,vc,r,rc] =
COMP(ulong,vlong,umed,vmed,ushort,vshort,corr_long,corr_med,corr_short,interrogation / 2^(passes
- 1));
```

```
    %% Second post-processing step (Post2)

    [u,v,uc,vc] = POST2(u,v,uc,vc,ushort,vshort,umed,vmed,ulong,vlong,rc);

    %% Third post-processing step (POST3)

    umin = -500;
    umax =  500;
    vmin = -500;
    vmax =  500;
    [u,v,uc,vc] = POST3(u,v,uc,vc,umin,umax,vmin,vmax);

    %% Interpolate (if desired, otherwise comment out)

    [u,v,uc,vc] = VECTORFILL(u,v,uc,vc);

    count = count + 1;
    toc

end
```

B.2 Post-processing step 1 (POST1)

```
function [u,v] = POST1(u,v,stdev,maxvel,minvel)

%% Velocity Limits

u(u >  maxvel) = NaN;
v(v >  maxvel) = NaN;
u(u < -maxvel) = NaN;
v(v < -maxvel) = NaN;
u(abs(u) < minvel & abs(v) < minvel) = NaN;
v(abs(u) < minvel & abs(v) < minvel) = NaN;

%% Standard Deviation Filter

meanu = nanmean(nanmean(u));
meanv = nanmean(nanmean(v));
stdu  = nanstd(reshape(u,size(u,1) * size(u,2),1));
stdv  = nanstd(reshape(v,size(v,1) * size(v,2),1));
minvalu = meanu - stdev * stdu;
maxvalu = meanu + stdev * stdu;
minvalv = meanv - stdev * stdv;
maxvalv = meanv + stdev * stdv;
u(u < minvalu) = NaN;
u(u > maxvalu) = NaN;
v(v < minvalv) = NaN;
v(v > maxvalv) = NaN;

end
```

B.3 Compilation (COMP)

```
function [u,v,uc,vc,r,rc] =
COMP(ulong,vlong,umed,vmed,ushort,vshort,corr_long,corr_med,corr_short,int)

%% Determine center of correlation plane

center = (int / 2) + 3;
u = NaN(size(ulong,1),size(ulong,2));
v = NaN(size(ulong,1),size(ulong,2));
uc = NaN(size(ulong,1),size(ulong,2));
vc = NaN(size(ulong,1),size(ulong,2));
r = NaN(size(ulong,1),size(ulong,2),3);
rc = NaN(size(ulong,1),size(ulong,2));

%% For loops to step through the vector field
%  If the vector has been permanently rejected, then the correlation plane
%  data is also set to NaN

for i = 1:size(ulong,2)

    for j = 1:size(ulong,1)

        if isnan(ulong(j,i)) == 1

            corr_long{j,i} = NaN(int,int);

        end

        if isnan(umed(j,i)) == 1

            corr_med{j,i} = NaN(int,int);

        end

        if isnan(ushort(j,i)) == 1

            corr_short{j,i} = NaN(int,int);

        end

    end

end

%% For loops to step through the vector field

for i = 1:size(ulong,2)

    for j = 1:size(ulong,1)

        %% Find primary and secondary peaks for each correlation plane
        %  Then find the ratio

        cl = corr_long{j,i} - mean(mean(corr_long{j,i}));
        cm = corr_med{j,i} - mean(mean(corr_med{j,i}));
        cs = corr_short{j,i} - mean(mean(corr_short{j,i}));
        cl = padarray(cl,[2,2],NaN);
        cm = padarray(cm,[2,2],NaN);
        cs = padarray(cs,[2,2],NaN);
        pks1 = [max(max(cl)) max(max(cm)) max(max(cs))];
        [yl,xl] = find(cl == pks1(1));
        [ym,xm] = find(cm == pks1(2));
        [ys,xs] = find(cs == pks1(3));
```

```
        cl(yl - 2:yl + 2,xl - 2:xl + 2) = 0;
        cm(ym - 2:ym + 2,xm - 2:xm + 2) = 0;
        cs(ys - 2:ys + 2,xs - 2:xs + 2) = 0;
        pks2 = [max(max(cl)) max(max(cm)) max(max(cs))];
        ratio = pks1 ./ pks2;
        r(j,i,1) = ratio(1);
        r(j,i,2) = ratio(2);
        r(j,i,3) = ratio(3);

        %% Temporarilly reject a vector with a vector displacement too small for the short time
spacing only

        if isempty(xs) == 0 && isempty(ys) == 0

            if xs(1) == center && ys(1) == center

                ratio(3) = 0;

            end

        end

        %% Select vector with best ratio

        if find(ratio == max(ratio)) == 1

            u(j,i)  = ulong(j,i);
            v(j,i)  = vlong(j,i);
            uc(j,i) = 1;
            vc(j,i) = 1;
            rc(j,i) = r(j,i,1);

        elseif find(ratio == max(ratio)) == 2

            u(j,i)  = umed(j,i);
            v(j,i)  = vmed(j,i);
            uc(j,i) = 2;
            vc(j,i) = 2;
            rc(j,i) = r(j,i,2);

        elseif find(ratio == max(ratio)) == 3

            u(j,i)  = ushort(j,i);
            v(j,i)  = vshort(j,i);
            uc(j,i) = 3;
            vc(j,i) = 3;
            rc(j,i) = r(j,i,3);

        end

    end

    %% Introduce maximum ratio limit of 1.6

    ratio(ratio < 1.6) = NaN;

    if isnan(ratio(1)) == 0 && isnan(ratio(2)) == 0 && isnan(ratio(3)) == 0

        u(j,i)  = ulong(j,i);
        v(j,i)  = vlong(j,i);
        uc(j,i) = 1;
        vc(j,i) = 1;
        rc(j,i) = r(j,i,1);

    elseif isnan(ratio(1)) == 0 && isnan(ratio(2)) == 0 && isnan(ratio(3)) == 1
```

```
        u(j,i)  = ulong(j,i);
        v(j,i)  = vlong(j,i);
        uc(j,i) = 1;
        vc(j,i) = 1;
        rc(j,i) = r(j,i,1);

    end

end

end
```

B.4 Post-processing step 2 (POST2)

```
% 1 = Long
% 2 = Medium
% 3 = Short

function [u,v,uc,vc] = POST2(u,v,uc,vc,ushort,vshort,umed,vmed,ulong,vlong,rc)

%% Pad all vector arrays

u      = padarray(u,     [2,2],NaN);
v      = padarray(v,     [2,2],NaN);
uc     = padarray(uc,    [2,2],NaN);
vc     = padarray(vc,    [2,2],NaN);
ulong  = padarray(ulong, [2,2],NaN);
umed   = padarray(umed,  [2,2],NaN);
ushort = padarray(ushort,[2,2],NaN);
vlong  = padarray(vlong, [2,2],NaN);
vmed   = padarray(vmed,  [2,2],NaN);
vshort = padarray(vshort,[2,2],NaN);
dif    = zeros(2,1);

%% Find the magnitude of each vector

uvmag    = (u.^2      +      v.^2).^0.5;
longmag  = (ulong.^2  +  vlong.^2).^0.5;
medmag   = (umed.^2   +   vmed.^2).^0.5;
shortmag = (ushort.^2 + vshort.^2).^0.5;

%% Reject vectors with ratio less than 1.2

[ind] = find(rc < 1.2); u(ind) = NaN; v(ind) = NaN;

%% For loops to step through the vector field

for i = 3:size(u,2) - 2

    for j = 3:size(u,1) - 2

        %% Find the median of the kernel

        uvkernel = uvmag(j - 2:j + 2,i - 2:i + 2);
        uvkernel(3,3) = NaN;
        uvmedian = nanmedian(nanmedian(uvkernel));

        %% Find each time spacings difference from the median

        dif(1,1) = abs(uvmedian - longmag(j,i));
        dif(2,1) = abs(uvmedian - medmag(j,i));
        dif(3,1) = abs(uvmedian - shortmag(j,i));

        uind = find(dif == nanmin(dif));

        %% Select best option

        if isempty(uind) == 1

            u(j,i) = NaN;
            v(j,i) = NaN;
            uc(j,i) = 4;
            vc(j,i) = 4;

        elseif uind == 1

            u(j,i) = ulong(j,i);
```

```
            v(j,i) = vlong(j,i);
            uc(j,i) = 1;
            vc(j,i) = 1;

        elseif uind == 2

            u(j,i) = umed(j,i);
            v(j,i) = vmed(j,i);
            uc(j,i) = 2;
            vc(j,i) = 2;

        elseif uind == 3

            u(j,i) = ushort(j,i);
            v(j,i) = vshort(j,i);
            uc(j,i) = 3;
            vc(j,i) = 3;

        end

        if isnan(uc(j,i)) == 1 || isnan(vc(j,i)) == 1

            uc(j,i) = 4;
            vc(j,i) = 4;

        end

    end

end

%% Un-pad arrays

u = u(3:1:size(u,1) - 2,3:1:size(u,2) - 2);
v = v(3:1:size(v,1) - 2,3:1:size(v,2) - 2);
uc = uc(3:1:size(uc,1) - 2,3:1:size(uc,2) - 2);
vc = vc(3:1:size(vc,1) - 2,3:1:size(vc,2) - 2);

end
```

B.5 Post-processing step 3 (POST3)

```
function [u,v,uc,vc] = POST3(u,v,uc,vc,umin,umax,vmin,vmax)

%% Velocity Limits Select

u(u > umax) = NaN;
u(u < umin) = NaN;
v(v > vmax) = NaN;
v(v < vmin) = NaN;
u(find(isnan(v) == 1)) = NaN;
v(find(isnan(u) == 1)) = NaN;
[ind] = find(isnan(u) == 1);
uc(ind) = 4;
vc(ind) = 4;

%% Median Filter

epsilon = 0.1;
thresh  = 4;
[J,I] = size(u);
medianres = zeros(J,I);
normfluct = zeros(J,I,2);
b = 1;

for c = 1:2

    if c == 1; velcomp = u; else; velcomp = v;end %#ok<*NOSEM>

    for i = 1 + b:I - b

        for j = 1 + b:J - b

            neigh = velcomp(j - b:j + b,i - b:i + b);
            neighcol = neigh(:);
            neighcol2 = [neighcol(1:(2 * b + 1) * b + b); neighcol((2 * b + 1) * b + b + 2:end)];
            med = nanmedian(neighcol2);
            fluct = velcomp(j,i) - med;
            res = neighcol2 - med;
            medianres = nanmedian(abs(res));
            normfluct(j,i,c) = abs(fluct / (medianres + epsilon));

        end

    end

end

info1 = (sqrt(normfluct(:,:,1).^2 + normfluct(:,:,2).^2) > thresh);
u(info1 == 1) = NaN;
v(info1 == 1) = NaN;
uc(info1 == 1) = 4;
vc(info1 == 1) = 4;

end
```